Structure Determination of Nanocrystalline Materials

A Dissertation Presented

by

Frederick Marc Michel

to

The Graduate School

in Partial Fulfillment of the

Requirements

for the Degree of

Doctor of Philosophy

in

Geosciences

Stony Brook University

December 2007

Stony Brook University

The Graduate School

Frederick Marc Michel

We, the dissertation committee for the above candidate for the
Doctor of Philosophy degree, hereby recommend
acceptance of this dissertation.

Martin A. A. Schoonen, Dissertation Advisor
Professor, Department of Geosciences

Brian L. Phillips, Chairperson of Defense
Professor, Department of Geosciences

John B. Parise, Dissertation Co-Advisor
Professor, Department of Geosciences & Department of Chemistry

Troy Rasbury
Professor, Department of Geosciences

Daniel R. Strongin
Professor, Department of Chemistry
Temple University

This dissertation is accepted by the Graduate School

Lawrence Martin
Dean of the Graduate School

Abstract of the Dissertation

Structure Determination of Nanocrystalline Materials

by

Frederick Marc Michel

Doctor of Philosophy

in

Geosciences

Stony Brook University

2007

There are numerous examples of nanocrystalline compounds that exhibit unique properties such as enhanced reactivity or unusual catalytic, magnetic, or optical behavior relative to their bulk counterparts. These interesting properties of nanosized materials, typically less than ~20 nm, are inextricably related to their size, shape, composition, and atomic structure. Developing a comprehensive understanding of these fundamental attributes of nanoparticles is a critical step towards understanding their size/shape/composition/structure-property relationships. These properties strongly influence their roles in geochemical and biological systems, and are crucial for unlocking their functional potential.

The principal goal of this dissertation was to quantitatively determine and evaluate the structures, i.e., the three-dimensional atomic arrangements, of a number of important nanocrystalline compounds. Included in this dissertation are detailed studies of the ferric oxyhydroxide mineral known as ferrihydrite ($Fe(OH)_3$), the initial iron sulfide precipitate (FeS), and several manganese sulfide (MnS) polymorphs. While the majority of the samples were synthetically-derived, a sample formed naturally through biomineralization was also investigated. A quantitative evaluation of their structures was accomplished primarily though the application of high-energy X-ray total scattering coupled with pair distribution function analysis. The application of this method to these particular compounds has resulted in substantial advancements over prior attempts that relied on conventional methods for structure determination, specifically X-ray diffraction and X-ray absorption spectroscopy. The major findings of this dissertation resolve several long-standing questions, particularly regarding the structures of these compounds.

Experimental studies of nanoparticles are inherently challenging due to extremely small particle sizes, instability, and highly reactive surfaces. These qualities necessitated the development of specific procedures for the synthesis, processing, and handling of these compounds, some of which are air-sensitive. The protocols utilized are described in detail and represent an important contribution to future studies involving these and similar nanosized compounds. In the conclusion of this dissertation, the implications of the major findings are summarized, important unanswered questions are posed, and an outlook for future experiments is presented.

This work is dedicated to the people who have shown me true friendship and love…
Neus.
My Family.
My Friends.

A portion of this dissertation is dedicated in memoriam to Charlie McClennen, my former academic advisor and Professor of Geology, Colgate University.

Table of Contents

The Short- to Medium-Range Atomic Order and Crystallite Size of the Initial FeS Precipitate from Pair Distribution Function Analysis

Hydrothermal Synthesis of Pure α-Phase Manganese(II) Sulfide
without the Use of Organic Reagents

Similarities in 2- and 6-Line Ferrihydrite Based on
Pair Distribution Function Analysis of X-ray Total Scattering

The Structure of Ferrihydrite, a Nanocrystalline Material

Structure of the Iron Core in Horse-Spleen Ferritin

List of Illustrations

Chapter 2

Figure 1 15

Calculated PDF, or *G(r)*, plotted against distance *r* (Å) for γ-MnS. The calculation is based on spacegroup $P6_3mc$ and the structural details reported in ICSD# 44765. The first correlation in the PDF at ~2.4 Å corresponds to the average Mn-S distance in the MnS_4 tetrahedron. This and the corner-sharing connectivity of the tetrahedra are defined by the short-range order. The intermediate range ordering to ~15 Å reflects the overall topology of the structure. The long-range ordering describes the extended periodicity of the topology and extends from ~20 Å *ad infinitum*.

Figure 2 22

Geometry typical of a high-energy X-ray total scattering experiment at the Advanced Photon Source at Argonne National Laboratory. The incident beam of high-energy X-rays interacts with a sample loaded in a capillary and mounted in the goniometer. The scattered X-rays are collected in Debye-Scherrer geometry using a 2-D plate-style detector (shown above) or by using a scanning point counter. A beamstop is used to prevent damage to the detector from the portion of the incident beam continuing beyond the sample (long dashes).

Figure 3 25

The experimental PDF *G(r)* versus distance *r* is plotted for a synthetic sample of 6 nm ferrihydrite (Fhyd6). Calculated PDFs for akaganéite and goethite are also plotted to show the similarities in the atom-atom distances over the first ~5 Å, typical of the range of distances reported by EXAFS.

Chapter 3

Figure 1 44

The layered structure of mackinawite. Small spheres represent Fe atoms; large spheres represent S atoms; a unit cell is outlined. Fe is tetrahedrally coordinated by S atoms and in square planar coordination with Fe.

Figure 2a - f..45

The normalized scattering function $Q[S(Q)-1]$ vs. Q ($Å^{-1}$) for each of the six FeS samples.

Chapter 4

Chapter 5

Chapter 6

Chapter 7

List of Tables

Chapter 3

Chapter 4

Chapter 5

Chapter 6

Chapter 7

Acknowledgements

Firstly, I would like to acknowledge the mentorship and support of my advisors, Martin Schoonen and John Parise. Both have given me a substantial amount of guidance and direction during the course of my Ph.D., while also allowing me the freedom to pursue my own research interests. I am forever grateful for the opportunities they provided and for their friendship towards me during my time at Stony Brook.

The content of this dissertation was also substantially improved by the guidance and thoughtfulness of a number of people at Stony Brook, most notably Lars Ehm, Brian Phillips, Sytle Antao, Aaron Celestian, and Jim Quinn. I have learned a great deal from working with all of them over the past four years. I would especially like to thank Dan Strongin and his group at Temple University and also acknowledge Xiang Zhang and Scot Martin at Harvard University, who were among my first collaborators. Many thanks to Pete Chupas, Peter Lee, and Sarvjit Shastri at the APS, without whom much of the work included in this dissertation would not have been possible. I'd also like to thank Troy Rasbury, Brian, Martin, John, and Dan for serving on my Ph.D. defense committee.

I'd like to say thank you to all of my friends who are members (current and former) of the Geosciences Department. Alex, Shannon, Richard, Brian, Nick, Joel and all the rest - despite moving on, I look forward to many more years as friends. Special thanks to Andrea Illausky, Emily Vance, Owen Evans, and Loretta Budd for their patience, support, and assistance. There are many people in an academic department who make a research experience like mine possible – many thanks to all faculty and staff.

My research would also not have been possible without the financial support provided by The Research Foundation of New York and the Department of Geosciences. I am also grateful for the funding provided by the Center for Environmental Molecular Science (CEMS) which fostered the majority of my research. Funded through the National Science Foundation, CEMS was made possible thanks to the efforts of Rich Reeder and all of the other principal investigators involved. Part of my research was also made possible by funding from the GAANN Fellowship Program and the National Aeronautics and Space Administration through the Office of Space Science. Additionally, I would like

to acknowledge the use of the Advanced Photon Source at Argonne National Laboratory and National Synchrotron Light Source at Brookhaven National Laboratory; both are supported by the U.S. Department of Energy.

Finally, I would like to acknowledge all of my family and friends who are dearest to me. First and foremost, I want to thank Neus for her inspiration and unwavering love, patience, and support. Thank you to my parents, siblings, extended family and Jo DeMari for all of your love and support. I would be lost without all of you in my life and words can not describe how much all of you mean to me.

Chapter 1: Introduction

The occurrence of nanosized particles in geochemical and biological systems, and use in technological and industrial applications, is attracting broad scientific attention. This is mainly because nanosized compounds often exhibit enhanced reactivity as well as unusual catalytic, magnetic, or optical behavior relative to their well-crystallized bulk counterparts. The interesting properties of nanoparticles, typically less than a few tens of nanometers in diameter, are inextricably related to their size, shape, composition and structure. While detailed studies of certain nanosized compounds have demonstrated size- and shape-property relationships (e.g., (*1, 2*) see (*3*) for review), quantitative examinations of structure, i.e., their 3-dimensional atomic arrangements, are often not possible by conventional methods. Comprehensive evaluations of these fundamental attributes are crucial for uncovering their roles in geochemical environments, biological systems, and tailoring for functional applications.

Genesis of nanoparticles in the environment occurs via a variety of both inorganic and biogenic pathways (see (*4*) for review). In geochemical systems, high degrees of supersaturation tend to produce large concentrations of nanoparticles. Examples include mixing zones in proximity to hydrothermal vents (*5*) and in chemical weathering-dominated systems such as acid mine drainage environments. In terms of biological pathways, the interaction of microorganisms with nanosized precipitates is significant. In general, these are processes centering on the ability of some microorganisms to generate metabolic energy by chemical redox reactions involving the formation or dissolution of nanoparticles (e.g., (*6*)). In other cases, organisms take advantage of specific properties of nanosized compounds to fulfill certain biological functions such as navigation ability (*7*) or the regulation of iron through protein-coated biominerals (*8*). Overviews of several types of formation environments relevant to the formation of nanosized compounds are included below. The focus is on the particular compounds relevant to this dissertation and their respective roles in specific geochemical and biological processes of interest.

Iron Sulfide Nanoparticles and the Early Diagenesis of Marine Sediments

In Earth's crust, pyrite formation from iron monosulfide is a key process in several geochemical cycles including maintenance of the oxygen content of the atmosphere (*9*), controlling metal and metalloid concentrations in natural waters (*5*), and in diagenetic cycling in marine sediments (*10*). The interaction of iron sulfides with various metals and metalloids is receiving increased attention because of the adverse health affects caused by these elements entering the food chain (*11*). In particular, the presence of defects and incorporation of impurities in pyrite (FeS_2) strongly affect its reactivity and surface chemistry. This enhanced reactivity is of increasing concern in terms of public health due to the potential dangers associated with ingestion of sulfide-containing coal dust and fly ash from mining and combustion activities (*12, 13*). The mechanisms for incorporation of minor (e.g., a few percent) and trace (<1 wt. %) elements in the initial iron monosulfide phase (FeS) and during the transformation of FeS to FeS_2 are not entirely clear (*14*). This is in part due to a poor understanding of the structure of the initial FeS precipitate.

The first step in the formation of iron sulfides under aqueous conditions is the nucleation of a reduced, iron monosulfide (commonly referred to as "disordered" or "amorphous" FeS) that is generally believed to be a precursor to crystalline mackinawite (FeS) (*15*). Hydrogen sulfide species, produced by sulfate-reducing bacteria, react with iron sources within the sediments to form FeS. The source of iron and other metals in sediments is primarily from the microbial reduction and dissolution of metal-bearing oxides and hydroxides originating from terrigenous materials and from mid-ocean ridge hydrothermal vent systems. Under sulfidic conditions, the subsequent conversion of FeS to FeS_2 can occur via a number of possible reaction pathways (see (*16*) for review).

The initial FeS precipitate is characterized by extremely small crystallite sizes which results in a large amount of reactive surface area. Evidence of the incorporation of minor and trace elements into Fe-S phases has been observed and reported in many studies involving samples collected from both natural (pristine) and contaminated environments (*17*). A mechanistic understanding of the pyritization of minor and trace elements has begun to emerge through research addressing the thermodynamic and kinetic behavior of metals and metalloids and, based on observational data, suggests that various elements exhibit very different behavior in sulfidic sediments (*14*). In Chapter 3, the structure of synthetic nanosized FeS is evaluated. Establishing the structure of the initial FeS precipitate is a critical step in understanding the association and of potential contaminants and their fate during subsequent transformation to more stable phases such as pyrite.

Exploring the Role of Semiconducting Minerals in Prebiotic Synthesis

Photoelectrochemical reactions on mineral surfaces are hypothesized to have played a critical role in prebiotic synthesis (*18*). In particular, photochemistry on the surfaces of colloidal semiconducting mineral particles such as MnS and ZnS can open novel reaction pathways and enhance reaction rates. In principle, the excitation of conduction-band electrons to valence-band holes by photons with sufficient energy creates the potential for driving redox reactions (*19*). The reduction of carbon from sources such as CO_2 under ultraviolet light is favorable for forming potential building blocks for organic molecules. The large surface area and catalytic properties of nanoparticles are expected to enhance this effect and therefore are important in the context of prebiotic synthesis.

The reducing conditions hypothesized for Hadean marine environments on the early Earth (*20*) and widespread occurrence of hydrothermal vents are suspected to have led to significant concentrations of semiconducting sulfide minerals, including nanosized MnS and ZnS particles, dispersed in the surrounding seawater. Laboratory-based studies involving these compounds are currently our best means for investigating the capabilities of sulfides in the fixation of carbon. Common synthesis methods involve the precipitation of sulfides under supersaturated conditions and lead to the formation of an initially nanosized particles. Sufficient aging of these initial precipitates under anoxic, low-temperature conditions leads to well-crystallized particles. In Chapter 4, the structures of the different polymorphs of MnS are investigated for both nanosized and bulk precipitates.

Nanoparticle Formation in Acid Mine Drainage Environments

Acid mine drainage (AMD) refers to the generation and outflow of highly acidic waters resulting from the weathering of exposed crushed rock debris (mine tailings) generally rich in metal sulfides. In contaminated aqueous geochemical systems associated with AMD, dissolved species such as chromium, mercury, lead, iron, aluminum and arsenic are mobilized in high concentrations (e.g., (*21, 22*)). The hazards associated with the uptake or ingestion of certain metals and metalloids by humans and many other types of biota make evaluating the geochemical processes associated with AMD important.

Depending on the redox conditions in the waters and underlying sediments of AMD-impacted streams and lakes, the mobilized species often precipitate as nano-sized sulfides and oxyhydroxides. In particular, an abundance of iron and aluminum is commonly observed and under hydrolyzing conditions leads to the formation of nanoparticles (*23, 24*). With dimensions typically between 1 – 10 nm, these particles exhibit a vast amount of reactive surface area and thus are important to the sequestration of potential contaminants through adsorption and co-precipitation (e.g., (*25*)). Furthermore, the association of nanoparticles with metals and metalloids under aqueous conditions (*26, 27*), and their subsequent transformation to more stable phases, makes these compounds of interest in the context of the fate and transport of contaminants.

Often the most frequently observed ferric iron precipitate in AMD environments is the mineral ferrihydrite, also commonly referred to as amorphous or hydrous ferric (hydr)oxide (*22, 28, 29*). While the precipitation of ferrihydrite in these environments is predominantly a consequence of inorganic processes (i.e., iron oxidation and hydrolyzation reactions), it is also facilitated by bacteria in AMD sediments (*6*). Unstable and highly reactive in general, ferrihydrite is exclusively nanosized and shows significant association with important environmental contaminants such as arsenic (*30*) and chromium (*31*). As such, it is also manufactured for use as a scavenger of heavy metals and metalloids during the treatment of wastewaters and in remedial activities (e.g., (*32*)).

Even with the considerable attention given to the chemical and physical properties of ferrihydrite in previous research, there remains a long-standing lack of consensus regarding its crystal structure (see (*24*) for review). This has undoubtedly limited progress in developing a full understanding of its composition as well as its role in geochemical environments. Determining a starting structural model for this phase is particularly challenging because ferrihydrite is exclusively nanocrystalline and has no known well-crystallized counterpart that can be synthesized in the laboratory or found in nature. As discussed in Chapter 5 of this dissertation, the primary difference between the different forms of inorganically-derived ferrihydrite is the size of individual crystallites, which are typically less than 10 nm in diameter. Chapter 6 presents a new structure model for ferrihydrite. As discussed in chapters 5 and 6, conventional methods of structure determination proved inadequate for the study of ferrihydrite nanoparticles and was the primary impediment to an earlier definitive structural determination for this phase.

Biomineralization of Nanoparticles

There are numerous examples of organisms evolving with the remarkable ability to form minerals in order to fulfill specific biological functions. These mineral phases can occur as discrete nanosized particles and serve a variety of functions including the formation of mineralized skeletal features (*33, 34*), gravity and navigation sensors in Earth's magnetic field (*35, 36*), and regulation of iron via protein-coated iron minerals (*8, 37*). The processes by which organisms form minerals are broadly referred to as biomineralization and can be divided into two groups (see (*38*) for review). In brief, *biologically induced* mineralization refers to secondary precipitation of minerals that occurs due to interactions between biological activity and the environment. For example, certain bacteria generate metabolic energy by chemical redox reactions involving the extracellular formation of nanoparticles (*39*). In such cases, there tends to be a minimal level of control put forth by the organism in terms of the shape, size, or composition of the nanoparticle. At the other end of the biomineralization spectrum are *biologically controlled* processes, whereby organisms use cellular activity to expressly control aspects such as shape, size, and composition, as well as the ultimate location of a biomineral (i.e., extra-, inter-, or intracellular). For example, magnetotactic bacteria synthesize intracellular, single-domain nanoparticles of magnetite and utilize these particles for navigation in Earth's magnetic field (*40*). Biomineralization of calcium-containing phases also occurs in a wide variety of organisms and serves a variety of functions including forming protective exoskeletons or adding structural stability through internal skeletal features (e.g., (*41, 42*)). The often complex processes associated with biomineralization and difficulties in studying the potentially transient and unstable nanosized products make this a challenging area of research.

An interesting example of biomineralization is found as a result of the need for organisms to regulate iron, an essential element to most cellular activity and prosperity, and is common to virtually all living organisms, including humans (*8, 37*). While organisms exploit the redox properties of iron for metabolic activity, it becomes potentially toxic in sufficiently high concentrations. Additionally, Fe^{3+} is virtually insoluble at neutral pH. The evolutionary solution to the problem of storing and releasing iron is the biomineralization of protein-encapsulated iron(III) oxyhydroxide nanoparticles. In Chapter 7, the structure of the nanocrystalline core formed in a natural sample of horse-spleen ferritin is evaluated. While the core has long been suspected to resemble the mineral ferrihydrite, a quantitative structure model is lacking. Furthermore, nanosized protein cages are increasingly being used as platforms for the nanoscale engineering of dispersed materials with biocompatible and bioactive properties (*43-45*). Quantitative methods of evaluating the structure of the nanosized particles formed in horse-spleen ferritin and other similar proteins are essential for the engineering and development of functional compounds.

Summary of Structure Determination of Nanocrystalline Materials

A survey of prior experimental studies on the nanosized compounds of interest in this dissertation indicates a lack of consensus regarding their structures (e.g., (*10, 24, 46, 47*)). In principal, this ambiguity arose because the traditional crystallographic methods used in these studies provided depictions of structure that were most sensitive either to long-range periodicity (X-ray, electron, or neutron diffraction) or short-range order (X-ray absorption spectroscopy). While these methods may be useful for identification of a nanosized phase under certain circumstances, structure determination and the extraction of quantitative structural details for an unknown compound are not always possible. This is often because diffraction patterns for nanoparticles are information-poor and results in ambiguity during subsequent interpretation.

In this dissertation, new evaluations of the structures of several important nanosized compounds were conducted using high-energy X-ray total scattering coupled with pair distribution function analysis. As will be discussed, the short-, intermediate-, and long-range ordering of a nanocrystalline compound are simultaneously attainable by this method. The results presented indicate that total scattering and PDF analysis is currently the best method for obtaining atomic arrangements of compounds forming with extremely small particle sizes and substantial disorder. Furthermore, the results indicate that the prior lack of consensus in regards to the structures of these compounds resulted primarily from limitations in the structure determination methods available at the time.

The following chapters of this dissertation are arranged in an order that reflects two important stages of progress. The first is the early development of laboratory procedures for working with nanosized particles. These procedures were subsequently used throughout the rest of the experimental work. Secondly, structural evaluations for compounds of interest become increasing more challenging and complex, as explained below. Chapter 2 includes experimental details relevant to the techniques utilized and an explanation of the terminology used throughout this dissertation. Chapters 3 and 4 include the experimental studies conducted on reduced iron and manganese sulfide compounds. These compounds are highly susceptible to oxidation, particularly when nanosized, and the development of protocols for synthesizing, processing, and handling was necessary to ensure sample integrity. These procedures are described in detail in these chapters. In terms of structure determination and evaluation, nanosized MnS and FeS have well-crystallized counterparts with known structures. These models were readily available for testing against MnS products with unknown structures. Conversely, the structure evaluation for ferrihydrite, included in Chapters 5 and 6, was significantly more challenging. This is because ferrihydrite has no known crystalline counterpart and previously proposed structure models were generally incomplete. The lack of an accepted structure for ferrihydrite necessitated the development of a new structure model for this phase. In Chapter 7, the iron core formed in the ferritin protein, long-suspected to be similar to ferrihydrite, was evaluated. With a new structure model available for this phase, the structure of the nanosized core formed in ferritin through biomineralization was testable. A summary of the major findings and outlook toward future is included in Chapter 8.

References

1. W. Vogel, J. Urban, M. Kundu, S. K. Kulkarni, *Langmuir* **13**, 827 (1997).
2. K. Watanabe, D. Menzel, N. Nilius, H. J. Freund, *Chemical Reviews* **106**, 4301 (2006).
3. E. Roduner, *Chemical Society Reviews* **35**, 583 (2006).
4. J. F. Banfield, H. Z. Zhang, in *Nanoparticles and the Environment*. (2001), vol. 44, pp. 1-58.
5. G. W. Luther, D. T. Rickard, *Journal of Nanoparticle Research* **7**, 389 (2005).
6. W. A. Clarke, K. O. Konhauser, J. C. Thomas, S. H. Bottrell, *Fems Microbiology Reviews* **20**, 351 (1997).
7. D. A. Bazylinski, B. M. Moskowitz, in *Geomicrobiology: Interactions between Microbes and Minerals*. (1997), vol. 35, pp. 181-223.
8. A. Lewin, G. R. Moore, N. E. Le Brun, *Dalton Transactions* **22**, 3597 (2005).
9. R. T. Wilkin, H. L. Barnes, *Geochimica et Cosmochimica Acta* **60**, 4167 (1996).
10. R. A. Berner, *American Journal of Science* **265**, 773 (1967).
11. L. M. Mayer *et al.*, *Environmental Science & Technology* **30**, 2641 (1996).
12. R. B. Finkelman, *International Journal of Coal Geology* **59**, 19 (2004).
13. R. B. Finkelman *et al.*, *International Journal of Coal Geology* **50**, 425 (2002).
14. J. W. Morse, G. W. Luther III, *Geochimica et Cosmochimica Acta* **63**, 3373 (1999).
15. M. A. A. Schoonen, H. L. Barnes, *Geochimica et Cosmochimica Acta* **55**, 1505 (1991).
16. D. Rickard, G. W. Luther, *Chemical Reviews* **107**, 514 (2007).
17. M. A. Huerta-Diaz, J. W. Morse, *Geochimica et Cosmochimica Acta* **56**, 2681 (1992).
18. X. V. Zhang *et al.*, *Journal of Photochemistry and Photobiology a-Chemistry* **185**, 301 (2007).

19. M. R. Hoffmann, S. T. Martin, W. Y. Choi, D. W. Bahnemann, *Chemical Reviews* **95**, 69 (1995).

20. H. D. Holland, *The Chemical Evolution of the Atmosphere and Oceans* (Princeton University Press, Princeton, NJ, 1984), pp. 598.

21. B. M. Chapman, D. R. Jones, R. F. Jung, *Geochimica et Cosmochimica Acta* **47**, 1957 (1983).

22. P. L. Smedley, D. G. Kinniburgh, *Applied Geochemistry* **17**, 517 (2002).

23. G. Furrer, B. L. Phillips, K. U. Ulrich, R. Pothig, W. H. Casey, *Science* **297**, 2245 (2002).

24. J. L. Jambor, J. E. Dutrizac, *Chemical Reviews* **98**, 2549 (1998).

25. G. A. Waychunas, C. S. Kim, J. F. Banfield, *Journal of Nanoparticle Research* **7**, 409 (2005).

26. M. F. Hochella, A. F. White, *Reviews in Mineralogy* **23**, 1 (1990).

27. S. L. S. Stipp *et al.*, *Chemical Geology* **190**, 321 (2002).

28. C. C. Fuller, J. A. Davis, G. A. Waychunas, *Geochimica et Cosmochimica Acta* **57**, 2271 (1993).

29. K. A. Quinn, R. H. Byrne, J. Schijf, *Environmental Science & Technology* **41**, 541 (2007).

30. G. A. Waychunas, B. A. Rea, C. C. Fuller, J. A. Davis, *Geochimica et Cosmochimica Acta* **57**, 2251 (1993).

31. L. Charlet, A. Manceau, *Journal of Colloid and Interface Science* **148**, 443 (1992).

32. B. J. Moldovan, M. J. Hendry, *Environmental Science & Technology* **39**, 4913 (2005).

33. H. A. Lowenstam, S. Weiner, *On Biomineralization* (Oxford University Press, New York, 1989), pp. 336.

34. N. Watabe, V. R. Meenakshi, P. L. Blackwelder, E. M. Kurtz, D. G. Dunkelberger, in *Mechanisms of Biomineralization in the Invertebrates and Plants;* N. Watabe, K. M. Wilbur, Eds. (University of South Carolina Press, Columbia, SC, 1976) pp. 283-308.

35. R. B. Frankel, D. A. Bazylinski, *Hyperfine Interactions* **90**, 135 (1994).

36. K. O. Konhauser, *Fems Microbiology Reviews* **20**, 315 (1997).

37. N. D. Chasteen, P. M. Harrison, *Journal of Structural Biology* **126**, 182 (1999).

38. S. Weiner, P. M. Dove, in *Biomineralization*. (2003), vol. 54, pp. 1-29.

39. D. Fortin, S. Langley, *Earth-Science Reviews* **72**, 1 (2005).

40. R. Blakemore, *Science* **190**, 377 (1975).

41. H. A. Lowenstam, *Science* **211**, 1126 (1981).

42. J. R. Young, K. Henriksen, in *Biomineralization*. (2003), vol. 54, pp. 189-215.

43. T. Douglas *et al.*, *Science* **269**, 54 (1995).

44. F. C. Meldrum, T. Douglas, S. Levi, P. Arosio, S. Mann, *Journal of Inorganic Biochemistry* **58**, 59 (1995).

45. M. Uchida *et al.*, *Journal of the American Chemical Society* **128**, 16626 (2006).

46. R. B. Herbert, S. G. Benner, A. R. Pratt, D. W. Blowes, *Chemical Geology* **144**, 87 (1998).

47. D. Rickard, *Chemical Geology* **78**, 315 (1989).

Chapter 2: Experimental

Strategy Overview

Studies of compounds formed in complex and dynamic natural systems often benefit from also evaluating inorganically-derived materials formed in vitro under controlled laboratory conditions. Such methodology enables researchers to minimize complexity caused by the incorporation of impurities such as metals or metalloids, or by the conditions of formation (e.g., presence of organics). For this reason, the majority of the compounds evaluated in this dissertation were formed synthetically. The overall goal has been to develop a firm understanding of the fundamental attributes of these compounds, namely, their size, morphology, composition, and atomic structure. This information was obtained using a combination of advanced synchrotron- and laboratory-based techniques. It should be noted that results from studies of samples derived in vitro are not necessarily fully applicable to natural systems and this must be taken into consideration when comparing the results presented here to related studies.

This dissertation includes structural evaluations of several nanosized compounds often referred to in the literature as being "X-ray amorphous" (e.g., (*1-3*)). Use of this term is technique-dependent and implies that these materials are exclusively short-range ordered with virtually no periodicity. The ability to differentiate between materials that are truly amorphous (e.g., glass or liquid) and nanocrystalline compounds, which exhibit limited long-range periodicity due to finite particle sizes, is of substantial importance. For example, the incorrect classification of a nanocrystalline material as amorphous and lack of quantitative structural model is potentially detrimental to thermodynamic modeling and limits progress in understanding structure-property relationships and their role in environmental, industrial, and biological systems.

Technique Summary

A variety of experimental techniques were utilized as part of this dissertation to obtain information regarding the size, morphology, composition, and structure of the materials of interest. The primary approach used to investigate the structural arrangements of nanosized materials is high-energy X-ray total scattering coupled with pair distribution function (PDF) analysis. For crystalline phases, conventional X-ray diffraction (XRD) methods were applied. The size distribution of selected samples was evaluated using dynamic light scattering (DLS), scanning electron microscopy (SEM), and transmission electron microscopy (TEM). Direct imaging methods (SEM and TEM) were also used to assess morphological characteristics. Selected samples were evaluated for weight-loss with temperature via thermogravimetric analysis (TGA) and chemical composition by means of colorimetric techniques. Brief overviews of the principals behind each of these techniques and the types of information obtained are described herein. As high-energy X-ray total scattering and PDF analysis is the primary experimental method utilized in this dissertation, this section will be the most comprehensive. Detailed information regarding the synthesis of compounds relevant to this dissertation is included in the subsequent chapters. Where appropriate, also included are acknowledgements of samples synthesized by other collaborators.

In regards to evaluating structure, there are several important and widely used structure determination and analysis methods. XRD of single- and polycrystalline samples is arguably the most frequently used method as part of laboratory-based studies. The diffraction patterns of well-crystallized powders facilitate phase identification and yield quantitative structural information. However, as discussed below there are limits to the amount of information obtainable from powder XRD, particularly for nanosized samples. For single-crystal diffraction experiments, there are limitations in terms of the minimum usable crystallite size due to the need to physically mount individual crystals prior to examination. With few exceptions (*4, 5*), single-crystal diffraction measurements are not routinely performed on crystals with dimensions less than several microns. Electron diffraction using transmission electron microscopy is a viable alternative for submicron particle sizes and therefore is increasingly used for nanosized materials. A wide variety of additional spectroscopic techniques exist for evaluating atoms, molecules, and solids (see (*6-9*) for reviews). These methods were not utilized as part of this dissertation and will therefore not be covered. Since previous models for the compounds of interest were based on diffraction and X-ray absorption spectroscopy, these methods will be the main focus of the discussion on the limitations of structure determination methods.

It is important to note that *senso stricto* there is currently no individual structure determination and analysis method that provides a complete picture of the atomic arrangement in nanosized particles for any compound. In the case of nanosized particles (< ~10 nm), significant effects from factors such as complex disorder, defects and surface relaxation are possible and must be understood. While modern methods for structure determination and analysis offer partial understanding of this complexity, a full description of the position of each individual atom (i.e., full particle simulations) is not yet feasible. The current state-of-the-art is to apply a suite of techniques, which provide partially overlapping information that can be assembled to form a more comprehensive structure model than any single method. As such, an overview of the strengths and weaknesses of contemporary structural probes in the context of structure determination and analysis of nanosized materials is presented.

Terminology for Ranges of Order

A continuum exists between materials possessing short-, intermediate-, and long-range ordering and where the boundaries are drawn between these is therefore artificial. This idea has been addressed in the glass community (e.g., (*10-12*)) but confusion persists in other areas of the geosciences. For clarification, a general description of the guidelines used by the glass community to define ranges of order in glass and liquid structure is included here (see (*13*) for review). This description will be useful for understanding the results and discussion presented in this dissertation.

The continuum of atomic ordering in matter can be divided into three main parts, i.e., *short*-, *intermediate*-, and *long-range ordering*. *Short-range order* refers to the nearest neighbor distances corresponding to the basic structural unit(s). The connectivity of these structural units also falls within the realm of short-range order. For example, in the case of well-crystallized γ-MnS the basic structural unit is the MnS_4 tetrahedron (**Figure 1**). The structure of this basic unit (tetrahedron) and the corner-sharing connectivity of it to neighboring units are defined by the short-range order. Associated with *intermediate-range ordering* is the presence of larger correlations of several

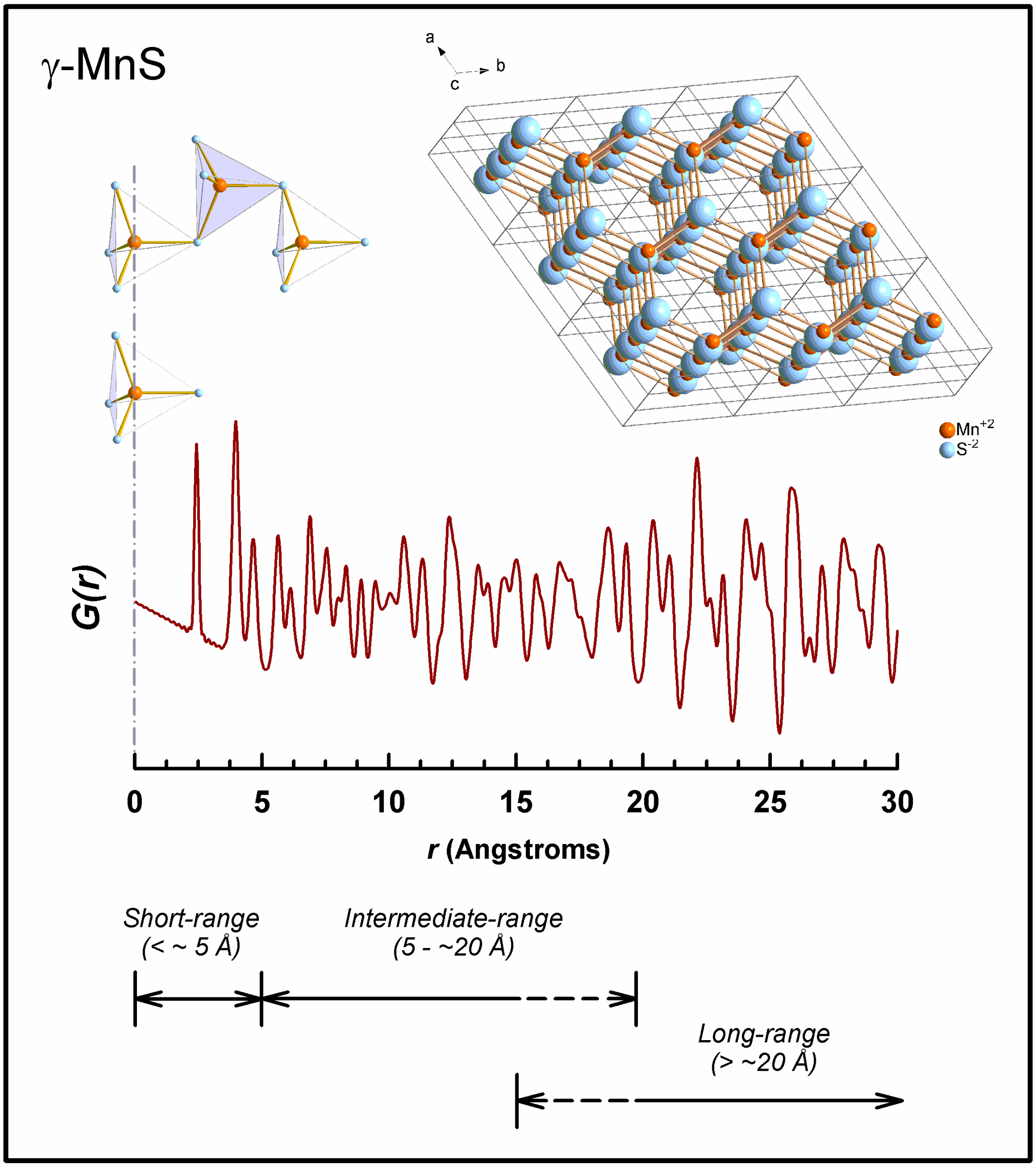

Figure 1: Calculated PDF, or *G(r)*, plotted against distance *r* for γ-MnS. The calculation is based on spacegroup $P6_3mc$ and the structural details reported in ICSD# 44765 (*16*). The first correlation in the PDF at ~2.4 Å corresponds to the average Mn-S distance in the MnS_4 tetrahedron. This and the corner-sharing connectivity of the tetrahedra are defined by the short-range order. The intermediate range ordering to ~15 Å reflects the overall topology of the structure. The long-range ordering describes the extended periodicity of the topology and extends from ~20 Å *ad infinitum*.

structural units. In real space this is usually characterized by a distance range of 10-20 Å. Studies of glasses and liquids, considered as being truly amorphous, have revealed that while all exhibit short- range order, some also possess intermediate-range order by forming cages, rings, chains, and other structures (*13*). In the case of γ-MnS (**Figure 1**) the overall topology of the structure is contained in the intermediate range ordering and is characterized by a simple ABAB stacking sequence. *Long-range order* is generally not applicable to glasses or liquids. In terms of scattering, long-range periodicity generally results in the well-defined Bragg peaks, as are observed in powder diffraction patterns of well-crystallized solids, and this phenomenon has been exploited for many years in structure determination. Long-range order is synonymous with infinite periodicity but does not only apply to macro-sized crystals. As shown in several of the subsequent chapters in this dissertation, certain nanocrystalline solids with finite particle sizes as small as 20 Å also exhibit a limited degree of periodicity. Despite this limited periodicity and lack of well-defined Bragg features, they are sufficiently ordered to be described using a unit cell when examined using a method well-suited to evaluating nanocrystalline structure.

X-ray and Neutron Diffraction

The diffraction pattern of a well-crystallized material is a robust source of information for characterization, phase identification, and the extraction of quantitative structural details. For known structure types, the most commonly sought information includes the identification and relative abundances of phases, unit cell dimensions, atomic positions, occupancies, and displacement parameters. This structural information is extracted primarily through assessment of the sharp diffraction maxima, resulting from Bragg scattering of X-rays or neutrons. Using established refinement methods such as Rietveld analysis (*14, 15*), the Bragg scattering component yields information regarding the long-range periodicity of a material. Tens of thousands of crystalline solids have been characterized using standard diffraction methods and catalogued in databases such as the Inorganic Crystal Structure Database (ICSD) (*16*) and Cambridge Structural Database (*17*) for organic compounds. These structure databases are routinely searched in order to find structures that best match features observed in diffraction patterns of single or multiphases samples. For an unknown compound, diffraction is also a powerful tool for structure determination using Fourier methods, Patterson interpretation, direct methods, or simply trial and error (see (*18*) for review). Again, the successful determination of structure depends on the extraction of sufficient information from the Bragg component.

Contrary to what is observed for well-crystallized compounds, diffraction from nanosized particles (< ~100 nm) produces patterns characterized by broadened and often convoluted diffraction maxima (*19*) and with a significant component of underlying diffuse scattering (*20, 21*). This broadening effect is primarily size-induced and affects the Bragg component becoming particularly pronounced for particle sizes < ~10 nm (e.g., (*22*)). Structure determination and refinement for nanocrystalline materials is additionally complicated when this size-induced broadening is coupled with surface relaxation, strain, and disorder (static and/or dynamic). These complex effects are generally manifested as diffuse scattering and often appear to simply increase the amount of background in a pattern. As discussed below, the diffuse scattering from a nanosized material with limited long-range periodicity (i.e., nanocrystalline) contains important information regarding the short- and intermediate-range structure. The general lack of well-defined Bragg maxima in the diffraction patterns for nanocrystalline compounds hinders quantitative structure determination and refinement by conventional methods which rely exclusively on these features.

Scanning and Transmission Electron Microscopy

Electron microscopes facilitate the probing of fine scale objects using a beam of highly energetic electrons (see (*23*) for review). The basic principle of SEM is that an energy exchange occurs between the electron beam and the sample and results in the emission of electrons and electromagnetic radiation. Detectors for measuring the secondary and backscattered electrons from the sample surfaces are used both to produce an image of the specimen and provide compositional information, respectively. For the examination of particles less than ~100 nm, the TEM is often preferable. The basic principal in the case of the TEM is that the beam of electrons is transmitted from the sample, magnified, and then recorded using photographic film or digital imaging. These instruments provide a powerful and direct method for obtaining information regarding particle size and morphology.

In the case of nanoparticles, the TEM is not only a versatile tool for obtaining information in real-space (directly from images) but also in reciprocal space (diffraction) (*24*). In regards to the latter, there are two basic approaches. In one, a nearly parallel beam of electrons as small as ~100 nm in diameter is used to perform selected-area electron diffraction (SAED) on single or multiple particles. While SAED is feasible on individual crystals, it becomes problematic when the maximum particle dimensions are significantly less then the size of the beam (i.e., << 100 nm) (*25*). Therefore, in the case of nanosized particles (< 10 nm) SAED is instead performed by illuminating with the electron beam groups of particles aggregated with various orientations. As expected, the diffraction pattern resulting from scattering of many particles is characterized by rings rather than spots. The second approach applies primarily to diffraction on extremely small individual crystals and is usually referred to as convergent-beam electron diffraction (CBED), or simply nanodiffraction (*25, 26*). In principal, a convergent beam of electrons covering a range of incident angles can be focused to a spot size less than 1 nm in diameter. When directed at an individual particle the scattering generated results in a disc diffraction pattern and contains information regarding the structure. However, since it is not possible to tilt an individual crystal to any particular orientation, many diffraction patterns are obtained on many different particles, each with a different orientation. Whether performing SAED or nanodiffraction, the resulting electron diffraction pattern (rings or discs) is ultimately treated in a manner synonymous with using standard XRD structure determination and analysis methods. Under ideal circumstances, the Bragg features are identified and then matched to known structure types or indexed and structural information is obtainable.

X-ray Absorption Spectroscopy

X-ray absorption spectroscopic (XAS) methods provide a variety of element-specific information including oxidation state and local coordination environment (see (*27, 28*) for comprehensive reviews and applications). The principal of XAS is that an atom absorbs X-rays at defined energies which correspond to the binding energies (E_0) of its electrons. The X-ray absorption spectrum is generally divided into two spectral regions, the first includes the pre-edge ($E < E_0$) and X-ray absorption near-edge structure (XANES) ($E = E_0 \pm 10$ eV), and the second is the more distant extended X-ray absorption fine structure (EXAFS) region (~10 eV to ~1000 eV above E_0). A typical XANES experiment measures the photoelectron intensity as a function of photon energy in the immediate vicinity of the absorption edge. The features in the low-energy pre-edge and XANES spectral region result from electronic transitions to empty or partially-filled higher orbitals. The intermediate XANES spectral region includes the absorption edge and is dominated by multiple scattering resonances of ejected photoelectrons with low kinetic energies. This region is therefore rich in chemical information such as oxidation state and site symmetry for the absorber atom.

In the EXAFS spectral region, the excitation of electrons above the main absorption edge causes photoelectrons to be ejected into the continuum from the absorbing atom and thereby interact with surrounding atoms in the material (*29*). EXAFS is element-specific and these scattered photoelectrons result in an interference pattern which is used to obtain information on the number, type, and distance to neighboring atoms. EXAFS is considered a local probe of structure because the limited mean free path of an ejected photoelectron is typically less than ~5 Å (e.g., (*30*)). In combination with spectra for known reference materials, EXAFS is routinely used for phase identification in multiphase or heterogeneous materials. For pure samples, EXAFS can in certain cases be used to compare and even build structure models, particularly for amorphous solids (*31*) and liquids (*32*).

Total Scattering and Pair Distribution Function Analysis

Total scattering experiments using X-rays for pair distribution function (PDF) analysis have been performed for over 80 years and historically were applied to the structures of liquids and amorphous solids (e.g., (*33-35*), see (*36*) for review). Total scattering implies the collection of all the elastic scattering from a sample and includes both the Bragg and diffuse components. While the Bragg component contains information on long-range ordering in crystalline materials, the diffuse component results from imperfections in the crystal lattice. Thus, the PDF technique has more recently been applied to the study of disorder in crystalline solids (e.g., (*21, 37-39*)). Furthermore, by not relying solely on the Bragg scatter, this method does not automatically exclude nanosized materials that have limited periodicity due to finite particle sizes and complex disorder.

In the case of X-rays, total scattering experiments are typically carried out at synchrotron facilities because of the need for high energies to measure over a wide range of momentum transfer (Q), where $Q = 4\pi\sin\theta/\lambda$ for elastic scattering. This wide range is important because the resolution of the PDF in real-space is directly related to the range of Q over which data are measured. The resolution in real-space can be approximated as $\delta r = \pi/Q_{max}$ where Q_{max} corresponds to the maximum Q-value (*20, 40*). The collection of high-Q values (>20 $Å^{-1}$) are easily obtainable using short wavelength X-rays and thus, the incident radiation used is typically >75 keV. For comparison, a laboratory X-ray source using Cu (λ = ~1.54 Å) provides data to a maximum Q-values of ~10 $Å^{-1}$. Shorter wavelengths and higher Q-values are possible using sources such as Ag (λ = ~0.4 Å), however the peak-to-background ratio at high-Q tends to be poor due to the low intensity of the incident radiation. Fortunately, the intense X-rays available at a synchrotron facility lead to favorable peak-to-background ratios, which are particularly important in the high-Q region dominated by the relatively weak diffuse scattering component. Although data from laboratory sources can be used to generate PDFs (e.g., (*41*)), the limited Q-range and relatively poor peak-to-background discrimination reduces both the accuracy and resolution (*36*). The same principal of collecting data to high-Q values applies to neutron total scattering measurement performed at pulsed neutron sources (e.g., (*42-44*)). Since the total scattering data presented in this dissertation were exclusively collected using X-rays, the differences between neutrons and X-rays for total scattering measurements are not discussed here but are reviewed elsewhere (*20*). The equations presented below are from Billinge (2003) and are also found in detail in (*20*).

The atomic PDF, $G(r)$, is defined as

$$G(r) = 4\pi r[\rho(r) - \rho_o], \tag{1}$$

where r is radial distance (e.g., from a central atom to a neighboring atom), ρ_0 is the average atomic number density, $\rho(r)$ is the atomic pair-density defined in Equation (2).

The PDF contains the real-space distribution of interatomic distances in a material and is obtained from the Fourier transform of the measurable diffraction intensities. The relationship of *G(r)* to the measured diffraction pattern (X-rays or neutrons) is through a Fourier transform

$$G(r) = (2/\pi) \int_{Q=o}^{Q_{\max}} Q[S(Q) - 1] \sin(Qr) dQ, \tag{2}$$

where *S(Q)* is the total scattering structure function and contains the measured scattering intensity. The total scattering structure function *S(Q)* is commonly displayed as the reduced structure function *f(Q)*, or *Q*[*S(Q)* – 1]. The experimental structure function is related to the coherent part of the total diffracted intensity,

$$S(Q) = \frac{I^{coh}(Q) - \sum c_i |f_i(Q)|^2}{\left|\sum c_i f_i(Q)\right|^2} + 1 \tag{3}$$

where $I^{coh.}(Q)$ is the properly corrected measured scattering intensity from a powder sample. In Equation 3, c_i and f_i are the atomic concentration and X-ray atomic form factor, respectively, for the atomic species of type *i* (*20, 45*). The geometry of the setup for a total scattering experiment is relatively straightforward (**Figure 2**). The scattered intensities are measured in Debye-Scherrer geometry using a 2-D plate-style detector. The applications of standard corrections for X-rays as well as those unique to the 2-D image-plate geometry are reviewed elsewhere (*46*).

While structural information can be extracted directly from the PDF, there are also a number of possible modeling strategies available. Modeling using periodic structures is straightforward because PDFs can be calculated directly from structure models and fitted to experimental data using a regression program (e.g., (*47*)). In this case, a highly constrained "Rietveld-like" refinement is performed on the PDF in which the unit cell dimensions, atomic positions, displacement, occupancy, and other model dependent parameters are varied to improve the fit between the observed and calculated PDF (*20*). For amorphous solids or liquids periodic structures do not apply and reverse Monte Carlo (RMC) simulations (*48*) are commonly applied instead. RMC is also a useful tool in the modeling of disorder in periodic structures (see (*20*) for summary).

The PDF method also provides a useful tool for probing the average coherent scattering domain size of nanocrystalline materials through evaluation of PDF attenuation

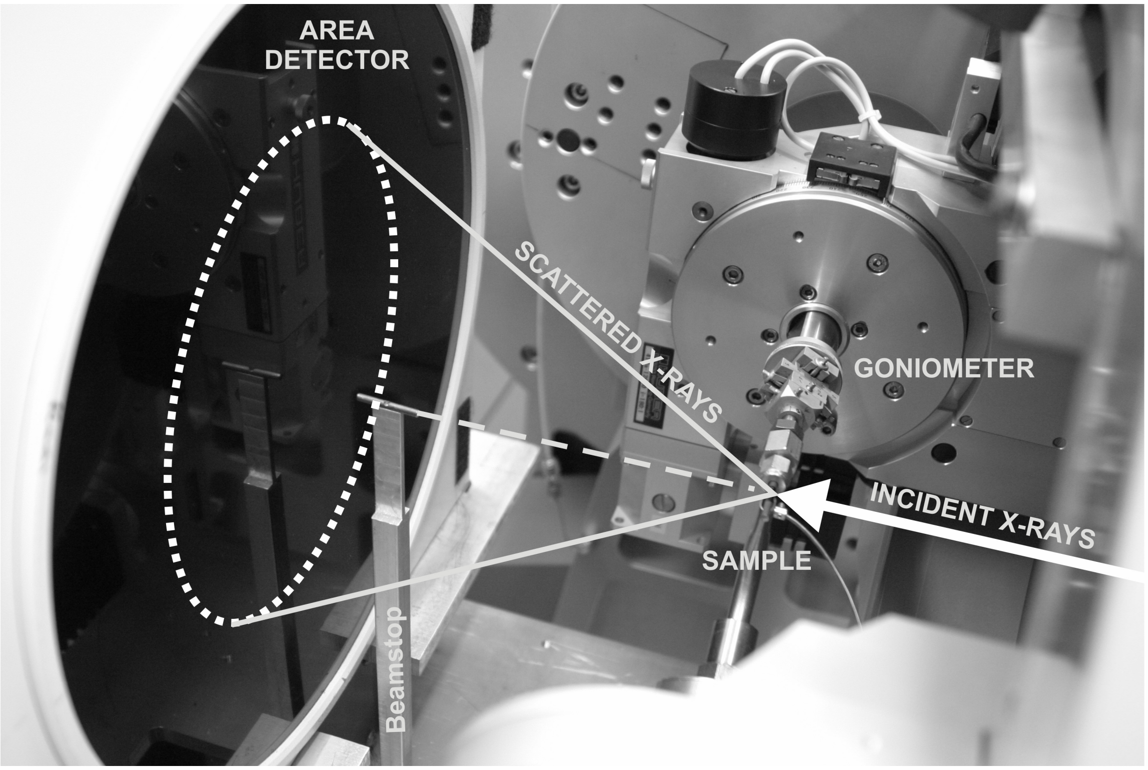

Figure 2: Geometry typical of a high-energy X-ray total scattering experiment at the Advanced Photon Source at Argonne National Laboratory. The incident beam of high-energy X-rays interacts with a sample loaded in a capillary and mounted in the goniometer. The scattered X-rays are collected in Debye-Scherrer geometry using a 2-D plate-style detector (shown above) or by using a scanning point counter. A beamstop is used to prevent damage to the detector from the portion of the incident beam continuing beyond the sample (long dashes).

(*49*). In principal, the average coherent domain size might correspond to the average particle size as was demonstrated in the case of gold nanoparticles (*50*). However, particle morphology (*51*) and/or the presence of structural disorder (e.g., static and/or strain) at the surface or the interior of a nanocrystalline phase (*52*) can also affect the PDF. These effects are complex and not fully understood but are anticipated to result in an underestimate of the average crystallite size through the range of structural coherence. In regards to particle size, the polydispersity of a sample must also be considered and therefore, the use of a separate technique, such as direct imaging by electron microscopy, is often necessary to corroborate size estimates from PDF.

Limitations of Structure Determination Methods

A complete description of the atomic arrangement of a nanoparticle ideally includes the interior "bulk" structure, the structure at and near the surfaces, and any additional disorder and defects throughout the particle. Although the X-ray spectroscopy and scattering methods described above provide specific structural and chemical information there is currently no single method for evaluating the entire atomic arrangement of any given nanocrystalline material. In general, this is a consequence of one or more limiting factors for each method. For example, when using conventional XRD methods, nanosized particles and complex disorder produce negative effects on data quality. The most striking aspect of a diffraction pattern for a nanosized material is that the maxima do not appear as sharp peaks with a high peak-to-background ratio. Rather, the maxima are broad and overlapping with a significant underlying diffuse scattering component. The lack of distinct features often makes indexing the pattern not feasible and therefore hinders determination of lattice parameters and space group symmetry. This diffuse scatter contains critical information regarding the short- and intermediate-range ordering of a material and is treated as background during Rietveld refinement.

Electron nanodiffraction also has certain limitations in regards to structure determination of nanoparticles and becomes unreliable for materials that are unstable under high vacuum and a focused electron beam. Structure determination by electron diffraction is synonymous with XRD since both rely on clearly defined diffraction maxima (rings or discs). Further, the analysis of electron diffraction data focuses on the

Bragg scattering component while the diffuse background is removed. As with XRD, the information treated as background is related to short- and intermediate range ordering and is essential to comprehensively evaluating structure in nanosized particles. Therefore, this method is most useful for materials which exhibit extended periodicity.

Sample heterogeneity must also be considered when utilizing nanodiffraction in the derivation of a structure model for an unknown phase. This is mainly the case for nanodiffraction of single-crystals since the ability to tilt a specimen relative to the beam is restricted and is typically < 5 degrees in any direction. Thus, structural information is not obtained for a single particle, but done by evaluating a large number of crystallites in various orientations. It is clear that sample heterogeneity would severely hinder developing an accurate and complete structure model for an unknown phase. However, it should be noted that sample heterogeneity not only complicates analysis by nanodiffraction, virtually all techniques for structure determination including scattering, diffraction, and spectroscopy suffer in this respect.

The effects of electron beam damage to a sample must also be considered, particularly for unstable samples that may experience change under high vacuum. In a recent study using electron energy loss spectroscopy (EELS) to evaluate the effects of electron beam damage to ferrihydrite, Pan *et al.* (*25*) observed the reduction of Fe^{3+} to Fe^{2+} and a migration of Fe from octahedral to tetrahedral sites with increasing electron dose. These results highlight how investigations carried out under the high vacuum and focused electron beam of the transmission electron microscope may cause significant, and perhaps undetected, changes to occur in a sample.

In the case of EXAFS, the main limitation to discriminating between potential structural models or deriving a new structure model for an unknown compound is the range of information obtained. As mentioned earlier, the mean free path of an ejected photoelectron is typically < ~5 Å which means that its interaction with neighboring atoms is generally limited to the first and second coordination shells. This is potentially problematic if attempting to differentiate between compounds with similar compositions and which exhibit similar short-range ordering. For example, in the Fe-O-H system there are several structures (e.g., goethite, akaganéite, lepidocrocite) that have edge and corner sharing FeO_6 octahedra and thereby would result in similar radial distribution functions

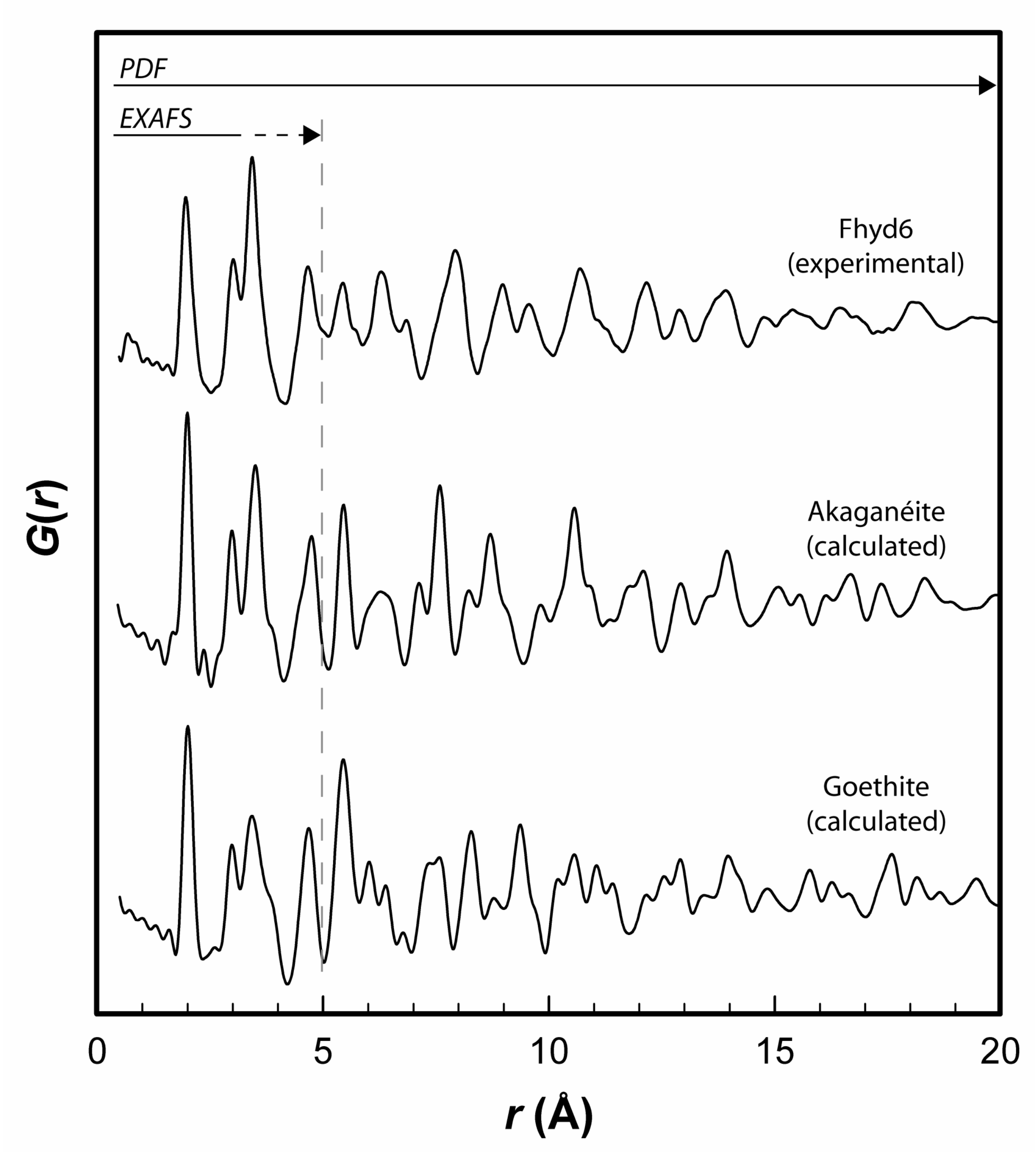

Figure 3: The experimental PDF *G(r)* versus distance *r* is plotted for a synthetic sample of 6 nm ferrihydrite (Fhyd6). Calculated PDFs for akaganéite and goethite are also plotted to show the similarities in the atom-atom distances over the first ~5 Å, typical of the range of distances reported by EXAFS.

out to ~5 Å (**Figure 3**). Despite possessing substantially different overall topologies, the first two coordination shells may appear virtually identical in terms of coordination number and distance. For nanoparticles this could potentially become even more challenging due to the added complexity of disorder and defects. The total scattering and PDF method differs from traditional analysis methods of XRD data (e.g., Rietveld) in that it requires no presumption of periodicity and yet yields direct information on the local, intermediate and long-range order (if present). In reciprocal space, diffraction data of amorphous and nanocrystalline materials appear as broad maxima with a substantial diffuse component. By Fourier transforming the measured total scattering intensity and evaluating the atomic arrangement in real-space using the PDF method, the broadening dilemma is avoided. However, the usefulness of the PDF for extracting quantitative structural information directly or through modeling is dependent on the quality and treatment of the data. Accurately measured scattering positions and intensities and a sufficiently high Q_{max} are paramount in total scattering experiments. This applies equally to both the measurement of the sample and the independent background. Other aspects such as the relative insensitivity of high-energy X-rays to lighter elements (e.g., hydrogen), and the negative impact of certain systematic and random errors during data analysis must all be considered. Detailed discussions on these topics are available elsewhere (*20, 40*).

Additional Experimental Methods

Colorimetry

Determining the concentration of a chemical in solution is possible if it has a color by use of colorimetry (see (*53*) for comprehensive review). A typical experiment involves measuring the absorbance of particular wavelengths of light and relating the degree of absorbance to concentration. Since most species do not have inherent color in solution, it is common for color to be derived by addition of another reagent. For example, the total iron content of a dissolved solid can be determined using the FerroZine test. In an aqueous sample properly buffered for pH, the FerroZine iron reagent forms a purple-colored complex with trace amounts of iron. In this case, the color change is directly proportional to the concentration of iron and is determined using the calibration curve (absorbance versus concentration) according to Beer's-Lambert Law. Colorimetry is a versatile method for determining concentrations on a wide variety of chemicals.

Thermogravimetric Analysis

Thermogravimetric analysis (TGA) involves measuring weight loss of a substance with temperature. In dehydration reactions changes in weight are observed when a loss of stoichiometric water and/or hydroxyl groups occurs (see (*54*) for review). Weight losses associated with reactions forming carbon dioxide, for example in the decomposition of calcite ($CaCO_3$) to calcium oxide and carbon dioxide (*55*), are also commonly measured. Additionally, measuring weight losses due to the oxidation of transition metals such as iron or manganese are possible (e.g., (*56*). During a thermal analysis experiment the three parameters that require precise measurement are temperature, weight, and temperature change. A well characterized, thermally-inert material such as α-Al_2O_3 is commonly measured for reference and for correction (e.g., instrument drift). Interpretation of TGA data may be complicated for samples where the reactions occurring are overlapping or occur with subtle rather than dramatic weight loss. Differential scanning calorimetry (DSC) is often done in conjunction with TGA as it provides information regarding the difference in the amount of heat required to increase the temperature of a sample. Exothermic and endothermic reactions associated with phase transitions are generally manifested as well defined features in DSC plots and often are useful in the interpretation of TGA data.

Dynamic Light Scattering

Dynamic light scattering (DLS) is a noninvasive technique for measuring the size and electrophoretic mobility of particles in solution (see (*57*) for review). Only the former was used as part of this dissertation and will be introduced. In brief, small particles in solution will scatter an incident beam of light (usually laser light) in all directions. The inherent vibration of particles in solution, also known as Brownian motion, results in intensity fluctuations in the scattered light measured by a detector. This movement of particles leads to a combination of constructive and destructive interferences for the scattered light which contains information regarding the time scale of movement of the particles. During an experiment the autocorrelation of the intensity trace is recorded. Particle size distributions are based on this measured autocorrelation function and calculated using analysis procedures such as CONTIN (*58*) and non-negative least squares (*59*). While this method is very reliable for evaluating monodisperse colloids, it is often less robust for polydisperse samples. Therefore, additional techniques for determining size such as direct imaging using electron microscopy are often necessary in conjunction with DLS.

References

1. R. R. Patterson, S. Fendorf, M. Fendorf, *Environmental Science & Technology* **31**, 2039 (1997).

2. K. A. Quinn, R. H. Byrne, J. Schijf, *Environmental Science & Technology* **41**, 541 (2007).

3. F. Zuo, B. Zhang, X. Z. Tang, Y. Xie, *Nanotechnology* **18** (2007).

4. R. B. Neder, M. Burghammer, T. Grasl, H. Schulz, *Zeitschrift Fur Kristallographie* **211**, 365 (1996).

5. R. B. Neder *et al.*, *Zeitschrift Fur Kristallographie* **211**, 763 (1996).

6. J. W. Akitt, *NMR and Chemistry, An Introduction to the Fourier Transform-Multinuclear Era* (Chapman and Hall, London, ed. 2, 1983), pp. 263.

7. G. Calas, F. C. Hawthorne, in *Reviews in Mineralogy*. (1988), vol. 18, pp. 1-9.

8. P. McMillan, in *Reviews in Mineralogy*. (1985), vol. 14, pp. 9-63.

9. D. Steele, *Theory of Vibrational Spectroscopy* (W. B. Saunders London, 1971), pp. 226.

10. D. L. Price, *Current Opinion in Solid State & Materials Science* **1**, 572 (1996).

11. A. C. Wright, *American Ceramic Society Bulletin* **58**, 380 (1979).

12. A. C. Wright, G. A. N. Connell, J. W. Allen, *Journal of Non-Crystalline Solids* **42**, 69 (1980).

13. M. C. Wilding, C. J. Benmore, in *Reviews in Mineralogy & Geochemistry*. (2006), vol. 63, pp. 275-311.

14. H. M. Rietveld, *Acta Crystallographica* **22**, 151 (1967).

15. H. M. Rietveld, *Journal of Applied Crystallography* **2**, 65 (1969).

16. E. Fluck, *Journal of Research of the National Institute of Standards and Technology* **101**, 217 (1996).

17. F. H. Allen, R. Taylor, *Chemical Society Reviews* **33**, 463 (2004).

18. G. H. Stout, L. H. Jensen, *X-ray Structure Determination. A Practical Guide* (John Wiley, New York, ed. 2, 1968), pp. 480.

19. H. P. Klug, L. E. Alexander, *X-ray Diffraction Procedures for Polycrystalline and Amorphous Materials* (Wiley Interscience, New York, ed. 2nd, 1974), pp. 992.

20. T. Egami, S. J. L. Billinge, *Underneath the Bragg Peaks: Structural Analysis of Complex Materials*. R. W. Cahn, Ed., Pergamon Materials Series (Elsevier, Oxford, 2003), pp. 404.

21. V. Petkov *et al.*, *Physical Review B* **65** (2002).

22. X. D. Zhou, W. Huebner, *Applied Physics Letters* **79**, 3512 (2001).

23. S. L. Flegler, J. W. Heckman, K. L. Klomparens, *Scanning and Transmission Electron Microscopy: An Introduction* (Oxford University Press, Oxford, 1995), pp. 240.

24. L. A. Bendersky, F. W. Gayle, *Journal of Research of the National Institute of Standards and Technology* **106**, 997 (2001).

25. J. W. Steeds, J. P. Morniroli, *Reviews in Mineralogy* **27**, 37 (1992).

26. J. P. Morniroli, J. W. Steeds, *Ultramicroscopy* **45**, 219 (1992).

27. G. E. Brown, G. Calas, G. A. Waychunas, J. Petiau, in *Reviews in Mineralogy & Geochemistry*. (1988), vol. 18, pp. 431-512.

28. D. C. Koningsberger, R. Prins, Eds., *X-ray Absorption: Principles, Applications, Techniques of EXAFS, SEXAFS, and XANES* (John Wiley & Sons, New York, 1988), pp. 684.

29. D. E. Sayers, E. A. Stern, F. W. Lytle, *Physical Review Letters* **27**, 1204 (1971).

30. E. A. Stern, S. M. Heald, in *Handbook of Synchrotron Radiation* E. E. Koch, Ed. (North Holland, New York, 1983), vol. 1b, pp. 955-1014.

31. G. N. Greaves, *Journal of Non-Crystalline Solids* **71**, 203 (1985).

32. A. Filipponi, *Journal of Physics-Condensed Matter* **13**, R23 (2001).

33. P. Debye, H. Menke, *Physikal. Zeit.* **31**, 797 (1930).

34. R. Kaplow, B. L. Averbach, S. L. Strong, *Journal of Physics and Chemistry of Solids* **25**, 1195 (1964).

35. R. Kaplow, T. A. Rowe, B. L. Averbach, *Physical Review* **168**, 1068 (1968).

36. S. J. L. Billinge, *Zeitschrift Fur Kristallographie* **219**, 117 (2004).

37. V. Petkov, S. J. L. Billinge, S. D. Shastri, B. Himmel, *Journal of Non-Crystalline Solids* **293**, 726 (2001).

38. V. Petkov, R. G. DiFrancesco, S. J. L. Billinge, M. Acharya, H. C. Foley, *Philosophical Magazine B-Physics of Condensed Matter Statistical Mechanics Electronic Optical and Magnetic Properties* **79**, 1519 (1999).

39. M. G. Tucker, M. P. Squires, M. T. Dove, D. A. Keen, *Journal of Physics-Condensed Matter* **13**, 403 (2001).

40. B. H. Toby, T. Egami, *Acta Crystallographica Section A* **48**, 336 (1992).

41. R. E. Franklin, *Acta Crystallographica* **3**, 107 (1950).

42. S. J. L. Billinge, T. Egami, *Physical Review B* **47**, 14386 (1993).

43. S. J. L. Billinge, M. G. Kanatzidis, *Chemical Communications*, 749 (2004).

44. T. Proffen *et al.*, *Applied Physics a-Materials Science & Processing* **74**, S163 (2002).

45. B. E. Warren, *X-ray Diffraction* (Dover, New York, 1990), pp. 381.

46. P. J. Chupas *et al.*, *Journal of Applied Crystallography* **36**, 1342 (2003).

47. C. L. Farrow *et al.*, *Journal of Physics: Condensed Matter* **19**, 335219 (2007).

48. R. L. McGreevy, L. Pusztai, *Molecular Simulation* **1**, 359 (1988).

49. B. D. Hall, D. Zanchet, D. Ugarte, *Journal of Applied Crystallography* **33**, 1335 (2000).

50. K. Page *et al.*, *Chemical Physics Letters* **393**, 385 (2004).

51. K. Kodama, S. Iikubo, T. Taguchi, S. Shamoto, *Acta Crystallographica Section A* **62**, 444 (2006).

52. B. Gilbert, F. Huang, H. Z. Zhang, G. A. Waychunas, J. F. Banfield, *Science* **305**, 651 (2004).

53. B. Ohta, A. Robertson, *Colorimetry: Fundamental and Applications* (John Wiley & Sons, 2006), pp. 350.

54. P. J. Haines, Ed., *Principles of Thermal Analysis and Calorimetry* (Royal Society of Chemistry, Cambridge, 2002), pp. 220.

55. G. T. Faust, *American Mineralogist* **35**, 207 (1950).

56. M. I. Zaki, M. A. Hasan, L. Pasupulety, K. Kumari, *Thermochimica Acta* **303**, 171 (1997).

57. B. Chu, *Laser Light Scattering: Basic Principles and Practice* (Academic Press, San Diego, 1991), pp. 165.

58. S. W. Provencher, *Computer Physics Communications* **27**, 213 (1982).

59. I. D. Morrison, E. F. Grabowski, C. A. Herb, *Langmuir* **1**, 496 (1985).

Chapter 3: The Short- to Medium-Range Atomic Order and Crystallite Size of the Initial FeS Precipitate from Pair Distribution Function Analysis

Reproduced with permission from Chemistry of Materials:

F. M. Michel [a,b], S. M. Antao [a,b], P. J. Chupas [d], P. L. Lee [d], J. B. Parise [a,b,c], M. A. A. Schoonen [a,b] (2005) The Short- to Medium-Range Atomic Order and Crystallite Size of the Initial FeS Precipitate from Pair Distribution Function Analysis, Chem. Mater., 17, 6246-6255, doi: 10.1021/cm050886b.

[a] *Center for Environmental Molecular Science (CEMS)*
[b] *Department of Geosciences, Stony Brook University, Stony Brook, New York 11794*
[c] *Department of Chemistry, Temple University, Philadelphia, Pennsylvania 19122*
[d] *Advanced Photon Source, Argonne National Laboratory, Argonne, Illinois 60439*

Abstract

Pair distribution function analysis (PDF) of X-ray diffraction data, collected at 11-IDC and 1-ID at the Advanced Photon Source, provides the atomic structure and primary crystallite size of FeS both freshly precipitated (FeS_{fresh}) and aged (FeS_{aged}). The short- to medium-range structure of both FeS_{fresh} and FeS_{aged} are nearly identical with that of highly crystalline (bulk) mackinawite. Attenuation in the observed range of structural coherence of the PDF for FeS_{fresh} indicates an average crystallite size on the order of ~2 nm. This range of structural coherence increased with aging of the sample under hydrothermal conditions due to growth of the individual crystallites, although the mechanism by which this growth occurs is not clear at present. Electron microscopic imaging confirms the presence of individual nano-scale crystallites and provides some insight into their aggregation behavior as larger clusters. The initial, fresh precipitate does not exhibit long-range atomic structure because it is nanocrystalline. The so-called X-ray amorphous nature of FeS_{fresh} is the result of the limited range of structural coherence imposed by the size of the individual crystallites rather than the result of a lack of medium- and long-range atomic order. We propose that the discrepancies in the

literature over crystallite size and the atomic structure of FeS_{fresh} are due primarily to the varying degrees of aggregation of uniformly-distributed and nanocrystalline FeS particles.

Introduction

The properties of the Fe - S system are of major interest and importance in environmental, geological, and planetary science. In Earth's crust, pyrite (FeS_2) formation from so-called disordered or amorphous FeS is a key process in several geochemical cycles (*1*). FeS is environmentally significant in the sequestration and remobilization of heavy metal contaminants such as Cu, Cd (*2*), As (*3*), Ni, and Co (*4*) and has recently been shown to react with contaminants such as dissolved $Cr^{(VI)}$ species (*5*). FeS is also an important product during diagenesis in marine sediments. Hydrogen sulfide, produced by sulfate-reducing bacteria, reacts with iron sources within the sediments to form FeS (*6, 7*). The first step in the formation of iron sulfides under aqueous conditions is the nucleation of a reduced, short-range-ordered iron monosulfide (FeS_{fresh}) that is generally believed to be a precursor to crystalline (bulk) mackinawite (*8*). Subsequently, mackinawite itself serves as a precursor to the stable Fe - S phase, pyrite. A structure model for the initial FeS precipitate is required as a first step to studying the consequences of its formation, transformation and reactivity under varying conditions, as well as the sequestration of contaminants. Until this study, the short- to medium-range crystal structure and primary crystallite size of the initial FeS precipitate, often referred to in the Earth science literature as amorphous FeS, had not yet been resolved.

Experimental

FeS was formed in this study by the reaction of ferrous iron with sulfide in aqueous solution at room temperature (22 ± 2 °C). The initial precipitate formed by mixing the iron and sulfide solutions will hereafter be referred to as freshly precipitated FeS or simply FeS_{fresh}. The precipitation reaction was conducted at pH values varying between ~5 and ~9. Both wet and dry samples of the FeS_{fresh}, as well as an aged precipitate (hereafter referred to as FeS_{aged}) were examined. Due to an absence of well-defined Bragg reflections in FeS_{fresh} and FeS_{aged}, atomic pair distribution function (PDF) analysis was used as a structural probe. This technique, originally developed to investigate the short- to medium-range atomic order in liquids and glassy materials, has been described in detail elsewhere (*9, 10*). In short, the PDF enables the gathering of three important pieces of information about pairs of atoms in the structure of interest: the peak position indicating the average distance separating the pair; the integrated intensity of each peak yielding number of coordinated atoms; and the width and shape of the peak indicating the static and/or dynamic disorder in the pair. Additionally, the range of the PDF indicates the size of coherently scattering structural domains and therefore, in certain cases, provides a means for determining average primary crystallite sizes (*11-14*). As it has been historically described as an X-ray amorphous material (*15-17*), the scattering from FeS_{fresh} was presumed to be generally weak, especially if in the presence of an aqueous solution. Therefore, a requirement of the study was to collect data of sufficient quality, across a wide range of momentum transfer (Q) to obtain a properly normalized total scattering structure function $S(Q)$ and pair distribution function $G(r)$. The purpose was to go beyond fingerprinting, by comparing diffraction patterns, to deriving testable structure models by fitting the real-space $G(r)$ derived from the scattering data. Without properly normalized $S(Q)$ this refinement of competing models is not possible. A sufficient range of $S(Q)$ requires use of intense, monochromatic, high energy X-rays available at the Advanced Photon Source (APS), a third generation synchrotron source.

Chemicals:

$Fe(NH_4)_2(SO_4)_2 \cdot 6H_2O$ (Mohr's Salt) Fisher Chemicals (99.4 %); $Na_2S \cdot 9H_2O$ (NaSH/NaOH or sulfide) Fisher Chemicals (99 %); $C_8H_5O_4K$ (potassium hydrogen phthalate) Aldrich (+99.5 %); KCl J.T. Baker (+99 %); HCl Fisher Chemicals (Certified A.C.S. Plus); NaOH (pellets) J.T. Baker (98.8 %); CH_3COOH (acetic acid) Fisher Chemicals; Iron wool (super fine #0000) Rhodes American. Buffer solutions of pH 4 were prepared by the addition of 50 ml 0.1 M potassium hydrogen phthalate to 0.1 ml 0.1 M HCl. Buffer solutions of pH 12 were prepared by the addition of 25 ml 0.2 M KCl to 6 ml 0.2 M NaOH. All of the chemicals were analytical grade and were used as received without additional purification. All solutions were prepared using water that was deionized (EasyPure®, filtered 0.2 μm, UV/UF) and purged with N_2 (99.99 % pure) for at least 30 minutes to remove dissolved molecular oxygen (*18*). All solutions were prepared at room (22 ± 2 °C) temperature in an anaerobic glove box purged with a mixture of N_2 (97 %) and H_2 (3 %) and equipped with a CoyLabs oxygen removal system and digital O_2 and H_2 analyzer/indicator. Sample FeS-E was an exception and is described below.

Syntheses:

All FeS samples (except FeS-Bulk) were synthesized by direct injection of 0.3 M ferrous ammonium sulfate solution (Mohr's salt) into 0.3 M sulfide (NaSH/NaOH) solution with a ratio of approximately 1:1. This common method of precipitating so-called amorphous FeS from solution was described initially by Rickard (*19*). In some cases a pH 4 or pH 12 buffer solution was added to the sulfide solution prior to the addition of the Mohr's salt solution to lower or increase, respectively, the pH at the time of precipitation (*8*). Highly crystalline (bulk) FeS was synthesized according to the method described by Lennie *et al.* (*20*) and involved the reaction of metallic iron and sulfide. It is important to note that great care was taken to minimize the potential for oxidation of the synthetic FeS by exposure to atmospheric oxygen. All syntheses were carried out at room temperature (22 ± 2 °C) and in a glove box (excluding FeS-E) under a completely anoxic H_2-N_2 atmosphere. The anoxic H_2-N_2 atmosphere in the chamber was maintained using a Pd-catalyst and monitored continuously with a dedicated, real-time oxygen/hydrogen sensor. Sample identification and an overview of synthesis conditions are outlined in **Table 1**.

Fresh Precipitates - Dry (FeS-A$_{(pH\ 5.3)}$, FeS-B$_{(pH\ 7.2)}$, FeS-C$_{(pH\ 8.0)}$ & FeS-D$_{(pH\ 8.2)}$):

Samples FeS-A through D were synthesized and processed according to the protocol outlined in **Table 2**. Upon mixing, the precipitated solid phase and supernatant solution were sealed in 50 ml plastic centrifuge tubes under anoxic conditions in preparation for rinsing of the solid phase. The precipitates were dried in the anaerobic glove box within less than two hours from the time of mixing.

Table 1. Sample identification and synthesis conditions

Manuscript Sample ID	**Reagent Volumes (mL)**			**pH**	**Aged (Y/N)**	**Dried (Y/N)**
	Mohr's Salt	Sulfide	Buffer (pH)			
FeS-A	10	10	10 (4)	5.3	N	Y
FeS-B	10	10	5 (4)	7.2	N	Y
FeS-C	10	10	--	8.0	N	Y
FeS-D	10	10	2.5 (12)	8.2	N	Y
FeS-E	15	17	10 (4)	5.5	N	N
FeS-F	500	525	--	9.2	Y	Y
	Iron Wool	Sulfide	Acetic Acid/Acetate			
FeS-Bulk	5 grams	100 mL	500 mL	1.7 – 4.5	N	Y

Ferrous ammonium sulfate hexahydrate (Mohr's Salt) was used as the source of Fe^{+2} for FeS-A through -F. Samples FeS-A through -E were synthesized using 0.3 M stock solutions. FeS-F was synthesized using 0.2 M stock solutions and was aged for one week at 70 °C as part of a large batch of sample. FeS-Bulk was synthesized according to the prep of Lennie *et al*. (*20*).

Table 2. Protocol for sample preparation (FeS-A, B, C, D and F

Step	Action
Synthesis	Mix reagents and precipitate FeS_{fresh} in 50 ml centrifuge tubes (followed by aging for one week at 70 °C in the case of FeS-F)
	Sonicate (1 min) and vortex (20 sec)
	Centrifuge 3 minutes at 5,000 RPM
	Decant supernatant #1 and add ~45 ml 1 mM sulfide solution
Rinse Cycle 1	Centrifuge 5 minutes at 5,000 RPM
	Decant supernatant and add ~45 ml 1 mM sulfide solution
	Sonicate (1 min) and vortex (20 sec)
Rinse Cycle 2	*Repeat Cycle 1*
Rinse Cycle 3	Centrifuge 5 minutes at 5,000 RPM
	Decant supernatant (including colloidal suspension*)
Extraction	Filter solid phase product
	Dry product under N_2 stream
	Lightly grind using agate mortar and pestle
Loading	Powders loaded into 1 mm polyimide capillaries and capped with glass wool and an amorphous silicone vacuum grease
Storage	Loaded capillaries were sealed in individual glass culture tubes pending transport to APS

Gray indicates actions were carried out in glove box under completely anoxic conditions. White indicates that action was carried out on sample sealed in centrifuge tube and capped with $H_2 – N_2$ mix. *Supernatant included a stable suspension of colloidal FeS particles and was preserved for TEM imaging.

Fresh Precipitate - Wet (FeS-E$_{(pH\ 5.5)}$):

Sample FeS-E was synthesized at the APS and analyzed within about 8 hours after the time of mixing the reagents. The protocol was similar to that used for the dry precipitates but with several differences outlined in **Table 3**. The reagents were mixed in a fume hood under flowing N_2 because a glove box was not available for use. The sample was centrifuged for one cycle (5 min at 3,000 RPM) in a 50 ml centrifuge tube. The resulting supernatant was then removed leaving the dense, wet FeS slurry that was packed into a 3 mm polyimide capillary and capped on both ends with wax under a stream of N_2. The loaded capillary was then centrifuged a second time to squeeze out more of the supernatant solution leaving a denser sample for analysis. This sample was analyzed to evaluate the effects of water on the structure, specifically to assess the degree of lattice relaxation relative to a dry sample precipitated under similar pH conditions (FeS-A).

Aged Precipitate (FeS-F$_{(pH9.2)}$):

FeS-F was synthesized following generally the same protocol as samples A – D but in addition was aged for one week at elevated temperature in a water bath as part of a large sample batch. FeS-F was formed by the direct injection of 500 ml of 0.2 M Mohr's Salt into 525 ml 0.2 M sulfide solution. The resultant product and supernatant were sealed under anoxic conditions in a 1 L glass vessel and immersed in a pre-heated 70 °C water bath for one week. The sample was agitated periodically by gently shaking. At the end of one week of aging, a portion of the sample was then separated under anoxic conditions in preparation for processing and characterization as described below.

Table 3. Protocol for sample preparation (FeS-E)

Step	**Action**
Synthesis	Mix reagents and precipitate FeS in 50 ml centrifuge tubes
	Centrifuge 5 minutes at 3,000 RPM
	Decant supernatant and add ~45 ml 1 mM sulfide solution
Rinse Cycle 1	Centrifuge 5 minutes at 3,000 RPM
	Decant supernatant
Loading	Wet slurry loaded into 3 mm polyimide capillaries and capped with wax
Centrifuge	Loaded capillaries were placed in 15 ml centrifuge tubes and centrifuged for 5 minutes at 3,000 RPM

Grey indicates actions were carried out under a stream of N_2.

Crystalline FeS (FeS-Bulk):

FeS-Bulk was synthesized according to the protocol described by Lennie *et al.* (*20*). In brief, finely-divided iron wool was rinsed with laboratory grade acetone prior to immersion in a beaker containing 500 ml of a 0.5 M acetic acid/acetate buffer (pH = 1.7) solution. After approximately 30 minutes, sufficient H_2 evolved from the reaction between the steel wool and acetic acid for the wool to be brought to the surface by trapped gas. Sulfide was subsequently added slowly to the solution and FeS spalled off of the surface of the iron and settled to the bottom of the beaker. The pH of the solution, initially at 1.7, increased to 4.5 when 100 ml of sulfide solution was added. The solution was allowed to sit for approximately 2 hours before the supernatant was decanted. A stirring bar magnet was used to recover any remaining fragments of metallic iron from the settled FeS precipitate. The recovered solid phase FeS was then washed using the centrifuge-rinsing protocol described below and subsequently filtered and dried. Characterization of the solid phase FeS by XRD revealed the presence of a minor percentage of greigite formed as a secondary phase. Because the synthesis was carried out under completely anoxic conditions we speculate that greigite (Fe_3S_4) formed in this instance from oxidized (ferric) iron present as impurities in the iron wool.

Sample Preparation:

Centrifuge & Rinsing:

The solid phase FeS precipitates (excluding FeS-E) were each rinsed three times using a protocol developed to minimize oxidation of the metal sulfide and yet to remove most of the electrolytes associated with the starting reagents. This rinsing protocol, summarized in **Table 2**, is a modified and expanded version of a protocol first described by Herbert *et al.* (*16*). In brief, during three cycles the FeS slurry was centrifuged for 5 minutes at 5,000 RPM after which the loaded tubes were returned to the glove box where most of the supernatant was removed from each and replaced by approximately 45 ml of 1 mM sulfide rinse solution. The sulfide rinse solution also served as a scavenger of oxygen preventing the surface oxidation of the FeS precipitate. The solid phase was then re-suspended in each fresh rinse solution using first a vortexer for 20 seconds followed by agitation in a sonicator bath for 1 minute. This process was repeated and following the third and final centrifuge-rinse cycle the solid phase FeS product was extracted under anoxic conditions.

Drying:

The resulting wet FeS slurry was filtered over a membrane filter with 0.2 μm diameter pores. It was observed that the liquid fraction was removed very slowly because the pores of the membrane filter were quickly clogged by the solid phase precipitate. The solid phase collected on the filter was dried at room temperature in the glove box under a stream of N_2.

Loading of capillaries:

Both dry and wet samples were pre-loaded into 1 mm or 3 mm O.D. polyimide (Kapton®) capillaries under completely anoxic atmosphere and capped at both ends to inhibit gas exchange and oxidation. The loaded capillaries were then sealed under anoxic conditions (excluding FeS-E) in glass culture tubes with septum caps for transport to the APS. As described earlier, the FeS-E sample was prepared on-site at the APS.

Sample Characterization:

Over 30 synthetic FeS samples were characterized at the APS. However, only data for seven representative samples are discussed in detail in this paper. Sample identification and the conditions under which they were analyzed are described in **Tables 1 - 3**. Data for the freshly precipitated samples that were analyzed as dry powders (FeS-A, B, C, and D) and also the wet slurry (FeS-E) were collected at BESSRC-CAT 11-IDC. The aged precipitate (FeS-F) and highly crystalline sample (FeS-Bulk) were analyzed at XOR 1-ID.

High energy powder X-ray diffraction (XRD) at the Advanced Photon Source

High energy powder XRD data was collected at 11-IDC (115 keV, $\lambda = 0.1076$ Å (*21*)) and at 1-ID (79.9 keV, $\lambda = 0.15513$ Å and 99.9 keV, $\lambda = 0.1240$ Å (*22*)). A CeO_2 standard (NIST diffraction intensity standard set: 674a) was used to calibrate the sample-to-detector distance and the tilt of the detector relative to the incident beam path. The energy calibration was initially achieved using the gold absorption edge as reference and, if increased to higher energies (i.e., 99.9 or 115 keV), was recalibrated by refinement of the wavelength and fixing of the sample-to-detector distance. The radiation scattered by the calibrant and samples was collected on a MAR-345 image plate detector system and processed using the program Fit-2D (*23, 24*). A polarization correction was applied during integration of the data. Data was also collected on both blank (empty) polyimide capillaries (1 mm & 3 mm) and on those loaded with de-ionized water for background correction during PDF analysis. The sample capillary was rotated during data collection.

Pair Distribution Function (PDF) analysis:

The total scattering structure function *S(Q)* and PDF *G(r)* were obtained using PDFgetX2 (*25*) where standard corrections were applied as well as those unique to image-plate geometry (*26*). The structure of crystalline mackinawite consists of tetrahedral layers of Fe and S atoms (**Figure 1**). The Fourier transform of the normalized and scaled *S(Q)*, or *Q*[*S(Q)-1*] (**Figures 2a - f**), resulted in the PDF, or G(r), which corresponds to real-space inter-atomic distances. The model for crystalline mackinawite was fitted to the experimental PDF and the structural parameters of the model were refined and plotted using the programs PDFfit and Kuplot (*27*), respectively (**Figures 3a - f**). The initial atomic coordinates, cell parameters, isotropic displacement parameters (U), and spacegroup (P4/nmm) were those of Lennie *et al.* (*20*). Two additional parameters δ and σ_Q were incorporated in each refinement to model sharpening of PDF near neighbor peaks due to correlated motion between atom pairs and the exponential decay of the PDF, respectively. If within the resolution of the instrument, the exponential decay of the PDF can be attributed to a limited range of structural coherence in nanocrystalline materials (i.e. primary crystallite size). In the case of highly crystalline samples, the decay of the PDF represents the resolution of the instrument (*14*).

Transmission Electron Microscopy (TEM):

Selected FeS samples were mounted directly from the stable suspensions captured during the centrifuge-rinse processing outlined in **Table 2**. Prior to mounting on grids,

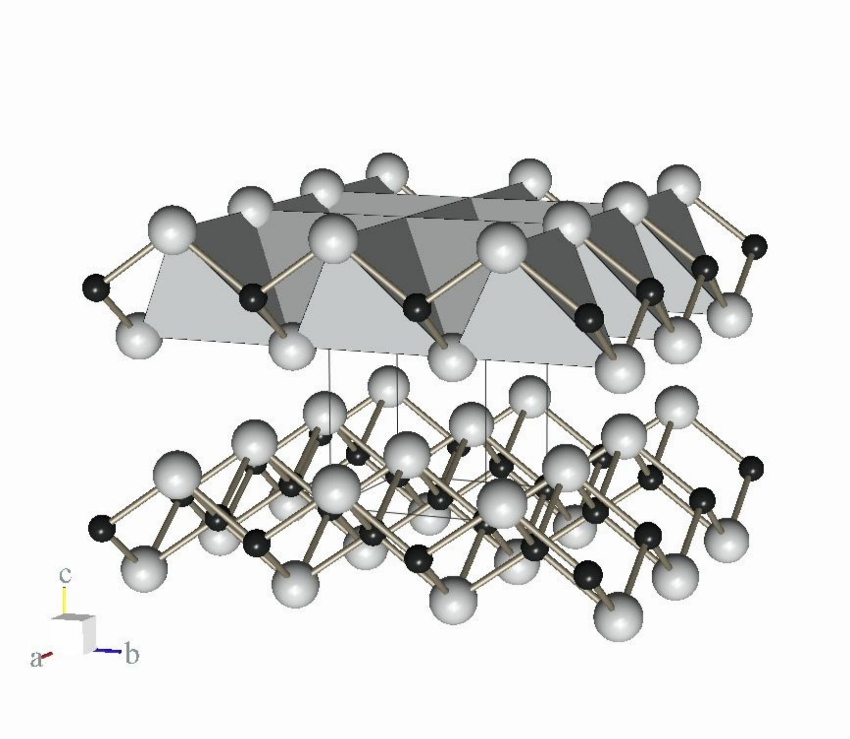

Figure 1. The layered structure of mackinawite. Small spheres represent Fe atoms; large spheres represent S atoms; a unit cell is outlined. Fe is tetrahedrally coordinated by S atoms and in square planar coordination with Fe.

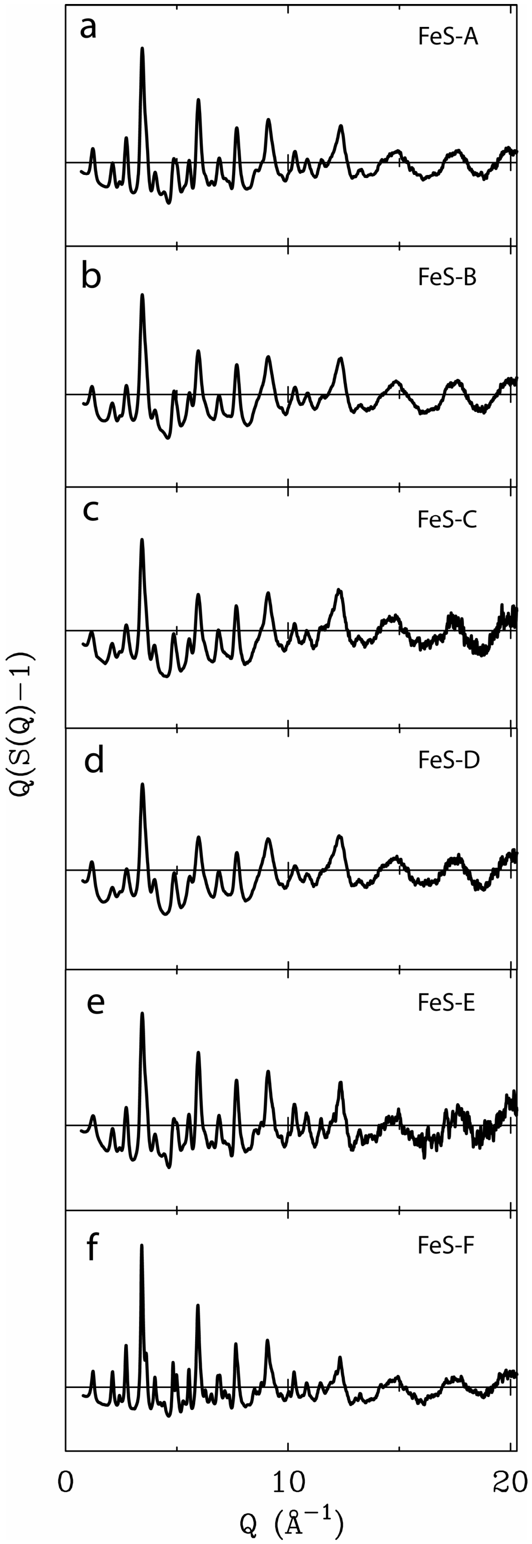

Figures 2a – 2f. The normalized scattering function $Q[S(Q)-1]$ vs. Q (Å^{-1}) for each of the six FeS samples.

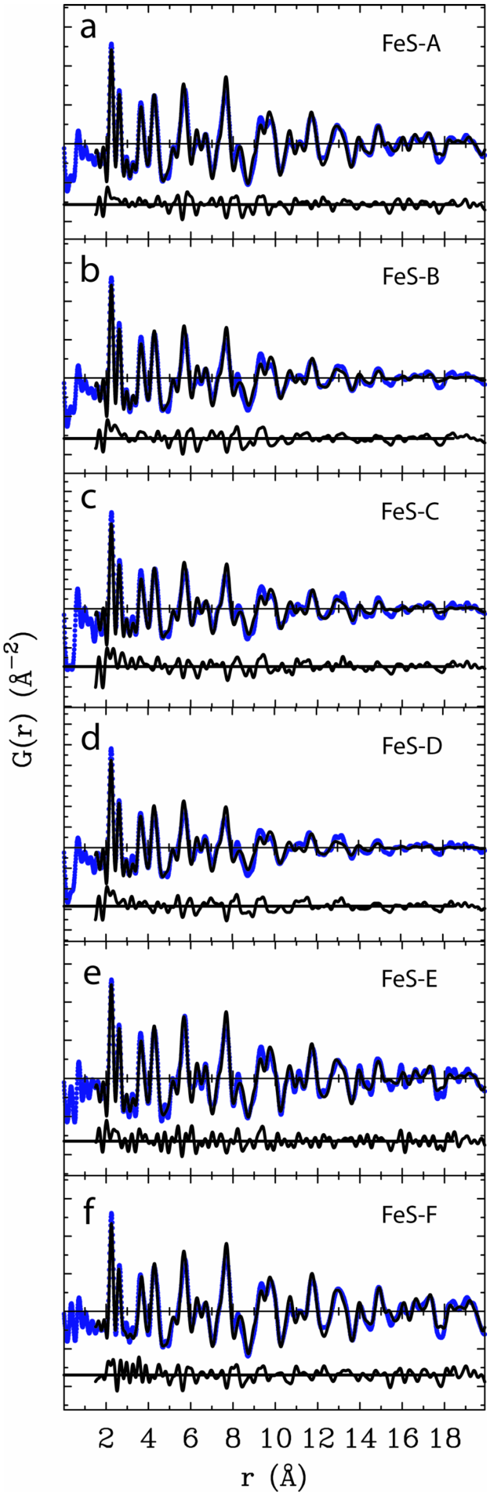

Figures 3a – 3f. *G(r)* or the PDF versus distance is plotted with the experimental data (blue circles) fitted by the refined model PDF (solid black) shown. A difference plot is included beneath each data set as an indication of fit.

the pH of the suspension was adjusted down to ~4 using HCl in order to disaggregate the FeS clusters in solution (unpublished dynamic light scattering results). FeS particles in solution were transferred under completely anoxic conditions onto 300 mesh, 3 mm, and carbon-coated copper grids with Formvar®. The mounted grids were dried under a stream of N_2 and then stored temporarily in glass vials and capped under anoxic conditions for transport to the TEM. The grids were each exposed to atmospheric oxygen for less than one minute on average while being transferred from the N_2-capped vials to a beryllium TEM sample holder before being placed under high vacuum in the microscope. Imaging was performed using a Philips CM12 scanning TEM with a high brightness (LaB_6) electron gun.

Results

Structural analysis using the PDF method involves a comparison between PDFs generated from the experimental scattering data and a model PDF. In this study the model PDF was based on the structure of crystalline mackinawite (*20*) and was refined in real-space and fit to the experimental PDFs for each of the seven representative samples. The fits of the single-phase mackinawite model are included as **Figures 3a – f**. The PDF has peaks at characteristic distances separating pairs of atoms and thus, $G(r)$ is a measure of the probability of finding an atom at a distance r from a reference atom and so describes the atomic arrangement (structure) of materials (*10*). Unit cell parameters, isotropic-displacement parameters, atom positions (S z-position), resolution dampening (σ_Q), a peak sharpening factor (δ), and scale factor were all refined simultaneously using PDFFit (**Tables 4a & 5a**). A "goodness of fit" indicator (R_w) is also reported for each refinement and information regarding the acceptable ranges for R_w and accuracy of the technique have been discussed elsewhere (*28-30*).

Table 4a. Refinement Results

Parameter	FeS-A (1)	FeS-B (1)	FeS-C (1)	FeS-D (1)	FeS-E (1)	FeS-F (2)	Rietveld Parameters**	CeO_2 (1)	CeO_2 (2)
a (Å) =	3.685(6)	3.687(2)	3.696(1)	3.694(6)	3.685(4)	3.695(1)	3.6735(4)	5.403(8)	5.419(9)
c (Å) =	5.037(4)	5.082(9)	5.083(3)	5.089(3)	5.068(2)	5.057(6)	5.0328(7)	--	--
S z-position	0.2550	0.2533(6)	0.2528(5)	0.2523(6)	0.2537(6)	0.2553(5)	0.2602(3)	--	--
R_w (%)	24.9	30.4	34.1	33.6	28.0	27.2	--	15.4	17.5
σ_Q (Å^{-1})	0.094(8)	0.133(8)	0.123(6)	0.146(1)	0.098(2)	0.077(8)	--	0.059(2)	0.032(8)
δ	0.090(3)	0.097(4)	0.100(5)	0.100(8)	0.090(7)	0.082(8)	--	0.093(7)	0.053(6)
*U_{Fe} (Å^2)	0.009(7)	0.009(9)	0.010(2)	0.010(5)	0.009(6)	0.009(9)	--	0.005(6)	0.004(5)
*U_S (Å^2)	0.009(7)	0.010(1)	0.009(6)	0.010(2)	0.009(9)	0.009(7)	--	0.023(4)	0.023(7)
pH	5.3	7.2	8	8.2	5.5	9.2	--	--	--
Aging	None	None	None	None	None	1 week at 70 °C	--	--	--

*U = isotropic-displacement parameter. **Cell parameters reported by Lennie *et al*. (*20*) for a Rietveld refinement of crystalline mackinawite. (1) Indicates data collected at 11-IDC (Energy = 115 keV). (2) Indicates data collected at 1-ID (Energy = 99.9 keV).

Table 4b. Refined Bond Lengths and Angles

Bond Lengths (Å)		**FeS-A**	**FeS-B**	**FeS-C**	**FeS-D**	**FeS-E**	**FeS-F**	**Rietveld Parameters***
Fe – S		2.246(3)	2.248(7)	2.250(8)	2.250(3)	2.246(9)	2.254(1)	2.2558(9)
Fe – Fe		2.606(1)	2.607(3)	2.613(4)	2.612(5)	2.605(9)	2.612(8)	2.5976(3)
Bond Angle (°)	**Coord.No.**							
S – Fe – S	2	109.09(5)°	109.14(6)°	109.02(6)°	109.01(7)°	109.11(7)°	109.16(6)°	109.0251°
	2	110.24(6)°	110.14(8)°	110.38(8)°	110.39(9)°	110.19(8)°	110.10(6)°	109.6947°
Fe – Fe – Fe	4	90°	90°	90°	90°	90°	90°	90°
Fe – S – Fe	2	70.91(1)°	70.86(1)°	70.98(1)°	70.99(2)°	70.89(2)°	70.84(1)°	70.3053°
	2	109.09(5)°	109.14(6)°	109.02(6)°	109.01(7)°	109.11(7)°	109.16(6)°	109.0251°

*Bond lengths and angles reported by Lennie *et al.* (*20*) for a Rietveld refinement of crystalline mackinawite.

Table 5a. Refinement results (FeS-Bulk)

Parameter	FeS-Bulk $^{(3)}$	Rietveld Parameters**	CeO_2 $^{(3)}$
a (Å) =	3.676(6)	3.6735(4)	5.4070(3)
c (Å) =	5.028(4)	5.0328(7)	--
S z-position	0.2559(1)	0.2602(3)	--
R_w (%)	29.0	--	28.9
σ_Q (Å^{-1})	0.066(1)	--	0.033(3)
δ	0.082(9)	--	0.034(3)
*U_{Fe} (Å^2)	0.011(8)	--	*U_{Ce} = 0.005(9)
*U_S (Å^2)	0.012(9)	--	*U_O = 0.008(8)
pH	1.5	--	--
Aging	2 hours at 22 °C	--	--

*U = isotropic-displacement parameter. **Cell parameters reported by Lennie *et al.* (*20*) for a Rietveld refinement of crystalline mackinawite. $^{(3)}$ Indicates data collected at 1-ID (Energy = 80 keV).

Table 5b. Refined bond lengths and angles (FeS-Bulk)

Bond Lengths (Å)		**FeS-Bulk**	**Rietveld Parameters***
Fe – S		2.244(5)	2.2558(9)
Fe – Fe		2.599(8)	2.5976(3)
Bond Angle	**Coord. No.**		
S – Fe – S	2	109.20(2)°	109.0251°
	2	110.02(2) °	109.6947°
Fe – Fe – Fe	4	90°	90°
Fe – S – Fe	2	70.8(3)°	70.3053°
	2	109.20(2)°	109.0251°

*Bond lengths and angles reported by Lennie *et al.* (*20*) for a Rietveld refinement of crystalline mackinawite.

Unit Cell Parameters, Bond Lengths and Angles:

The cell parameters derived from PDF refinement of all of the FeS samples analyzed (**Table 4a**) are in good agreement with those reported from Rietveld refinement of crystalline mackinawite (*20*) and with the highly crystalline sample (FeS-Bulk) analyzed here (**Table 5a**). Bond lengths and angles calculated using PDFFit subsequent to each refinement are listed in **Tables 4b & 5b**. The analysis of the structure of FeS_{fresh} and FeS_{aged} are nearly identical with previous reports on the structure of crystalline mackinawite (*20, 31*). A crystalline CeO_2 standard was also analyzed during each of the three data collection events and the results of the refinements are included for reference (**Tables 4a & 5a**).

Structure Relaxation:

The *c*-parameter corresponding to the atomic spacing between basal planes in the layered mackinawite structure of FeS_{fresh} and FeS_{aged} shows only minor relaxation (less then ~1%) compared to bulk FeS. Further, the refined *a*-parameter corresponding to Fe in square planar coordination is also very close to that of the bulk sample. As will be discussed, these refined values are not consistent with those reported in a recent investigation (*3*) which concluded that a portion of the initial precipitate forms with a highly relaxed structure. The structure of the initial precipitate also did not change when dispersed in an aqueous media. The present study includes two samples (FeS-A & FeS-E) that were initially precipitated under similar pH conditions but differed in that sample FeS-E was analyzed as a dense wet slurry while FeS-A was in the form of a thoroughly dried sample. The refined model PDFs were fitted to the experimental PDFs (**Tables 4a & 4b**) and no significant differences in lattice parameters were observed. This indicates that drying of the material does not result in any significant structural changes.

PDF Attenuation & Particle Size:

The primary method of synthesis employed in this study involves a sudden generation of high supersaturation levels and results in the rapid nucleation of very small particles at the time of mixing (*32*). As mentioned above, the PDF method has been demonstrated to be a useful tool in determining the primary crystallite size of

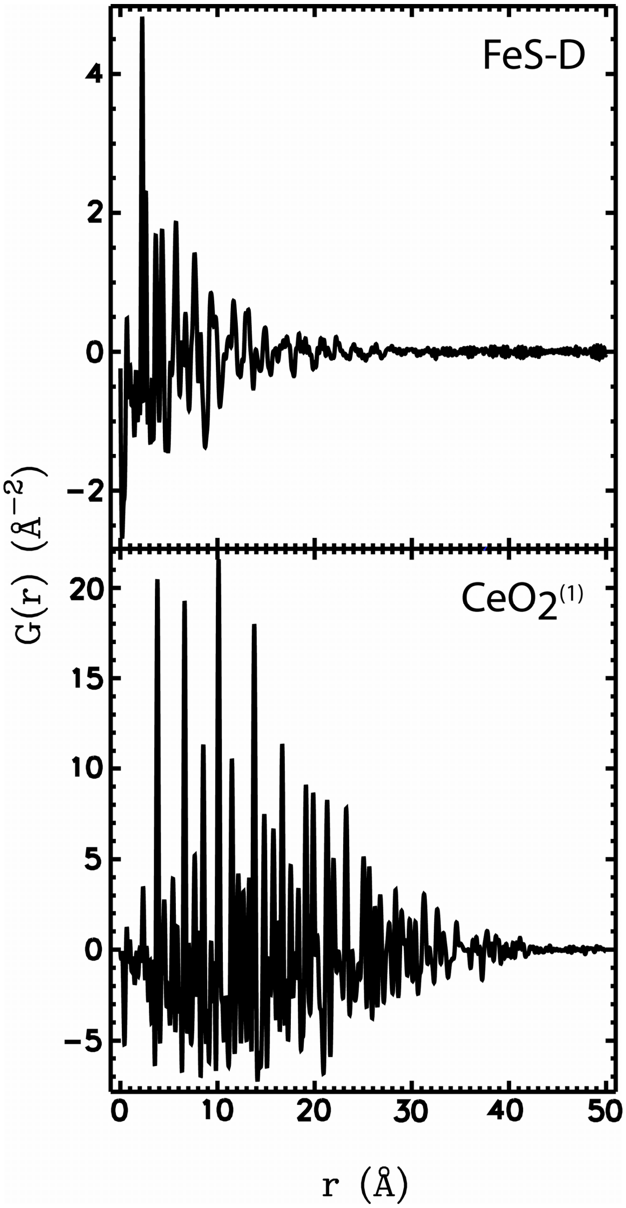

Figure 4a. *G(r)* plotted out to 50 Å or 5 nm to illustrate the degree of attenuation due to the range of structural coherence, i.e. crystallite size (~2 nm), of a sample of freshly precipitated FeS at pH 8.2. The PDF for $\mathrm{CeO_2}^{(1)}$ is included to demonstrate the attenuation of a crystalline sample due to instrument resolution (BESSRC 11-IDC, 115 keV). Note the increased intensity and range of the correlations in the crystalline material.

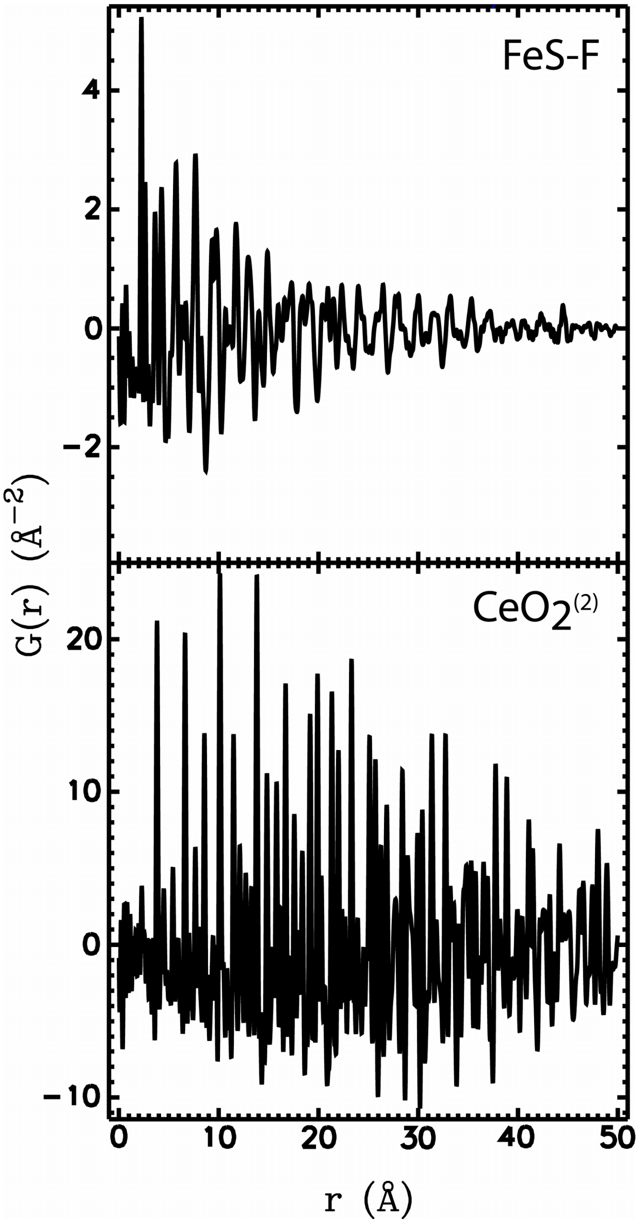

Figure 4b. *G(r)* plotted out to 50 Å or 5 nm to illustrate the degree attenuation due to the range of structural coherence, i.e. crystallite size (~4.5 nm) of a sample hydrothermally aged for one week. The PDF for $CeO_2^{(2)}$ is included to demonstrate the attenuation of a crystalline sample due to instrument resolution (1-IDC, 99.9 keV).

nanocrystalline materials through an evaluation of the attenuation of the PDF resulting from a limited range of structural coherence. PDFs for the freshly precipitated samples analyzed as dry powders (FeS-A, B, C & D) and in one case as a wet slurry (FeS-E) all show a significant degree of attenuation by a distance of only ~2 nm (**Figure 3a**). The radial distance plotted along the abscissa was extended to emphasize the strong degree of attenuation at relatively short distance in FeS-D and FeS-F compared to a highly crystalline CeO_2 standard (**Figures 4a & 4b)**. Here, the correlations of FeS-D beyond ~2 nm terminate, reducing the signal to statistical noise and this pattern is repeated in the other fresh precipitates. Our evidence of the primary crystallite size for FeS_{fresh} from PDF analysis shows only partial agreement with prior research in which the Scherrer equation was applied to low energy XRD data and nano-scale particle sizes were calculated (*3*).

It is important to note here that this attenuation in structural coherence is not due to the attenuation in the PDF that occurs at an even greater *r*-distance and is inherent to the instrument, known as the resolution dampening factor (σ_Q) (*27*) or instrument envelope. This envelope was evaluated independently at each beamline using highly crystalline CeO_2 with reported particle sizes >1 μm from which a refined value of σ_Q ($Å^{-1}$) was obtained. In all cases the refined values for CeO_2 were significantly less (i.e. exhibiting higher intensity correlations extending to a much higher radial distance) than those for both the fresh and aged precipitates examined (**Tables 4a & 5a**). This high degree of attenuation in the PDFs for the fresh precipitates is also apparent when compared with that of highly crystalline FeS (**Figure 4c**). In this plot the PDF for FeS-Bulk has a comparable attenuation to that of CeO_2 collected on the same instrument. Therefore, like CeO_2, this highly crystalline sample is also representative of the instrument envelope. The range of structural coherence is the most important feature and the intensity differences evident between mackinawite and CeO_2 in **Figure 4c** are explained by a higher number of atom pairs at each given distance and also their corresponding scattering power. In this study, PDFs with a limited range in structural coherence have σ_Q values ranging from 0.08 to 0.15 (FeS_{fresh} & FeS_{aged}) compared to that of crystalline CeO_2 which is 0.03 at 1-ID and 0.06 at 11-IDC. Thus, from the apparent limited range of structural coherence the average primary crystallite size of the FeS_{fresh} crystallites is estimated to be on the order of ~2 nm in diameter and may be even less in

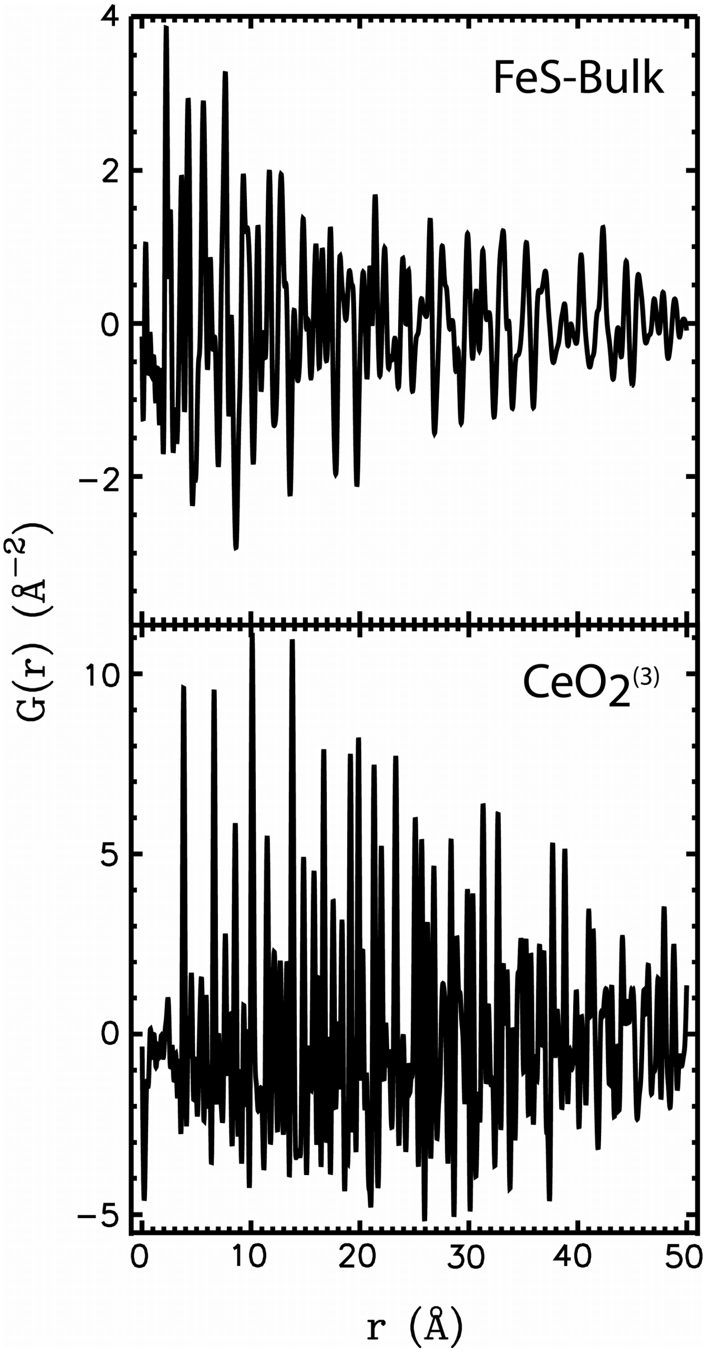

Figure 4c. *G(r)* plotted out to 50 Å or 5 nm to illustrate how the bulk FeS sample (FeS-Bulk) has the same attenuation as the crystalline CeO_2 standard. The PDF for $CeO_2^{(3)}$ is included to demonstrate the attenuation of a crystalline sample due to instrument resolution (1-IDC, 79.9 keV). Note again the increased intensity and range of the correlations in the crystalline material.

certain dimensions. This finding was corroborated by direct imaging of the particles using TEM. A representative image of a freshly precipitated sample is presented (**Figure 5**).

Growth:

Prior research (*1, 33*) indicates that the initial FeS precipitate will develop improved long-range atomic arrangement and eventually form what is considered bulk mackinawite. It is reasonable then to hypothesize that the nanocrystalline fresh precipitates reported here will become larger upon aging through crystal growth by mechanism such as Ostwald ripening (*34*) or oriented attachment (*35*). An increase in the range of structural coherence in the PDF would be predicted due to growth by either mechanism. This feature was observed in the PDF for sample FeS-F (**Figure 4b**), which, upon aging for one week at 70 °C, showed correlations that clearly can be fitted by the mackinawite model to a range of ~4.5 nm. This finding was also consistent with TEM analysis and representative images of sample FeS-F are presented (**Figure 6 & 7**). The FeS crystallites appear to be relatively monodisperse in these two images appearing both as individual particles and as aggregates. It is difficult to say with any confidence by which mechanism(s) the particles grow.

pH Effects:

The data obtained from the pH-buffered precipitates do not show significant structural changes between pH ranging from ~5 to ~8. The sample formed under the lowest pH conditions (FeS-A) had a slightly better fit as expressed in the residual difference (R_w) between the experimental PDFs and fitted model (**Table 4a**) compared to those samples formed at higher pH values (FeS-B, C and D). The consistency in the derived unit cell parameters and decrease in σ_Q (**Table 4a**) between these samples may indicate that this improvement is due primarily to a slight increase in the crystallite size of the initial precipitate under decreasing pH conditions (**Figure 3a - d**). This may also indicate a change in electronic structure with increasing particle size as seen in the optical properties of nano-sized MoS_2 in which a change from molecule-like to solid-like band spectra was demonstrated (*36*).

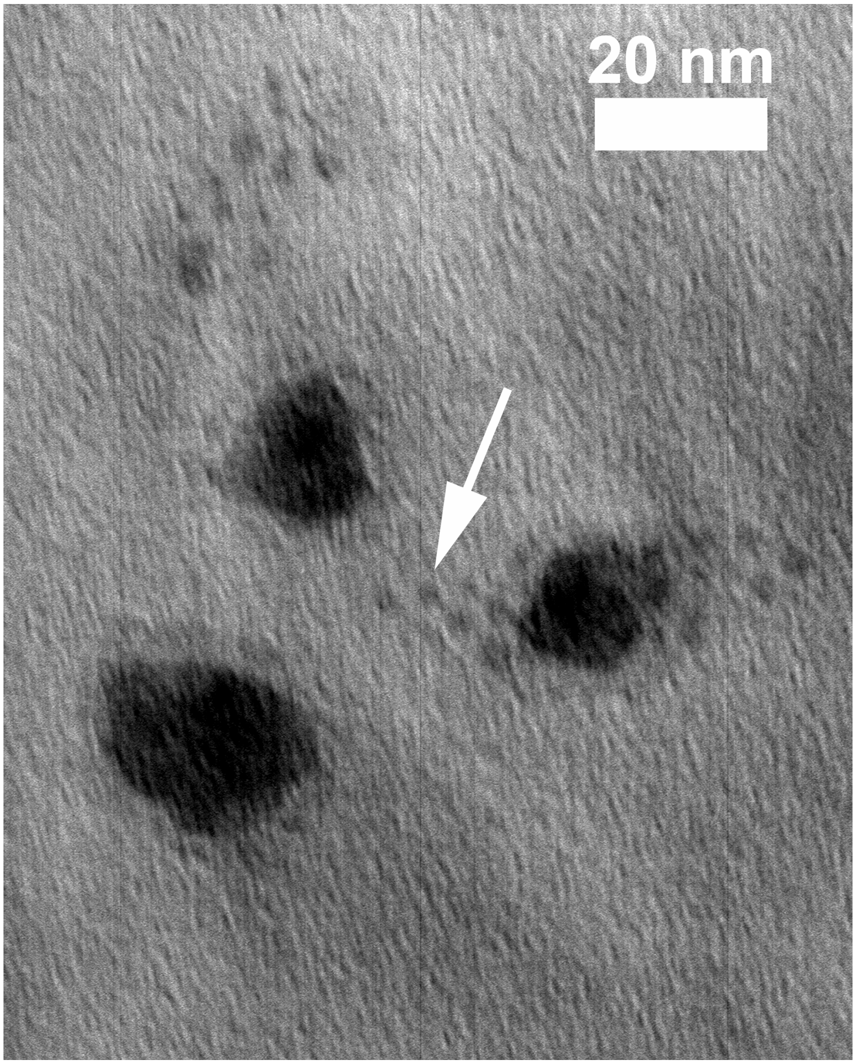

Figure 5. Transmission electron micrograph (TEM) of freshly precipitated individual FeS crystallites (arrow) approximately 2 nm in diameter and larger aggregates (260k magnification). Scale bar indicates 20 nm.

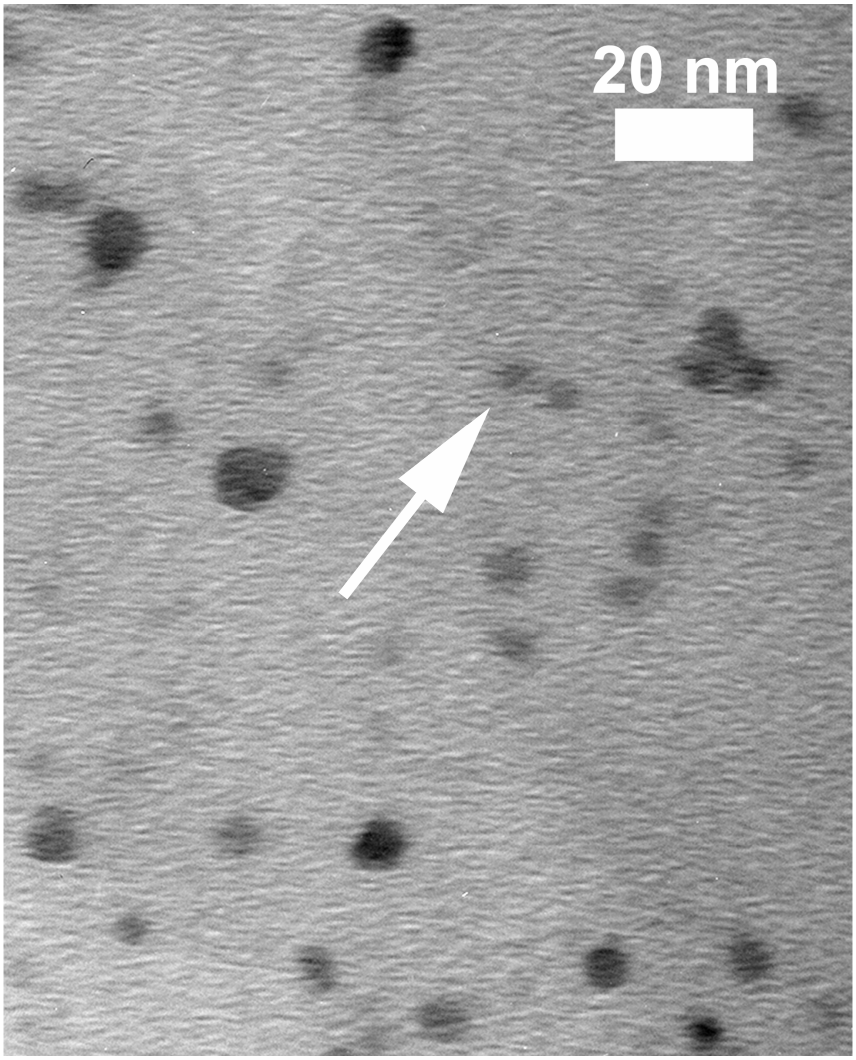

Figure 6. TEM image of FeS crystallites approximately 4 – 5 nm in diameter subsequent to aging (7 days at 70 °C). Slightly larger and darker particles may be aggregates of multiple smaller crystallites (260k magnification). Scale bar indicates 20 nm.

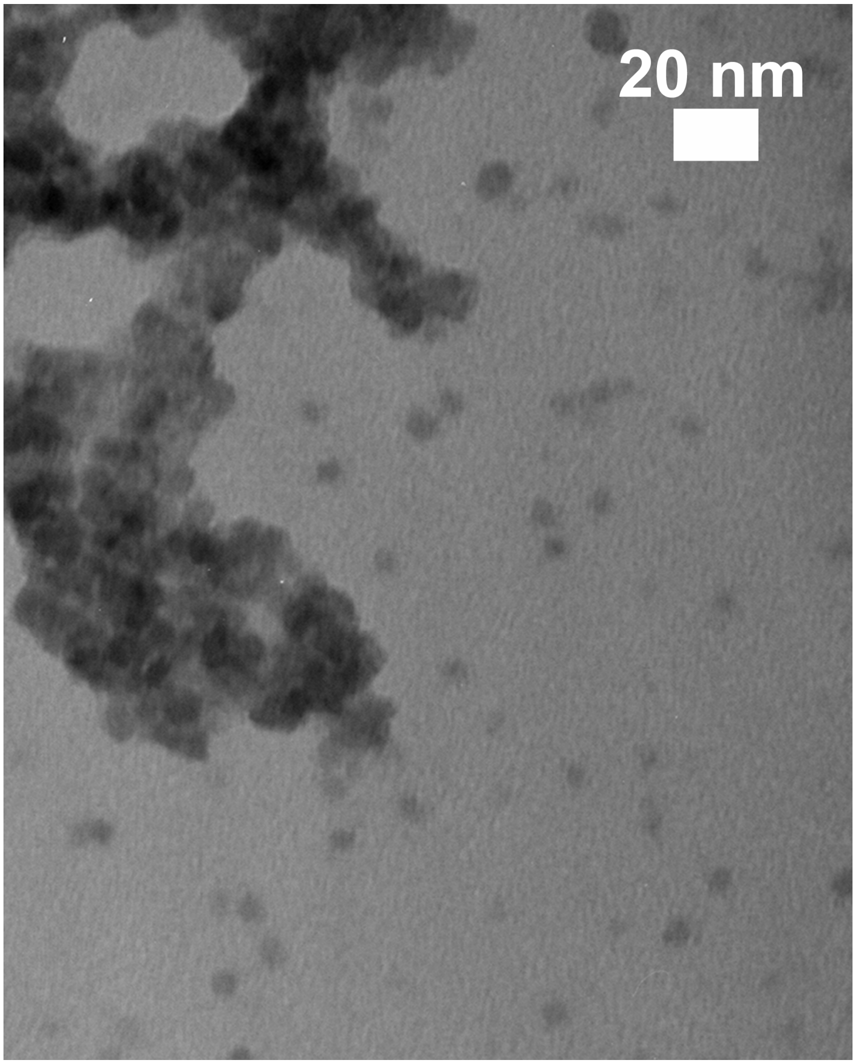

Figure 7. TEM image of FeS crystallites subsequent to aging (7 days at 70 °C). Individual particles appear relatively monodisperse and are also apparent in larger aggregates (160k magnification). Scale bar indicates 20 nm.

Aggregation:

The individual FeS particles have a strong tendency to aggregate. This aggregation into larger ensembles may be one of the reasons why there has been so little consensus in the literature on the primary crystallite size and morphology of the initial FeS precipitate. Electron microscopic images presented in several studies showed poorly-defined agglomerates of freshly precipitated FeS particles formed through inorganic synthesis (*3, 5, 37*). A study of biogenic iron sulfides formed in a culture of sulfate reducing bacteria reported FeS precipitates occurring as fine-grained and platy particles on the order of 100 to 300 nm in diameter (*16*). The particle sizes estimated in that study do not seem consistent with the concurrent XRD analysis in which the authors reported that the material was X-ray amorphous showing only a broad peak with a corresponding inter-planar distance of ~5 Å. Although the particle sizes reported by that study are orders of magnitude larger than the present study it is possible that the aggregation behavior of particles obscured what may also have been fundamentally a nanocrystalline material. Assembly of particles into aggregates may occur with assembly by randomly oriented stacking and may indicate localized oppositely charged regions are present on the edges versus faces of the particles. This behavior has been observed in flocculated clays and described as having edge-to-face type configurations (*38*). The aggregation may also be due in part to the effects of cations while still in solution which has been shown previously to be enhanced by increasing ionic strength (*39*).

Discussion

The lack of consensus between prior studies of the structure and/or crystallite size of FeS_{fresh} is primarily attributable to two factors: the extreme small size of the crystallites and their tendency to aggregate. The usefulness of more traditional techniques like the Rietveld (*40*) method in refining the long-range atomic order of FeS_{fresh} have been limited by broadening of the Bragg reflections resulting primarily from submicron particle sizes (*41, 42*). Further, the diffuse scattering characteristic of short-range order is usually folded into the background correction in this methodology. However, the PDF method is well-suited in that it utilizes the total scattering of the sample, i.e., both the Bragg and diffuse components, and does not assume that the structure exhibits long-range periodicity (*43*). A strong tendency for FeS to aggregate in solution (unpublished dynamic light scattering results) and upon processing (such as during filtering and drying) has led to a wide range of particle sizes reported in the literature. The particle sizes in a variety of studies ranged from 2 to 400 nm were reported from electron microscopic imaging (SEM & TEM), calculated from gas adsorption measurements (BET), and calculated from small angle X-ray powder diffraction data (*3, 37, 44-48*).

The short- to medium-range atomic structure determined from PDF for FeS_{fresh} and FeS_{aged} are nearly identical with that of a single-phase and highly crystalline mackinawite. The short-range structure reported here is consistent with that presented in a prior investigation using X-ray absorption spectroscopy (*31*) and our results go further by also characterizing the medium-range structure as well as the crystallite size. Our study differs, however, from previous theories that have described the initial precipitate as either a mixture of mackinawite and greigite (Fe_3S_4) (*15*) or as a mixture of two end-member mackinawite phases (MkA and MkB) each with distinct long-range ordering (*3, 15, 49*). The former hypothesis, proposed nearly 40 years ago, was based on observations of XRD data collected using low-energy Cu radiation. The presence of greigite as a secondary phase was difficult to discern with any certainty since the scattering from the initial FeS precipitate was weak overall with broadened peaks. In the XRD pattern presented (*49*) the peak positions suggested only the presence of poorly crystalline material with a mackinawite-like structure. In the present study, greigite was not observed in any of the nanocrystalline FeS samples (FeS_{fresh} and FeS_{aged}) formed by the commonly used rapid-mixing method. Although greigite was detected in FeS-Bulk as a secondary phase we believe this to be the result of oxidized iron impurities in the iron wool used in the synthesis. To illustrate how the PDFs for other iron sulfide phases would differ from that of mackinawite a series of patterns have been calculated using PDFFit (**Figure 8**). It is clear that the inter-atomic distances for mackinawite are distinct from those of other iron sulfide phases (e.g., greigite, smythite, pyrrhotite and troilite) and therefore these would not provide an adequate fit to the experimental data presented here.

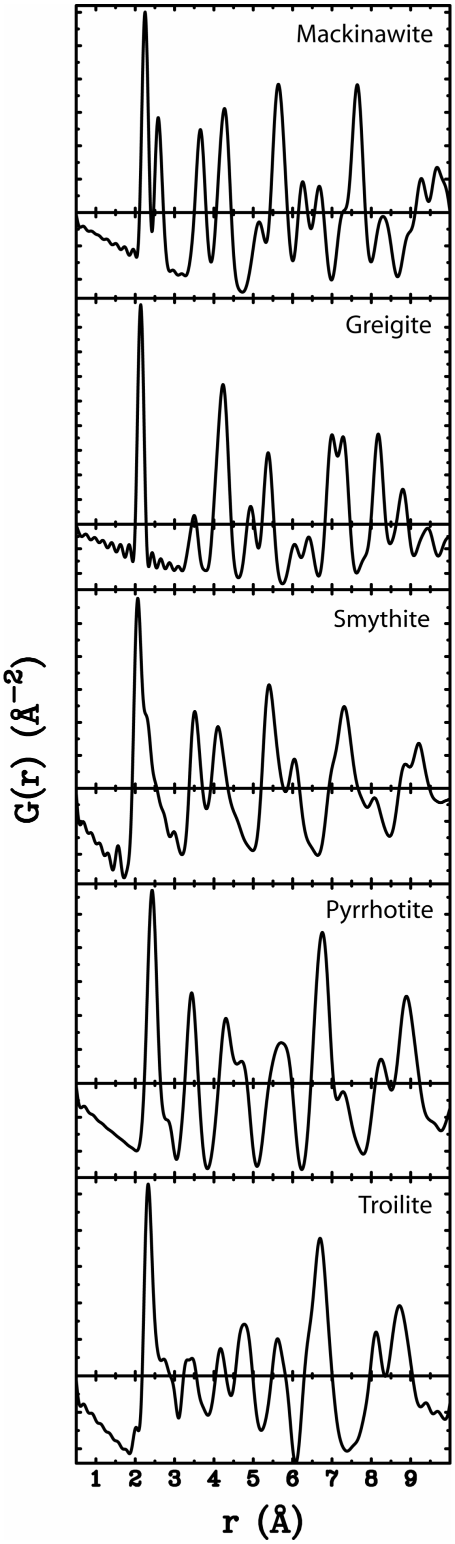

Figure 8. Calculated *G(r)* for several iron sulfide phases including mackinawite (FeS), greigite (Fe_3S_4), smythite (Fe_3S_4), pyrrhotite (~Fe_7S_8) and troilite (FeS). These calculations are based on the structures reported as entries 81087, 42536, 42537, 8064, and 44752 in the Inorganic Crystal Structure Database.

In the latter and more recent study, Wolthers and co-workers presented a model of the initial FeS precipitate to explain their scattering results collected using a low-energy X-ray source (*49*). The model consisted of a disordered mixture of two mackinawite phases (30% MkA and 70% MkB) with the proportion of the minor phase (MkA) decreasing with aging. Two distinct primary crystallite sizes of 2.2 × 1.7 nm and 7.4 × 2.9 nm were calculated for MkA and MkB, respectively, using the Scherrer equation. Although TEM data were presented there were no images of individual crystallites to confirm the sizes calculated from XRD. The difficulties encountered in the application of peak-width-based analysis to nanocrystalline materials have been pointed out by Hall (*12*) and others. We believe that use of the Scherrer equation is questionable given the limited quality of data obtainable using a low-energy X-ray source. However, it is interesting that the size reported for the minor phase (MkA) is approximately the same as the size reported in the present study. The unit cell parameters reported (MkA: $a = 4.0$ Å, $c = 6.7 \pm 0.1$ Å) and (MkB: $a = 3.7$ Å, $c = 5.5 \pm 0.2$ Å) would indicate that a relatively large relaxation of the atomic structure occurred and resulted in the distance separating the basal planes to increase as much as 33% from that of crystalline FeS. This proposed lattice expansion was explained by the effects of intercalated water molecules and small crystallite size. It was also used in part to explain the high adsorptive capacity of the initial FeS precipitate for divalent metals also noted in previous studies (*44, 50-52*). In the present study we find that no significant relaxation is observed in the structure of FeS_{fresh} and FeS_{aged} as represented in the refined unit cell parameters derived from PDF analysis. Further, the initial precipitate formed is both single-phase and nanocrystalline mackinawite even under varying pH conditions.

Conclusions

Amorphous, or X-ray amorphous, is a common term used in the geo- and marine sciences communities to describe mineral precipitates lacking long-range order. The initial FeS precipitate has long been described in this way primarily from observations made using traditional XRD techniques. An amorphous solid by definition refers to a material in which the positions of atoms are lacking long-range order. On short-range scales (< ~1 nm), however, amorphous solids typically do exhibit order. It is difficult to make the distinction between materials that are truly amorphous and solids in which the size of the crystallites are extremely small. Electron imaging and traditional XRD techniques may have difficulty in distinguishing between amorphous and crystalline structures on these length scales. The relatively recent application of high-energy XRD and PDF analysis to nanocrystalline solids provides a new tool for adequately characterizing and understanding such materials. This study shows that the initial FeS precipitate is in fact highly-ordered over short- and medium-range atomic scales even with such extremely small crystallites. Hence, the initial FeS precipitate is better described as a nanocrystalline material with mackinawite structure. Work in progress exploring pH effects on particle size, growth mechanisms, growth rate and morphology using time-resolved method experiments and Reverse Monte Carlo simulations will be included in upcoming communications.

References

1. R. T. Wilkin, H. L. Barnes, *Geochimica et Cosmochimica Acta* **60**, 4167 (1996).

2. R. H. Parkman, J. M. Charnock, N. D. Bryan, F. R. Livens, D. J. Vaughan, *American Mineralogist* **84**, 407 (1999).

3. M. Wolthers, Ph.D.thesis (2003).

4. J. W. Morse, F. J. Millero, J. C. Cornwell, D. Rickard, *Earth-Science Reviews* **24**, 1 (1987).

5. M. Mullet, S. Boursiquot, J. Ehrhardt, *Colloids and Surfaces A: Physicochemical and Engineering Aspects* **244**, 77 (2004).

6. R. A. Berner, *American Journal of Science* **268**, 1 (1970).

7. R. Donald, G. Southam, *Geochimica et Cosmochimica Acta* **63**, 2019 (1999).

8. M. A. A. Schoonen, H. L. Barnes, *Geochimica et Cosmochimica Acta* **55**, 1505 (1991).

9. T. Egami, *Journal of Physics and Chemistry of Solids* **56**, 1407 (1995).

10. T. Egami, S. J. L. Billenge, *Underneath the Bragg Peaks: Structural Analysis of Complex Materials*. R. W. Cahn, Ed., Pergamon Materials Series (Elsevier, Oxford, 2003), pp.

11. S. J. L. Billinge, V. Petkov, T. Proffen, *Commission on Powder Diffraction of the International Union of Crystallography Newsletter* (2000).

12. B. D. Hall, D. Zanchet, D. Ugarte, *Journal of Applied Crystallography* **33**, 1335 (2000).

13. R. B. Neder, V. I. Korsunskiy, *Journal of Physics-Condensed Matter* **17**, S125 (2005).

14. K. Page *et al.*, *Chemical Physics Letters* **393**, 385 (2004).

15. R. A. Berner, *American Journal of Science* **265**, 773 (1967).

16. R. B. Herbert, S. G. Benner, A. R. Pratt, D. W. Blowes, *Chemical Geology* **144**, 87 (1998).

17. D. Rickard, *Chemical Geology* **78**, 315 (1989).

18. I. B. Butler, M. A. A. Schoonen, D. T. Rickard, *Talanta* **41**, 211 (1994).

19. D. Rickard, *Stockholm Cont. Geology* **20**, 67 (1969).

20. A. R. Lennie, S. A. T. Redfern, P. F. Schofield, D. J. Vaughan, *Mineralogical Magazine* **59**, 677 (1995).

21. U. Rutt *et al.*, *Nuclear Instruments & Methods in Physics Research A* **467-468**, 1026 (2001).

22. S. D. Shastri *et al.*, *Journal of Synchrotron Radiation* **9**, 317 (2002).

23. "Fit2D" V. 9.129 Reference Manual V. 3.1.

24. A. P. Hammersley, S. O. Svenson, M. Hanfland, D. Hauserman, *High Pressure Research* **14**, 235 (1996).

25. X. Qiu, J. W. Thompson, S. J. L. Billinge, *Journal of Applied Crystallography* **37**, 110 (2004).

26. P. J. Chupas *et al.*, *Journal of Applied Crystallography* **36**, 1342 (2003).

27. T. Proffen, S. J. L. Billinge, *Journal of Applied Crystallography* **32**, 572 (1999).

28. V. Petkov, S. J. L. Billinge, J. Heising, M. G. Kanatzidis, *Journal of the American Chemical Society* **122**, 11571 (2000).

29. V. Petkov *et al.*, *Physical Review B* **65** (2002).

30. B. H. Toby, T. Egami, *Acta Crystallographica Section A* **48**, 336 (1992).

31. A. R. Lennie, D. J. Vaughan, in *Special Publication - Geochemical Society* M. D. Dyar, C. McCammon, M. W. Schaefer, Eds. (1996), vol. 5, pp. 117-131.

32. G. A. Waychunas, in *Nanoparticles and the Environment* J. F. Banfield, A. Navrotsky, Eds. (The Mineralogical Society of America, Washington, D.C., 2001), vol. 44, pp. 105-162.

33. D. Rickard, M. A. A. Schoonen, G. W. Luther, in *Geochemical Transformations of Sedimentary Sulfur* M. A. Vairavamurthy, M. A. A. Schoonen, Eds. (Am. Chem. Soc., Washington, D.C., 1995), vol. 612, pp. 168-193.

34. R. L. Joesten, *Rev. Mineral.* **26**, 507 (1991).

35. R. L. Penn, J. F. Banfield, *American Mineralogist* **83**, 1077 (1998).

36. J. P. Wilcoxon, G. A. Samara, *Physical Review B* **51**, 7299 (1995).

37. L. G. Benning, R. T. Wilkin, H. L. Barnes, *Chemical Geology* **167**, 25 (2000).

38. J. O. Fossum *et al.*, *Energy* **30**, 873 (2005).

39. J. C. Cornwell, J. W. Morse, *Marine Chemistry* **22**, 193 (1987).

40. H. M. Rietveld, *Journal of Applied Crystallography* **2**, 65 (1969).

41. P. Scherrer, *Göttin Nochricht* **2**, 98 (1918).

42. R. A. Young, in *IUCr monographs on crystallography* R. A. Young, Ed. (Oxford University Press, 1993), vol. 5, pp. 1-38.

43. S. J. L. Billinge, M. G. Kanatzidis, *Chemical Communications* **7**, 749 (2004).

44. W. A. Kornicker, Ph.D., Texas A&M University (1988).

45. D. Rickard, G. W. Luther, *Geochimica et Cosmochimica Acta* **61**, 135 (1997).

46. D. T. Rickard, *American Journal of Science* **275**, 636 (1975).

47. P. Taylor, T. E. Rummery, D. G. Owen, *Journal of Inorganic Nuclear Chemistry* **41**, 1683 (1979).

48. A. M. Widler, T. M. Seward, *Geochimica et Cosmochimica Acta* **66**, 383 (2002).

49. M. Wolthers, S. J. Van der Gaast, D. Rickard, *American Mineralogist* **88**, 2007 (2003).

50. T. Arakaki, J. W. Morse, *Geochimica Cosmochimica Acta* **57**, 9 (1993).

51. J. W. Morse, T. Arakaki, *Geochimica Cosmochimica Acta* **57**, 3635 (1993).

52. M. J. Wharton *et al.*, *Applied Geochemistry* **15**, 347 (2000).

Crystallographic Information File

```
data_Initial_FeS_Precipitate

_ccdc_journal_manuscript_code     cm050886b
_publ_requested_journal           Chemistry of Materials
_publ_contact_author_name         'F. Marc Michel'
_publ_contact_author_address
;Department of Geosciences
Stony Brook University
255 Earth & Space Sciences Bldg.
Stony Brook, NY 11794-2100
;
_publ_contact_author_email        fmichel@ic.sunysb.edu
_publ_contact_author_phone        631-632-6839
_publ_contact_author_fax          631-632-8240

_audit_creation_method            'Created with Diamond
                                  (www.crystalimpact.com)'
_audit_creation_date              07-11-07
_audit_update_record              07-11-07
_chemical_name_systematic         'Initial FeS precipitate'
_chemical_formula_structural      'FeS'
_chemical_formala_sum             'FeS'
_chemical_name_mineral            Nanocrystalline Mackinawite
_chemical_formula_weight          87.913
_chemical_compound_source         Synthetic

_cell_length_a                    3.685(6)
_cell_length_b                    3.685(6)
_cell_length_c                    5.037(4)
_cell_angle_alpha                 90
_cell_angle_beta                  90
_cell_angle_gamma                 90
_cell_volume                      67.9
_cel_formula_units_z              2

_symmetry_cell_setting            hexagonal
_symmetry_space_group_name_H-M    'P 4/n m m'
_symmetry_int_table_number        129
_symmetry_space_group_name_Hall   'P_4ab_2ab_-1ab'

_diffrn_radiation_probe           x-ray
_diffrn_radiation_type            monochromatic
_diffrn_radiation_wavelength      0.107(6)
_diffrn_source                    synchrotron
_diffrn_source_type               'APS Beamline BESSRC 11-ID-C'

loop_
_symmetry_equiv_pos_site_id
_symmetry_equiv_pos_as_xyz
1 'x, y, z'
2 '1/2-x, 1/2-y, -z'
3 '1/2-y, 1/2+x, z'
4 '-x, -y, z'
5 '1/2+y, 1/2-x, z'
6 'y, -x, -z'
7 '-y, x, -z'
```

```
8 '1/2+x, 1/2-y, -z'
9 '1/2-x, 1/2+y, -z'
10 'y, x, -z'
11 '-y, -x, -z'
12 '1/2+x, 1/2+y, -z'
13 '-x, y, z'
14 'x, -y, z'
15 '1/2-y, 1/2-x, z'
16 '1/2+y, 1/2+x, z'

loop_
_atom_type_symbol
_atom_type_oxidation_number
Fe2+ 2
S2-  -2

loop_
_atom_site_label
_atom_site_type_symbol
_atom_site_symmetry_multiplicity
_atom_site_Wyckoff_symbol
_atom_site_fract_x
_atom_site_fract_y
_atom_site_fract_z
_atom_site_occupancy
_atom_site_attached_hydrogens
_atom_site_u_iso_or_equiv
Fe1 Fe2+ 2 a 0.00000 0.00000 0.00000 1.000 0.0 0.009(7)
S1 S2- 2 c 0.00000 0.50000 0.2550(1) 1.000 0.0 0.009(7)

#End of data_Initial_FeS_Precipitate
```

Chapter 4: Hydrothermal Synthesis of Pure α-Phase Manganese(II) Sulfide Without the Use of Organic Reagents

Reproduced with permission from Chemistry of Materials:

F. M. Michel [a,b], M. A. A. Schoonen [a,b], X. V. Zhang [c], S. T. Martin [c], J. B. Parise [a,b] (2006) Hydrothermal Synthesis of Pure α-Phase Manganese(II) Sulfide Without the Use of Organic Reagents, Chem. Mater., 18, 1726-1736, doi: 10.1021/cm048320v.

[a] Department of Geosciences, Stony Brook University, Stony Brook, NY, USA.
[b] Center for Environmental Molecular Science (CEMS)
[c] Division of Engineering and Applied Sciences,
Harvard University, Cambridge, MA, USA.

Abstract

Recent studies exploring the role of metal sulfides as (photo)catalysts in prebiotic synthesis reactions provide the impetus for finding carbon-free synthesis methods for metal sulfides. The decomposition of organosulfur and organometallic precursor compounds is often the protocol for synthesizing bulk metal chalcogenides, such as manganese sulfide (MnS). Here we report a hydrothermal synthesis method for the formation of MnS in which a $MnCl_2$ solution is injected into a preheated sulfide solution. By varying the temperature of injection and subsequent aging time, we can control the specific crystal phase of the product. Three MnS polymorphs are known and two of these, α-MnS and γ-MnS, form as pure phases in aqueous systems. The initial precipitate formed upon mixing of aqueous solutions of Mn(+II) and S(-II) at ambient temperature is nano-crystalline and is composed of a mixture of γ-MnS (wurtzite structure) and β-MnS (zinc blende structure). β-MnS has not previously been identified as forming under aqueous conditions. The initial binary-phase precipitate can be transformed to pure, highly crystalline γ-MnS by aging at temperatures as low as 150 °C within 3 days. Aging to yield pure α-MnS requires temperatures in excess of ~200 °C for 3 days.

Characterization of the products was performed using powder X-ray diffraction, high-energy X-ray total scattering and pair distribution function (PDF) analysis, dynamic light scattering (DLS), and transmission and scanning electron microscopy (TEM & SEM). Chemical analyses were performed using colorimetric techniques.

Introduction

Manganese sulfide (MnS) occurs naturally as alabandite (α-MnS) and is the subject of recent photoelectrochemical research to test the hypothesis that MnS may have played a role in prebiotic synthesis on early Earth (*1*). The use of crystalline MnS formed in the absence of any organosulfur compounds circumvents the introduction of additional sources of carbon in such photochemical studies. In this study we present an aqueous pathway to form pure α-MnS without the use of organosulfur reagents. Our findings are consistent with prior studies discussed below which indicated that the abundance of the various MnS phases precipitated by solvothermal methods was strongly dependent on reaction temperature and aging time. The formation of the thermodynamically stable α-phase is kinetically-inhibited at room temperature; however, under solvothermal conditions this phase will form readily at temperatures in excess of ~200 °C.

MnS crystallizes in one of three polymorphs, each with distinct physical and structural properties. The metastable beta (β) and gamma (γ) phases are pink and form at low temperatures with tetrahedrally-coordinated zinc blende (SG: $\boldsymbol{F}\bar{4}3m$) and wurtzite (SG: $\boldsymbol{P}6_3mc$) crystal structures, respectively. The thermodynamically stable alpha (α) phase forms at a relatively higher temperature with octahedrally-coordinated rock salt structure (SG: $\boldsymbol{F}m\bar{3}m$) and a green color. Early experimental work involving the magnetic, electrical, and optical properties of the MnS phases have been summarized elsewhere (*2*).

Various procedures have been reported for the formation of MnS in one or more of the three polymorphic forms. These include the reaction of elemental Mn and S at elevated temperatures(*3-5*) and deposition in the form of films(*6-13*), which, in at least one instance, was formed from the decomposition products of organometallic precursor compounds (*14*). In several other experimental studies, MnS was initially formed from inorganic precursors under aqueous conditions but was then dried and later transformed to α-MnS by heating at elevated temperatures (1000 °C) (*15, 16*). Prior studies have also reported the formation of both metastable polymorphs (β and γ) and stable (α) MnS using solvothermal synthesis techniques (*17-21*). To our knowledge, synthesis of MnS in all such prior studies relied on the use of elemental components or on the thermal decomposition of an organic precursor at elevated temperature in combination with extended aging (*9, 19, 21-23*). β-MnS, in particular, was previously observed to be formed only under nonaqeous conditions (*21*). This phase has the lowest free energy of formation of the MnS polytypes, followed closely by that of the γ-phase. Lu *et al.* (*19*) succeeded in forming β-MnS in an ether solvent (tetrahydrofurane) and γ-MnS in a hydrocarbon solvent (benzene). Both of the solvents used in this case were nonaqeous and nonpolar. This observation suggests that the precipitation kinetics within the Mn-S system are strongly dependent on the polarity of the solvent and on slight differences in the surface tensions of the three polymorphs.

The synthesis method presented here may also be useful to other applications for which a carbon-free MnS, which is a dilute semiconductor material, is desirable. Carbon-free synthesis routes have recently been explored as part of research investigating the fabrication of bulk superconducting materials such as Bi-based compounds and other superconducting cuprates (*24*). Studies on the synthesis of boron nitride nano-structures have also been hindered by carbon contamination due to the presence of carbon in the precursor reagents (*25*).

Experimental

Synthesis of MnS precipitates:

Pure metastable (γ) and stable (α) MnS crystallites were precipitated using two different protocols. Reagent solutions were prepared and MnS products were extracted at room temperature (22 ± 2 °C) in a glove box under N_2 atmosphere. The resulting product slurry was filtered over a membrane filter with 0.2-μm or 0.45-μm pores. The MnS precipitate collected on the filter was dried at room temperature under a stream of N_2 prior to characterization.

MnS Synthesis - Protocol A:

In one series of experiments using Protocol A, the reagents were mixed by the rapid direct injection of 20 mL of room temperature 0.2 M $MnCl_2$ into 22 mL of 0.05 M sulfide solution (NaSH/NaOH), which had been preheated to an elevated temperature of 230 ± 5 °C using a hydrothermal mixing apparatus as described below. Experimental details including heating times required to reach stable reaction temperatures are included in **Table 1**. The injection apparatus consisted of a 42-mL stainless steel reaction vessel, injection pump, temperature control components, and associated plumbing. This type of injection method has been utilized for more than 15 years in the synthesis of iron sulfides and other hydrothermal studies (*26, 27*). The reacted solutions were then aged at the injection temperature (230 ± 5 °C) for periods ranging from 5 ± 0.5 minutes up to 6 ± 0.1 hours. In a second series of experiments also using Protocol A, the reagents were mixed at elevated temperatures, ranging from 250 - 350 ± 5 °C, and then 'instantaneously' quenched to room temperature. Quenching was achieved by immersion of the sealed reaction vessel into a water bath at room temperature within approximately 5 minutes of mixing. (Due to the physical limitations of the injection apparatus, a short period of aging was inevitable but was limited to 5 ± 0.5 minutes from injection to quenching.) Each run remained in the room temperature water bath for a minimum of 20 minutes, and a temperature probe was used to verify that the reactor body thermally equilibrated with the water in the bath. A reduced concentration of the sulfide solution was employed in this protocol because of the corrosiveness of sulfide in stainless steel at elevated temperature.

Table 1: Sample identification, synthesis conditions, and analyses

Synthesis Protocol	Sample ID	Mixing Temp (°C)	Heating Time* (Hr)	Aging Temp (°C)	Aging Time (Min)	Phase	Analyses Presented			
							XRD	PDF	DLS	HACH
A	Inj-250	250	32	250	5	wur	X	X		X
	Inj -275	275	34	275	5	wur/rs	X			
	Inj -300	300	36	300	5	wur/rs	X			
	Inj -325	325	38	325	5	wur/rs	X			
	Inj -350	350	40	350	5	rs	X	X		X
A	Age-230A	RT	28	230	30	wur	X			
	Age-230B	RT	28	230	120	wur/rs	X			
	Age-230C	RT	28	230	180	wur/rs	X			
	Age-230D	RT	28	230	240	wur/rs	X			
	Age-230E	RT	28	230	360	rs	X	X		
B	Age-150	RT	20	150	3 days	wur		X		
B	Age-200	RT	25	200	3 days	rs		X		
--	RT-Fresh	RT	N/A	N/A	N/A	wur/zb	X	X	X	X

Note: *Heating time equals the total time required to reach and stabilize at the aging temperature designated. RT indicates reagents were initially mixed at room temperature (22 ±°C). XRD indicates data collected using Cu $K\alpha_1$ radiation. N/A indicates not applicable.

MnS Synthesis - Protocol B:

In Protocol B, the reagents (20 mL 0.2 M $MnCl_2$ into 42 mL 0.2 M sulfide solution) were mixed at room temperature (22 ± 5 °C) using the same hydrothermal mixing apparatus as above and subsequently heated to and aged at elevated temperature. Experimental details are again included in **Table 1**. In this protocol, the initial precipitate formed upon mixing of aqueous solutions of Mn and S at room temperature is a binary mixture of γ- and β-MnS. This precipitate is characterized as a part of this study. The poorly crystalline initial precipitate was subsequently heated to and aged at temperatures of 150 or 200 ± 5 °C for 72 ± 0.25 hours, thereby forming highly-crystalline γ- or α-MnS, respectively.

Chemicals:

$MnCl_2 \cdot 4H_2O$ (99 %) and $Na_2S \cdot 9H_2O$ (99 %) (hereafter referred to as NaSH/NaOH or sulfide) were from Fisher Chemicals. The chemicals were analytical grade and were used as received without additional purification. Solutions were prepared using water that was de-ionized (EasyPure, filtered 0.2 μm, UV/UF). and purged with N_2 (99.99 % pure) for at least 30 minutes to remove dissolved molecular oxygen (*28*).

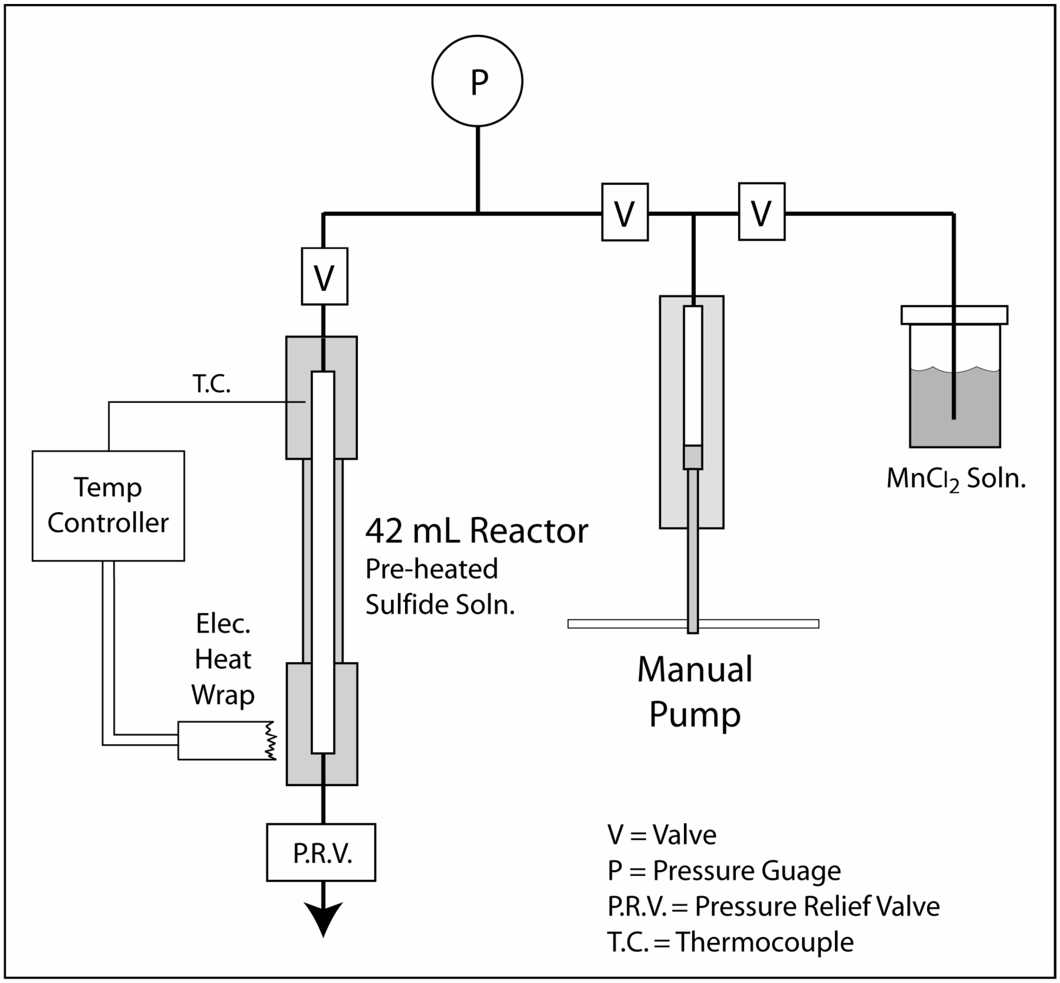

Figure 1: Hydrothermal mixing apparatus. A $MnCl_2$ solution is drawn into a manual injection pump while the sulfide solution is preheated to a desired reaction temperature in the 42-mL reaction vessel. The vessel, constructed of 316SS, is heated using electric heat wrap and maintained using an electronic temperature controller and Variac. A pressure relief valve allows the escape of some fluid the due to heating and volume expansion and the displacement of the sulfide solution at the time of injection of $MnCl_2$ (22 mL). The injection pressure is monitored using an in-line pressure gauge. The temperature of the vessel is monitored using a thermocouple connected to the controller unit.

Hydrothermal Apparatus:

The hydrothermal apparatus used in this study is based on a rapid injection design described in earlier work (*26, 27*). In brief, a 42-mL tube reactor was connected to a manual, high-pressure generator pump and a pressure relief valve (**Figure 1**). This pump was used to inject one of the reagents—here $MnCl_2$—into the reactor vessel containing the preheated sulfide solution (Protocol A only). A pressure relief valve was used to suppress boiling of the preheated sulfide solution before the $MnCl_2$ solution was injected using the hand pump. The relief valve also allowed some of the fluid to escape due to volume expansion during heating and the injection. The backpressure on the relief valve was set at 250 ± 10 bars. Reactor (High Pressure Equipment Company (HiP™)), relief valve (Swagelok™), hand pump (HiP™), and connecting tubing were made out of 316 stainless steel. The reactor was heated using a heavy-duty, insulated electric heat tape wrapped around the body of the reactor. The temperature of the reactor was maintained using a thermocouple-controller unit.

Characterization of MnS precipitates:

Characterization of the run products was carried out by XRD, electron microscopy (TEM & SEM), and/or pair distribution function analysis (PDF) analysis. Dynamic light scattering (DLS) was also attempted to determine particle size distribution. The poorly crystalline initial precipitate formed upon mixing of aqueous solutions of Mn and S at room temperature was also characterized. Total scattering data from high-energy synchrotron radiation and for pair distribution function analysis (PDF) were collected on selected samples. Total-Fe content in selected run products and their starting reagents were determined using colorimetric techniques. Sample identification and an overview of syntheses and characterization are described in **Tables 1 & 2**.

Table 2: General protocols (A & B) for product syntheses

Step	Action
Synthesis	Load sulfide solution in the 42 mL SS reaction vessel and pre-heat and pre-heat to desired reaction temperature (heating in protocol A only). Inject $MnCl_2$ solution Aging at elevated injection temperature for periods ranging from <5 min to 6 hours (protocol A only). Heating to and aging at elevated temperatures ranging from 150 – 200 ±5°C for 3 days (protocol B only). Quenching and extraction of liquid and solid (slurry) under N_2 atmosphere.
Rinse Cycle 1	Centrifuge initial slurry 5 minutes at 5,000 RPM Decant supernatant and add ~45 mL 1 mM sulfide solution Sonicate (1 min) and vortex (20 sec)
Rinse Cycle 2	*Repeat Cycle 1*
Rinse Cycle 3	Centrifuge 5 minutes at 5,000 RPM *Decant supernatant including
Extraction	Filter solid phase product Dry product under N_2 stream
XRD Mounts	Low-energy: Powders mixed into amorphous silicone grease to inhibit oxidation and mounted on glass slides
	High-energy: Powders loaded dry into 1 mm polyimide capillaries and capped with glass wool and epoxy
EM Mounts	Product mounted directly from colloidal suspensions obtained during Rinse Cycle 3* onto aluminum stubs (SEM) or carbon-coated, Cu grids (TEM)

*Supernatant included a stable suspension of colloidal MnS particles and was preserved for electron microscopic imaging. Note: During the rinse cycles described the samples were sealed in centrifuge tube and capped with $H_2 – N_2$ mix. Samples for DLS measurements were also prepared using the colloidal suspension from Rinse Cycle 3.

X-ray powder diffraction (Cu Kα_1 radiation):

Once dry, MnS powder samples inside the glove box were thoroughly mixed with an amorphous silicone vacuum grease to inhibit oxidation during slide preparation and XRD analysis. Powder X-ray diffraction patterns were collected using a Scintag PADx Diffractometer equipped with graphite monochromatized Cu Kα_1 radiation (λ = 1.5405 Å) and a scanning rate of 2.0°/min with 2θ ranging from 20° to 75°. The use of the silicone grease resulted in a background interference and created a "hump" in the intensity spectrum at low 2θ. The atomic structure-types of the run products formed at elevated temperatures using protocols A and B were determined using powder XRD techniques and comparison of the experimental patterns with the Joint Committee on Powder Diffraction Standards (JCPDS) database.

High-energy X-ray total scattering at the Advanced Photon Source (APS):

Selected powdered samples (RT-Fresh, Inj-250, Inj-350, Age-150, Age-200) were loaded into 1 mm O.D. polyimide (Kapton) capillaries under a completely anoxic atmosphere and capped at both ends with glass wool and epoxy, so as to inhibit oxidation. The loaded capillaries were then sealed under anoxic conditions in glass culture tubes with septum caps and transported to the APS. High-energy X-ray total scattering data were collected at the 1-ID beamline (99.9 keV, λ = 0.1240 Å or 79.9 keV, λ = 0.1551 Å (*29*)) of the APS. A CeO_2 standard (NIST diffraction intensity standard set: 674a) was used to calibrate the sample-to-detector distance and the tilt of the detector relative to the incident beam path. The energy calibration was initially achieved using the gold absorption edge as reference and, if increased to higher energies (i.e., 99.9 keV), was recalibrated by refinement of the wavelength and fixing of the sample-to-detector distance. The radiation scattered by the calibrant and samples was collected on a MAR-345 image plate detector system and processed using the program Fit-2D (*30, 31*). A polarization factor was applied during integration of the data. Data were also collected for an empty polyimide capillary (1 mm o.d.) for background correction during PDF analysis.

Pair Distribution Function (PDF) analysis:

The total scattering structure function $S(Q)$ and PDF $G(r)$ were obtained using PDFgetX2 (*32*) where standard corrections were applied as well as those unique to image-plate geometry (*33*). The Fourier transform of the normalized and weighted $S(Q)$, or $Q[S(Q)-1]$, results in the PDF, or $G(r)$, which corresponds to real-space inter-atomic distances. The unit cell for crystalline α- and γ-MnS each consist of two Mn and two S atoms. The unit cell for crystalline β-MnS consists of four Mn and four S atoms. The initial atomic coordinates, cell parameters, isotropic displacement parameters (U), and spacegroups $\boldsymbol{F}m\bar{3}m$, $\boldsymbol{P}6_3mc$, and $\boldsymbol{F}\bar{4}3m$ are those of the JCPDS database Powder Diffraction File No. 6-518, 40-1289, and 40-1288 for α-, γ-, and β-MnS polymorphs, respectively. The models for the crystalline MnS polymorphs are fitted to the experimental PDFs and the structural parameters of each model are refined and plotted using the programs PDFfit and Kuplot,(*34*) respectively. Unit cell parameters, isotropic-displacement parameters, atom positions, resolution dampening (σ_Q), a peak sharpening factor (δ), and a scale factor were refined simultaneously using PDFFit. A "goodness of fit" indicator (R_w) is reported for each refinement (**Table 3**). The two additional parameters δ and σ_Q are incorporated in the refinements to model sharpening of PDF near neighbor peaks due to correlated motion between atom pairs (δ) and the exponential decay of the PDF (σ_Q), respectively. The exponential decay of the PDF can, in certain cases, be attributed to a limited range of structural coherence in nano-crystalline materials, i.e., crystallite size.(*35-38*) In the case of highly crystalline samples, the exponential decay is primarily an indication of the resolution of the instrument (*38*) or instrument envelope. A crystalline CeO_2 standard was also analyzed during each of the two data collection events, and the results of the PDF refinements are included for comparison (**Table 3**).

Dynamic Light Scattering (DLS):

Particle sizes for several samples were measured using DLS techniques with a Brookhaven Instruments Corporation 90Plus/BI-MAS Particle Size Analyzer. The intensity correlation function of each sample was measured over five runs at a scattering angle of 90° from the incident laser beam (695 nm). Particle sizing by DLS is a non-invasive technique whereby the diffusion of particles in solution is measured through light scattering. As a result, samples can be examined under aqueous conditions. Particle sizes ranging from 150 to 10000 nm were determined from the autocorrelation function based upon the CONTIN (*39*) and Non-Negative Least Squares (*40*) analysis procedures.

Scanning & Transmission Electron Microscopy (SEM & TEM):

Run products selected for analysis by SEM and energy dispersive analysis using X-rays (EDAX) were extracted directly from the reaction vessel and drawn through a 0.2-μm polypropylene filter. The products were then washed with de-ionized water free of molecular oxygen and dried at room temperature using a stream of N_2. The solid-phase precipitate was then re-dispersed in ethanol and mounted on aluminum stubs. SEM was performed using a Leo 1550 equipped with a Schottky Field Emitting Gun and an EDAX Phoenix system. TEM imaging was performed on freshly precipitated MnS particles (RT-Fresh) using a Philips CM12 scanning TEM with a high brightness (LaB_6) electron gun. Colloidal MnS particles in solution were transferred under completely anoxic conditions, as described in **Table 2,** onto 300-mesh, 3-mm, carbon-coated copper grids with Formvar® and lacey carbon support film. The mounted grids were dried under a stream of N_2 and then stored temporarily in glass vials and capped under anoxic conditions for transport to the TEM. The grids were each exposed to atmospheric oxygen for less than one minute on average, while being transferred from the vials to a beryllium TEM sample holder, before being placed under high vacuum in the microscope.

Chemical Analyses:

Selected run products, dissolved in HCl (6 N), Fisher Chemicals (Certified A.C.S. Plus) were analyzed for total-iron content via colorimetric techniques using a HACH DR/4000 UV-vis Spectrophotometer and HACH Method 8147. Total-iron content was determined using the FerroZine fluorescence method (λ = 562 nm). The estimated minimum detection limit (EDL) was 0.004 mg/L. The FerroZine iron reagent forms a purple-colored complex with trace amounts of iron in samples that are buffered to a pH

Table 3: Refinement results from PDF analysis and comparison to crystalline standards

Parameter	**Age-150** $^{(1)}$ **(wur)**	**Inj-250** $^{(2)}$ **(wur)**	**γ-MnS****	**Age-200** $^{(2)}$ **(rs)**	**Inj-350** $^{(2)}$ **(rs)**	**α-MnS*****	**CeO$_2$** $^{(1)}$	**CeO$_2$** $^{(2)}$
a (Å) =	3.987(4)	3.974(9)	3.987	5.213(4)	5.213(8)	5.222(6)	5.407(0)	5.419(9)
c (Å) =	6.457(6)	6.430(3)	6.438	--	--	--	--	--
S z-position (Å)	0.3763(3)	0.3762(3)	0.375	--	--	--	--	--
R$_w$ (%)	19.9	17.4	--	17.6	10.5	--	28.9	17.5
σ_Q (Å^{-1})	0.036(1)	0.050(8)	--	0.028(3)	0.042(0)	--	0.033(3)	0.032(8)
δ	0.0756	0.104(9)	--	0.061(0)	0.071(4)	--	0.034(3)	0.053(6)
*U_{Mn} (Å^2)	0.010(2)	0.012(7)	--	0.008(3)	0.013(0)	--	0.006(1)	0.004(5)
*U_S (Å^2)	0.010(3)	0.012(6)	--	0.008(8)	0.013(0)	--	0.008(8)	0.023(7)
Aging	72 hours at ~150 °C	5 min at ~250 °C	--	72 hours at ~200 °C	5 min at ~350 °C	--	--	--

*U = isotropic-displacement parameter. **Cell parameters reported in ICSD-44765 for crystalline γ-MnS. *** Cell parameters reported in ICSD-76204 for crystalline α-MnS. $^{(1)}$ Indicates data collected at 1-ID (Energy = 79.9 keV). $^{(2)}$ Indicates data collected at 1-ID (Energy = 99.9 keV). "wur" and "rs" indicate fitting of the wurtzite (γ-MnS) and rock salt (α-MnS) models, respectively.

of 3.5. The color change is directly proportional to the concentration of iron present. Less than 0.5 g of each of the solid phase precipitates was dissolved in HCl. The precursor reagents at the same concentrations used in the syntheses were also analyzed to check for iron impurities.

Results & Discussion

Pure α-MnS was formed hydrothermally using both experimental protocols presented here. In one series of experiments using protocol A, α-MnS was formed via structural transformation of the metastable γ-phase after sufficient aging (6 hours) at 230 ± 5 °C. **Figure 2** presents XRD patterns for MnS formed using protocol A by direct injection at 230 ± 5 °C and subsequent aging for 0.5, 2, 3, 4, and 6 hours. The patterns for samples aged for 2, 3 and 4 hours show that both the α- and γ-phases are present simultaneously during the transition as a binary mixture. Here the abundance of α-phase crystals increases with aging time at the expense of the γ-phase. At 6 hours the phase transition is complete, and only the thermodynamically stable α-phase is detectable.

In a second series of experiments also using protocol A, α-MnS was formed this time by injection at temperatures in excess of ~325 °C. MnS samples were precipitated at temperatures ranging from 250 ± 5 to 350 ± 5 ºC. The aging time was limited to approximately five minutes. The XRD results indicate that, at temperatures between ~275 °C and ~325 °C, the products consist of a binary mixture of α- and γ-MnS with the relative abundance of α-phase increasing with reaction temperature (**Figure 3)**.

For MnS precipitated by protocol B (i.e., mixing of reactants at room temperature), the initial precipitate, without any subsequent aging at elevated temperature, is a binary mixture of the two metastable MnS polymorphs. The crystallinity of the initial precipitate is relatively poor, i.e., having broadened and weak XRD reflections and a rapid rate of oxidation upon exposure to air. These features are attributable to extremely small particle sizes which result from rapid and frequent nucleation at the time of mixing (*41*). Also contributing to the broadened maxima may be the effects of defects in the structures. The

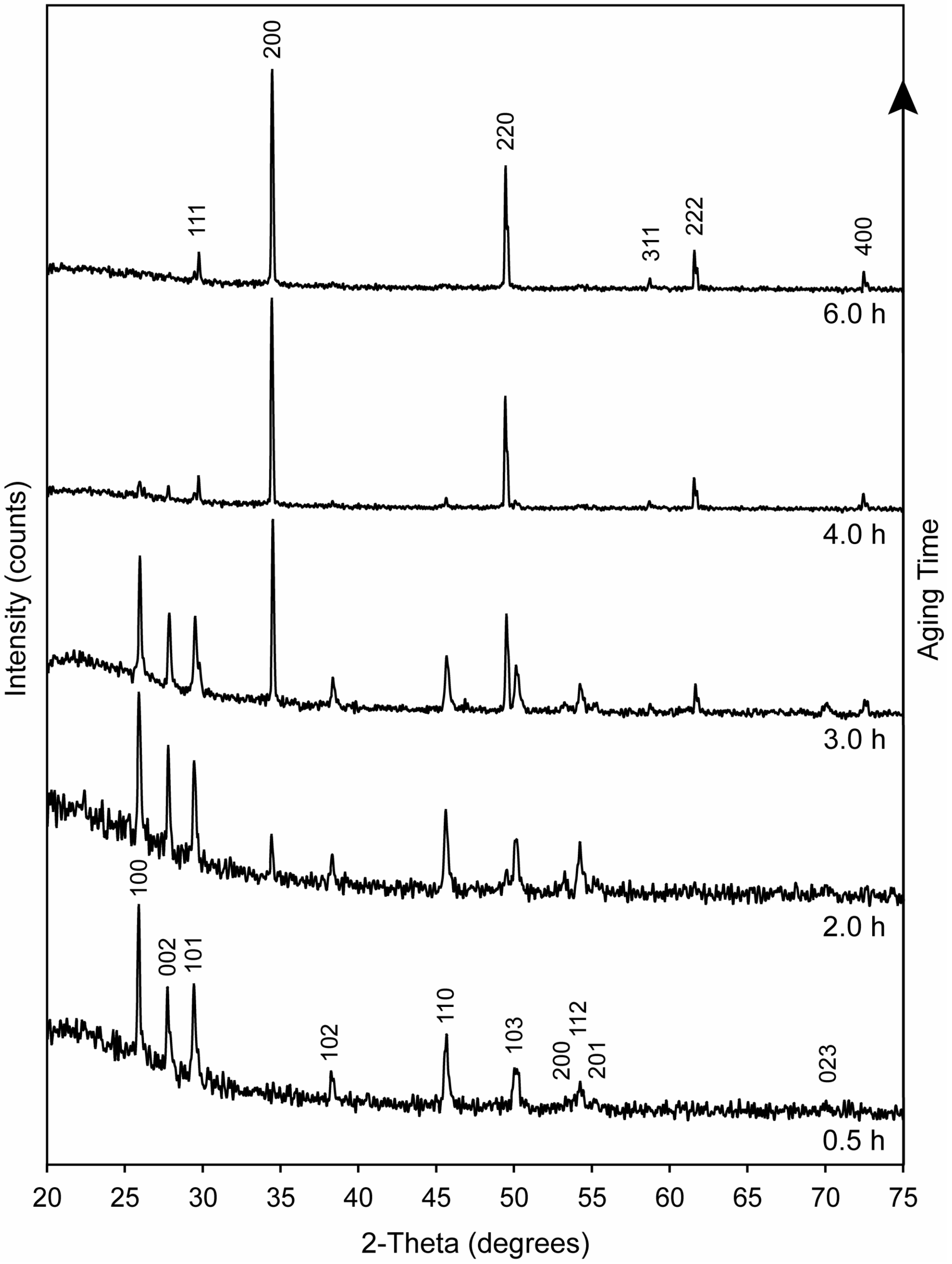

Figure 2: XRD for five MnS samples synthesized using protocol A. Mixing and aging occurred at 230 °C with aging times ranging from 0.5 to 6.0 hours. Aging time increases from bottom to top plot. MnS samples with shorter amounts of aging (0.5 and 2.0 hours) are dominantly γ-phase whereas samples aged 4.0 and 6.0 hours are dominantly α-MnS.

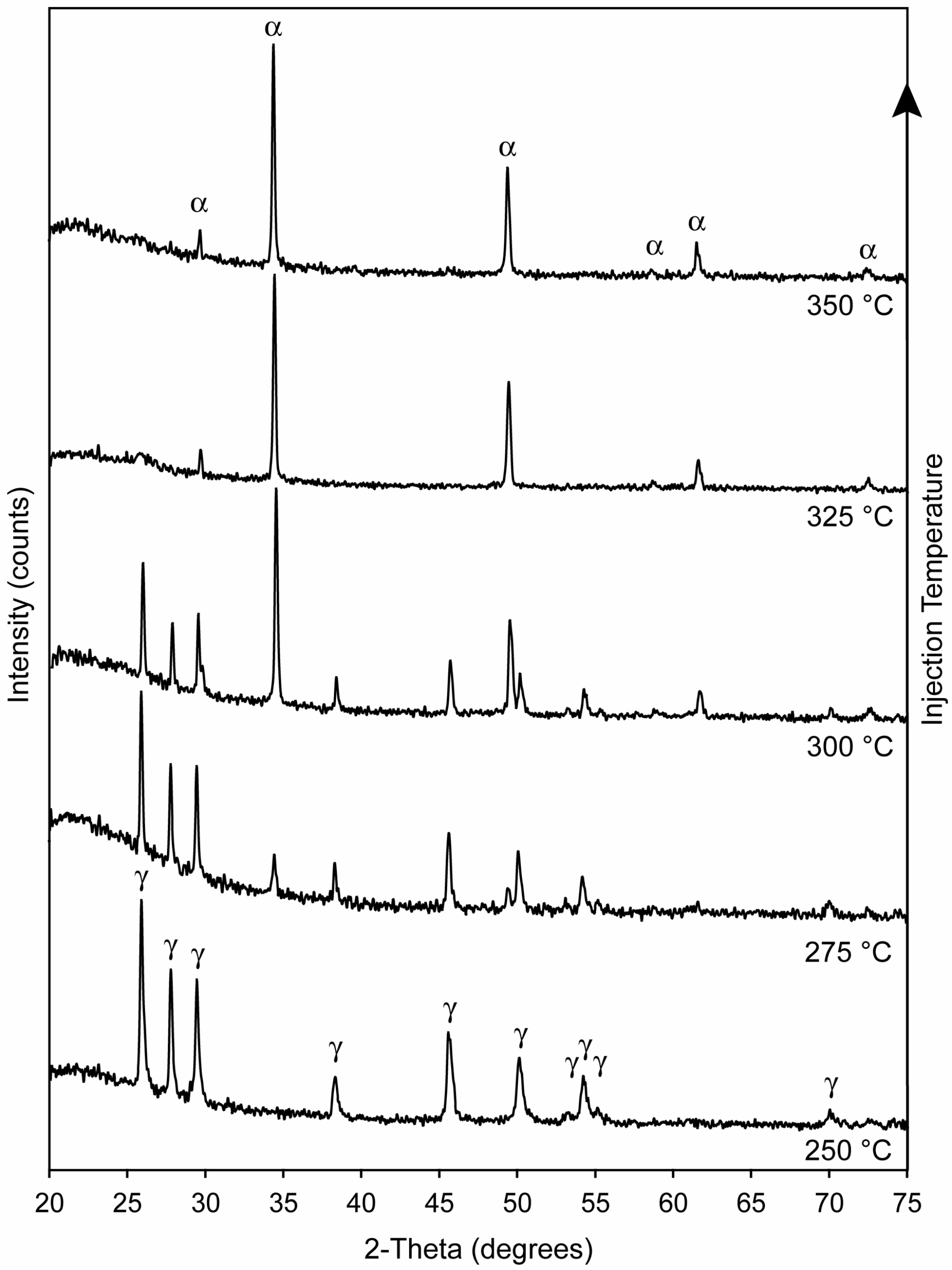

Figure 3: XRD for five MnS samples synthesized using protocol A by injection at temperatures ranging from 250°C to 350°C and aged less than 5 minutes. Injection temperature increases from bottom to top plot.

crystallinity of the initial metastable MnS precipitate improved when subsequent aging occurred at 150 °C (Sample: Age-150), as is indicated by a sharpening of the Bragg reflections and a relative increase in intensity. Sufficient aging at temperatures of 200 °C or higher using protocol B led to a complete structural transformation to form α-MnS (Sample: Age-200).

Atomic Structure from PDF:

Selected samples (RT-Fresh, Inj-250, Inj-350, Age-150 and Age-200) were evaluated using total scattering data and PDF analysis. Recently this technique has been applied successfully to studies of nano-crystalline materials for which traditional XRD techniques are limited (*38, 42, 43*). The usefulness of more traditional techniques like the Rietveld method (*44*) in refining the long-range atomic order of nano-crystalline materials have been limited by a broadening of the Bragg reflections resulting primarily from submicron particle sizes (*41, 45*). The diffuse scattering component of the total elastic scattering from the sample, characteristic of short-range order, is usually folded into the background correction in this methodology. However, the PDF method is well-suited in that it utilizes the total scattering of the sample, i.e. both the Bragg and diffuse components, and does not assume that the structure exhibits long-range periodicity (*46*). The PDF technique, originally developed to investigate the atomic order in liquids and glassy materials, has been described in detail elsewhere (*47*). In brief, the PDF has peaks at characteristic distances separating pairs of atoms and thus, $G(r)$ is a measure of the probability of finding an atom at a distance r from a reference atom and so describes the atomic arrangement (structure) of materials (*47*).

Several of these samples were anticipated to have dominantly nano-sized crystallites due to the lack of aging at the elevated mixing temperatures (Inj-250 and Inj-350) or lack of both heating and aging (RT-Fresh). For comparison, highly crystalline γ-MnS (Age-150) and α-MnS (Age-200) were formed through extended aging at elevated temperatures, and for these cases the cell parameters derived from PDF refinement are nearly identical with those reported for these phases in the JCPDS database (**Table 3**). The PDF model fits for Inj-250 (**Figure 4b**) and Inj-350 (**Figure 5b**) and the refined cell parameters (**Table 3**) indicate that these samples also are highly crystalline. This result was somewhat unexpected because these two samples experienced very short aging times and thus were anticipated to be extremely fine-grained. As discussed further below, the presence of nano-sized particles in either sample cannot be ruled out by PDF analysis alone because the PDF signal in a sample with a non-uniform distribution of particle sizes is dominated by the highly crystalline (largest) fraction. Therefore, electron imaging was also used to directly evaluate the distribution of particles sizes (see below).

In contrast to the highly crystalline run products, there are distinct regions of the PDF where the initial precipitate (RT-Fresh) is not adequately described on the basis of the structure of a single-phase model for either metastable polymorph. The top two panes in **Figure 4c** show the individual fits for wurtzite ("wur") and zinc blende ("zb"). Although the three nearest-neighbor atom pairs have a satisfactory fit by either model, there are obvious differences in peak positions and intensities at greater distances (r > ~4 Å), as indicated in the difference plots. The presence of a binary mixture of the metastable polymorphs is testable by fitting the experimental PDF with a dual-phase ("wur/zb") model (**Figure 4c – bottom pane**). The fit is significantly improved, as indicated in the difference plot and the refinement results (**Table 4**). The ability to fit the data with two end-member structures, each based on a periodic model, suggests the presence of two separate and coherently scattering phases. The scaling factors, refined individually for each phase, indicate a wurtzite to zinc blende ratio of approximately 2:1.

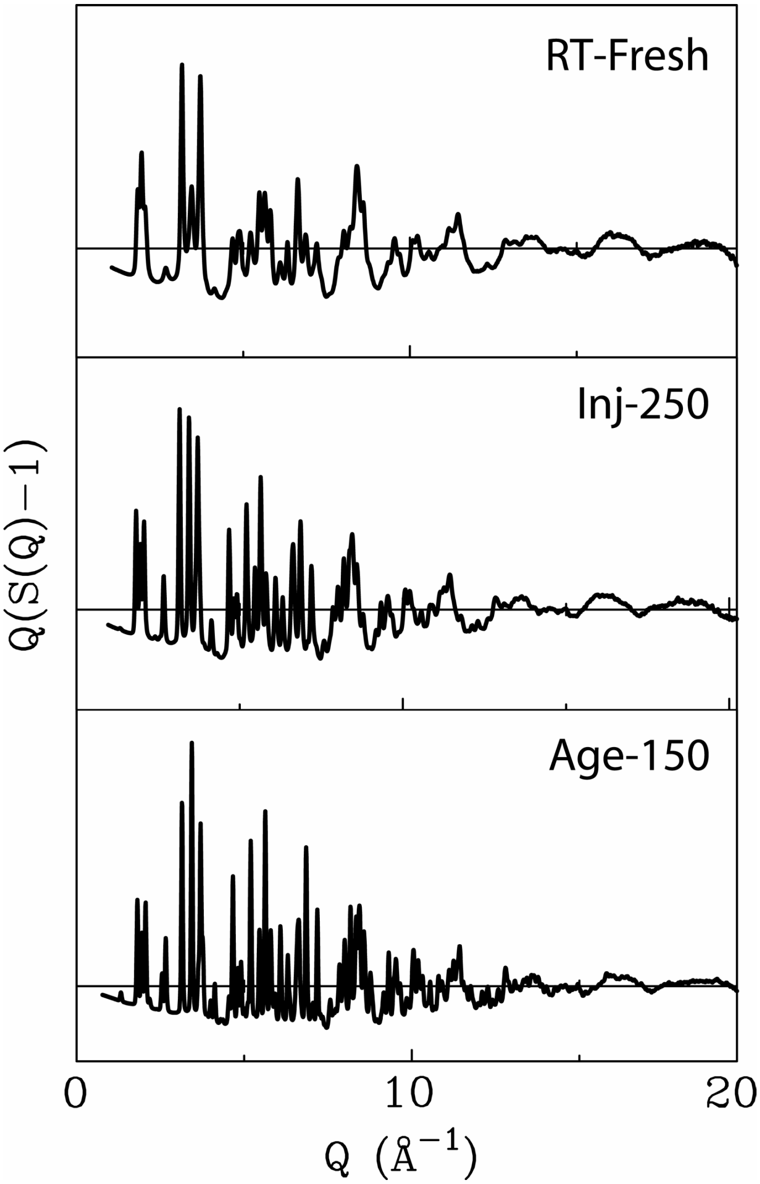

Figure 4a: The weighted total scattering structure function $Q[S(Q)-1]$ for run products (RT-Fresh, Inj-250, Age-150).

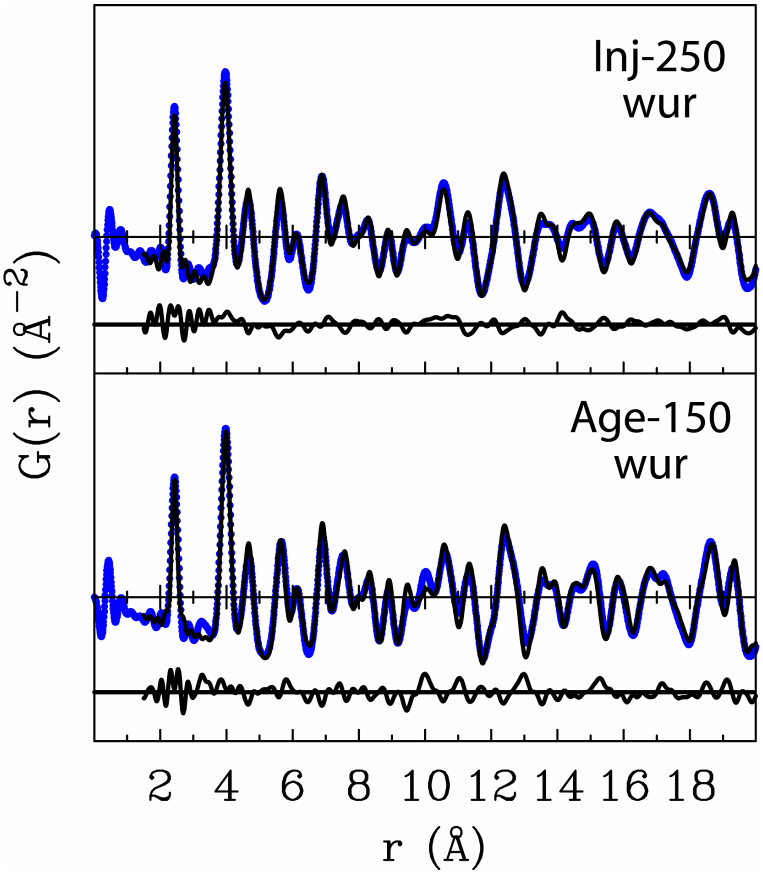

Figure 4b: The PDF *G*(*r*) versus distance *r* is plotted with the experimental data (blue circles) fitted by the refined model PDF (solid black) shown for samples Inj-250 and Age-150. The structure model for wurtzite (γ-MnS) is indicated by "wur". A difference plot is included beneath each data set as an indication of fit.

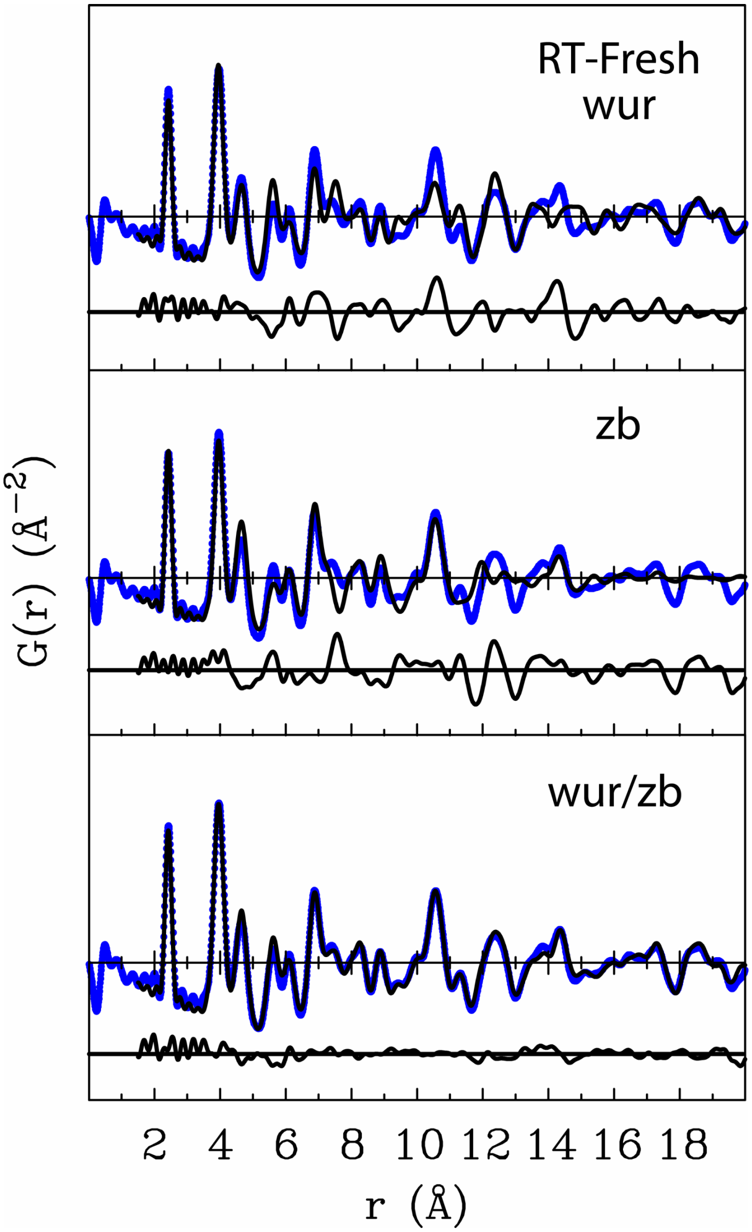

Figure 4c: The PDF *G*(*r*) versus distance *r* is plotted with the experimental data (blue circles) fitted by the refined model PDF (solid black) shown for sample RT-Fresh. The structure models for wurtzite (γ-MnS) and zinc blende (β-MnS) are indicated by "wur" and "zb". A difference plot is included beneath each PDF as an indication of fit

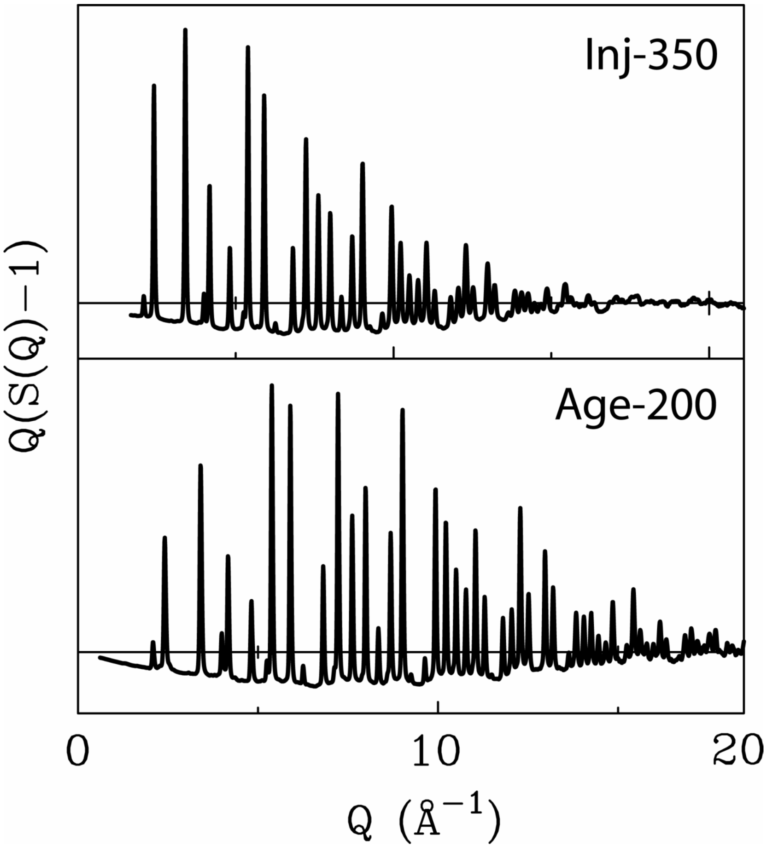

Figure 5a: The weighted total scattering structure function *Q*[*S*(*Q*)-1] for α-MnS run products (Inj-350, Age-200).

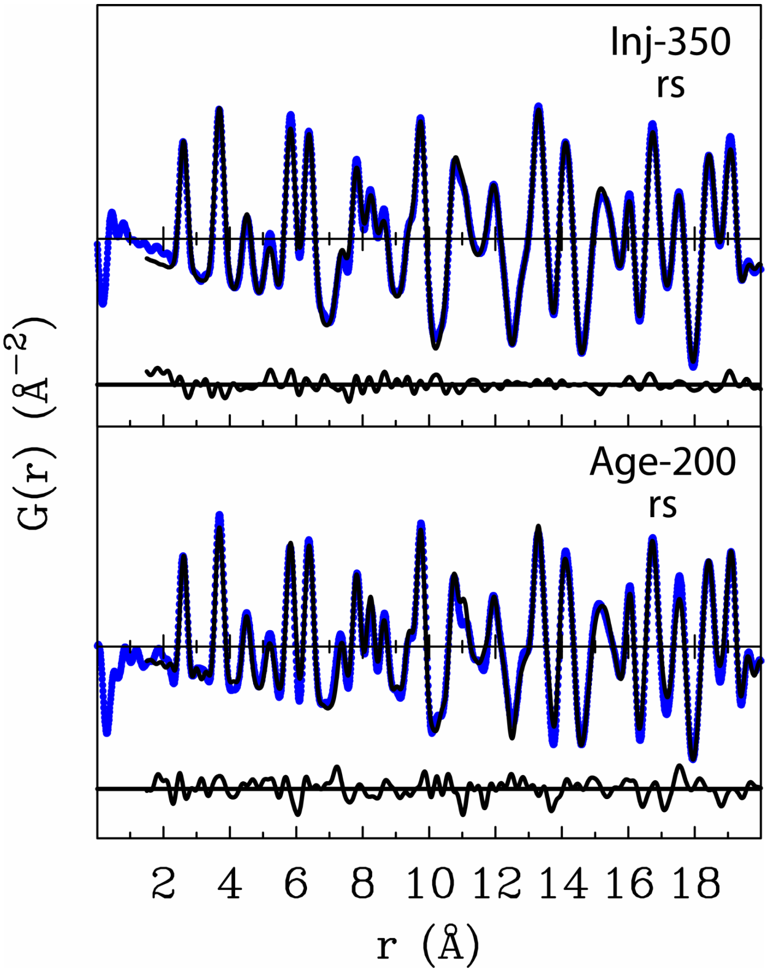

Figure 5b: The PDF $G(r)$ versus distance r is plotted with the experimental data (blue circles) fitted by the refined model PDF (solid black) shown for samples Inj-350 and Age-200. The structure model for cubic rock salt (α-MnS) is indicated by "rs". A difference plot is included beneath each PDF refinement set as an indication of fit.

The exact spatial relationship between the two MnS phases coexisting in the initial precipitate is not presently known. An alternative to the presence of a binary mixture of discrete phases would be zinc blende occurring as inter-growths or defects in a wurtzite host-structure (e.g., stacking faults or core-shell type nanoparticles). In the wurtzite structure, the occurrence of stacking faults are equivalent to alternating layers of wurtzite (ABAB stacking) and the closely related zinc blende structure (ABCABC stacking). This type of configuration is commonly observed in nanocrystalline CdSe (*48*), ZnSe (*49*), ZnO, and ZnS (*50*). Such planar defects in crystalline materials result in modifications in the intensities of specific peaks (e.g., [002] in zinc blende and [111] in wurtzite) as well as additional diffraction features, which are manifestations of the relationship between the two structure types. These features usually occur at slightly larger *d*-spacing with relatively less intensity. Due to broadening of the diffraction maxima any extra features become obscured by neighboring and often overlapping reflections. Such is the case in the initial nanocrystalline MnS precipitate (**Figure 4a – Top Pane**). Furthermore, in the case of extremely small particles, where the coherence length of the X-rays is comparable to the size of the intimately inter-grown phases, the overall scattering would be distinct from these phases occurring separately. Under such conditions, a satisfactory fit of the PDF would not be obtained by two separate models, each based on a periodic structure.

Table 4. PDF model refinement results (RT-Fresh)

	Single - phase				Dual – phase (wur/zb)	
Parameter	**γ-MnS (wur)**	**γ-MnS****	**β-MnS (zb)**	**β-MnS*****	**γ-MnS (wur)**	**β-MnS (zb)**
a (Å) =	3.972(1)	3.987	5.617(6)	5.606	3.969(9)	5.615(9)
c (Å) =	6.427(3)	6.438	--	--	6.440(2)	--
S z-position (Å)	0.382(1)	0.375	--	--	0.378(2)	--
R_w (%)	38.8	--	41.3	--	16.0	
σ_Q (Å^{-1})	0.080(2)	--	0.142(1)	--	0.071(2)	
δ	0.67(3)	--	0.74(8)	--	0.55(6)	
*U_{Mn} (Å^2)	0.014(2)	--	0.015(1)	--	0.015(1)	0.019(5)
*U_S (Å^2)	0.023(4)	--	0.029(3)	--	0.015(7)	0.027(3)
Scale Factor (%)	74	--	77	--	51	26

*U = isotropic-displacement parameter. **Cell parameters reported in ICSD-44765 for crystalline γ-MnS. ***Cell parameters reported in ICSD-44764 for crystalline β-MnS. (1) Indicates data collected at 1-ID (Energy = 79.9 keV). (2) Indicates data collected at 1-ID (Energy = 99.9 keV).

Crystal Morphology:

The morphology of the highly-crystalline run products formed using both experimental protocols was evaluated by SEM. The α-MnS crystallites precipitated by injection at room temperature and aging at elevated temperature (protocol B) were octahedrons having abundant intergrowths and twins (**Figure 7a)**. Increasing the injection temperature to 325 °C (protocol A) led to a morphology of the α-phase dominated by truncated cubes (**Figure 7b**). Although **Figure 7c** shows a nearly complete cube inter-grown between two larger octahedrons, fully formed cubes were rare in the α-MnS samples examined and formed using either experimental protocol. This result was possibly due to insufficient aging time. The γ-MnS sample formed using protocol A and examined by SEM had varied crystal sizes and morphologies and was in general dominated by hexagonal prisms and hexagonal dipyramids [**Figures 8a & 8b**]. The latter forms were bullet-shaped with varying dimensions. This morphology has also been observed in earlier studies (*22*). Low-resolution TEM images of the non-aged sample precipitated at room temperature (RT-Fresh) indicated a dominance of extremely small crystallites of 5 to 10 nm. The dominant morphology was difficult to discern at this resolution but appeared irregularly shaped in general (**Figures 9 & 10**).

Crystallite Size:

In the present study crystallite sizes in selected samples were evaluated primarily using electron microscopy (SEM or TEM). A wide size distribution of highly-crystalline MnS in both polymorphic forms was observed by SEM in the run products from both protocols A and B (**Figures 7a – 8b**). Individual crystallite sizes in these samples ranged from tens of nanometers up to and exceeding one micrometer. Although all of the run products inspected by SEM were filtered (0.2-μm), nano-sized particles were still visible (**Figures 7a, c and 8a – arrows**). Nano-sized particles would be expected to pass through a 0.2-μm filter and their presence may be in part due to a reduction in the effective pore size of the filter membrane during filtration.

The PDF for the initial MnS precipitate (RT-Fresh) shows a significant degree of attenuation within ~6 nm (**Figure 6**). The radial distance plotted along the abscissa is extended in Figure 6 to emphasize the attenuation at relatively short distances in the RT-Fresh sample compared to more crystalline samples (Age-150 and CeO_2). Beyond 6 nm, the correlations of RT-Fresh terminate and the pattern reduces to statistical noise. This degree of attenuation is not attributable to the resolution dampening factor (σ_Q) or instrument envelope (*34*) but instead arises from a limited range of structural coherence in the material. This envelope is evaluated independently using a highly crystalline sample of CeO_2 having particle sizes above 1-μm. From this standard, a refined value of σ_Q is obtained that has higher intensity correlations extending to a greater radial distance than for the nano-crystalline MnS. The nano-crystalline sample with a highly-attenuated PDF has a σ_Q value of 0.1, compared to that of 0.03 for crystalline CeO_2 (**Table 3**). Thus, from the apparent limited range of structural coherence, the average crystallite size of the freshly precipitated MnS crystallites is ~6 nm in diameter and may be greater or less in certain dimensions. This finding is consistent with TEM images (**Figures 9 & 10**).

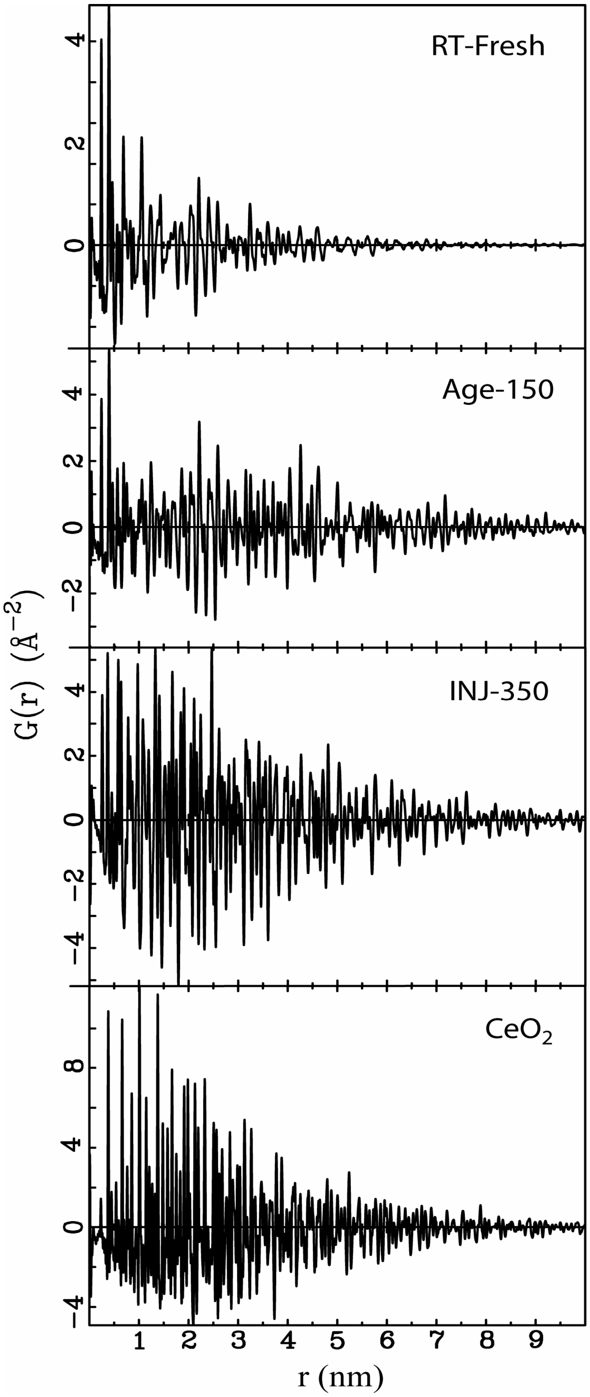

Figure 6: The PDF *G*(*r*) plotted out to 50 Å to illustrate the degree of attenuation due to the range of structural coherence (i.e., crystallite size) of the initial γ-MnS precipitate. The PDF for CeO_2 is also included to demonstrate the attenuation of a crystalline sample due to instrument resolution (1-ID). There is increased intensity and range in the correlations in the crystalline material.

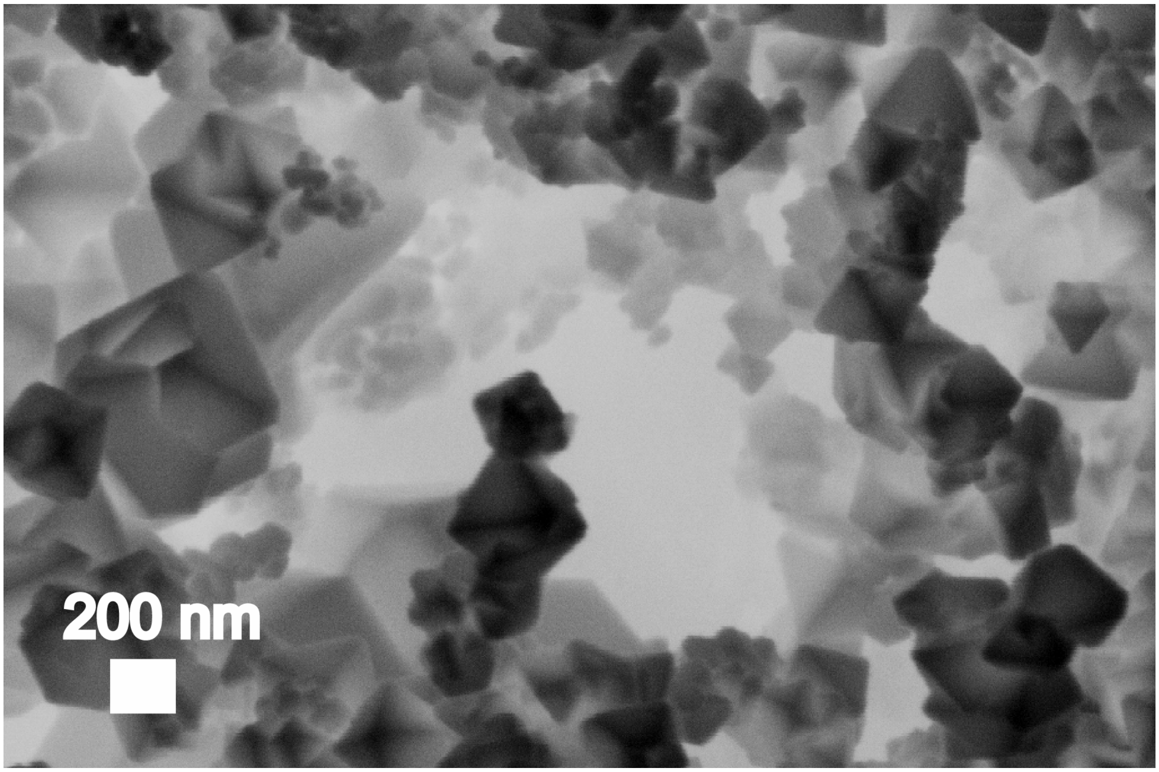

Figure 7a: SEM image of α-MnS formed by aging the initial MnS precipitate (precipitated at room temperature) for 3 days at 200 °C (protocol B). Morphology dominated by octahedron forms with sizes ranging from tens of nanometers to one micrometer. Arrow pointing at crystallites with sizes on the order of tens of nanometers. Marker indicates 200 nm.

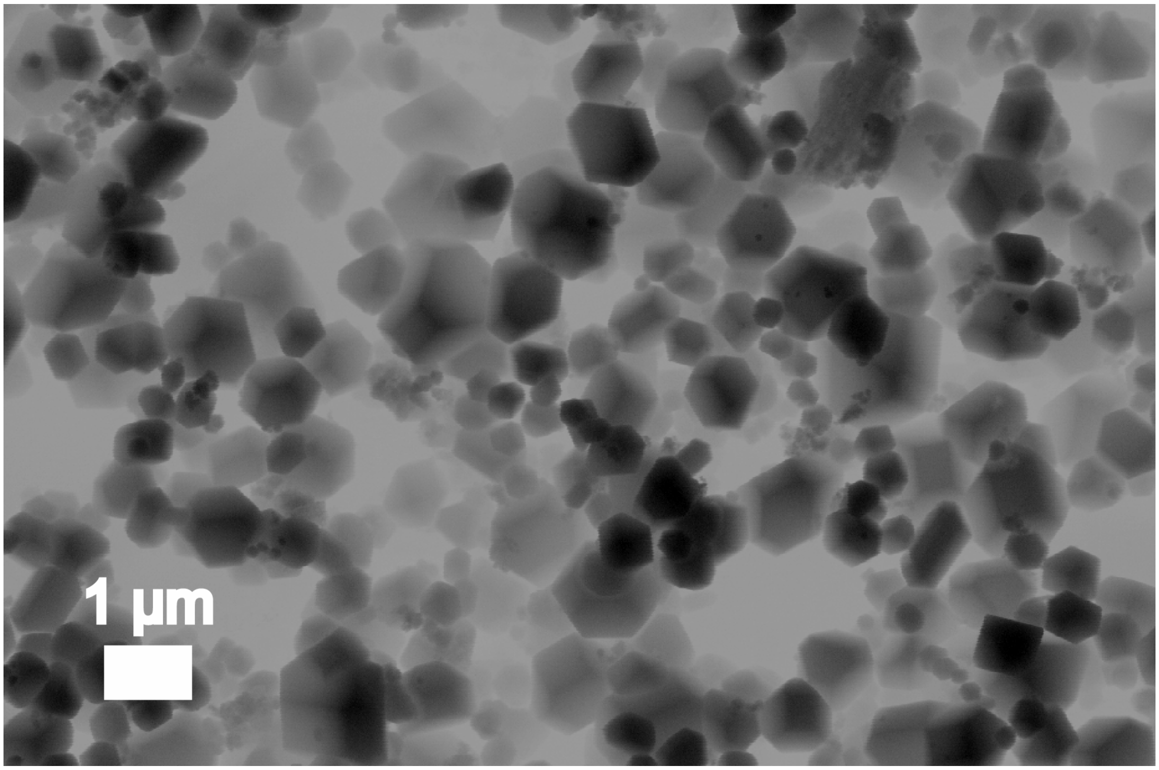

Figure 7b: SEM image of α-MnS precipitated and aged at 325 °C and aged for 27 hours (protocol A). Morphology dominated by truncated cubic forms with sizes ranging from hundreds of nanometers up to and exceeding one micrometer. Marker indicates 1 μm.

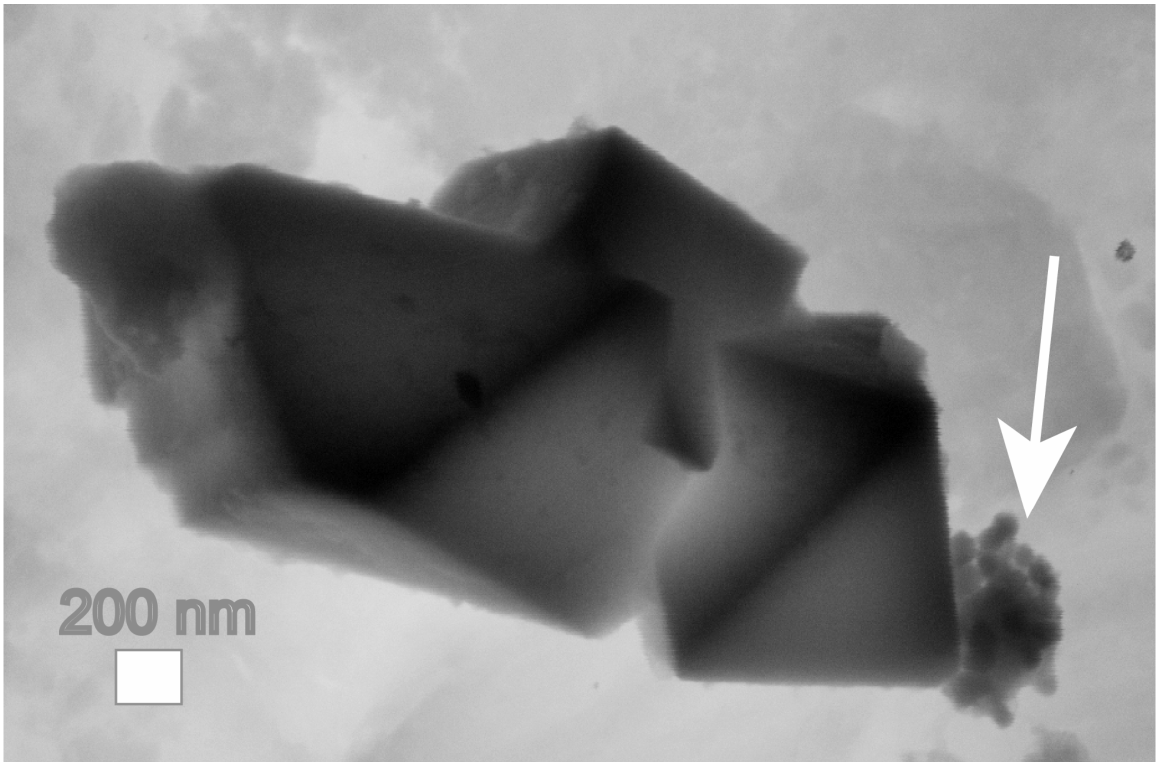

Figure 7c: SEM image of α-MnS precipitated at room temperature and aged more than 20 hours at 200 °C (protocol B). Morphology includes two octahedrons positioned on either side of a nearly complete cube. Arrow pointing at crystallites with sizes on the order of tens of nanometers. Marker indicates 200 nm.

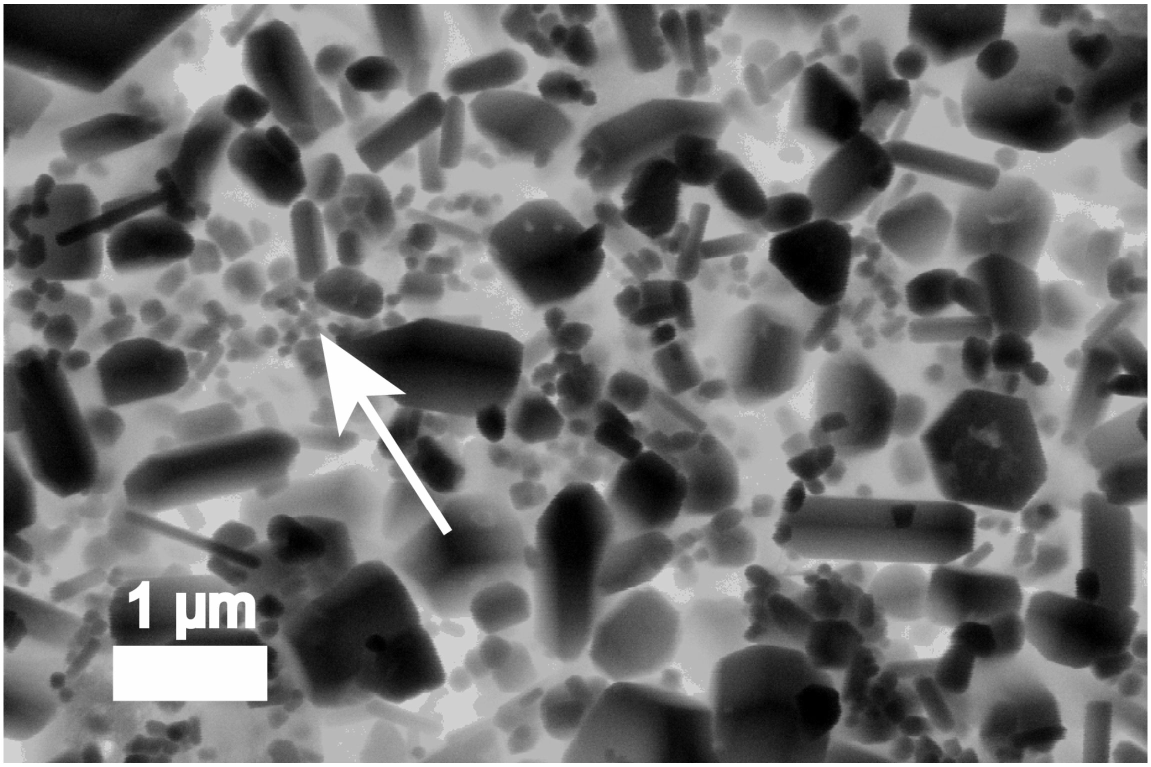

Figure 8a: SEM image of γ-MnS precipitated and aged at 170 °C for more than 20 hours (protocol A – XRD not presented). Morphology includes many size and shape variations on hexagonal prisms and hexagonal dipyramids. Sizes range from tens of nanometers to micrometers. Arrow pointing at crystallites with sizes on the order of tens of nanometers. Marker indicates 1 µm.

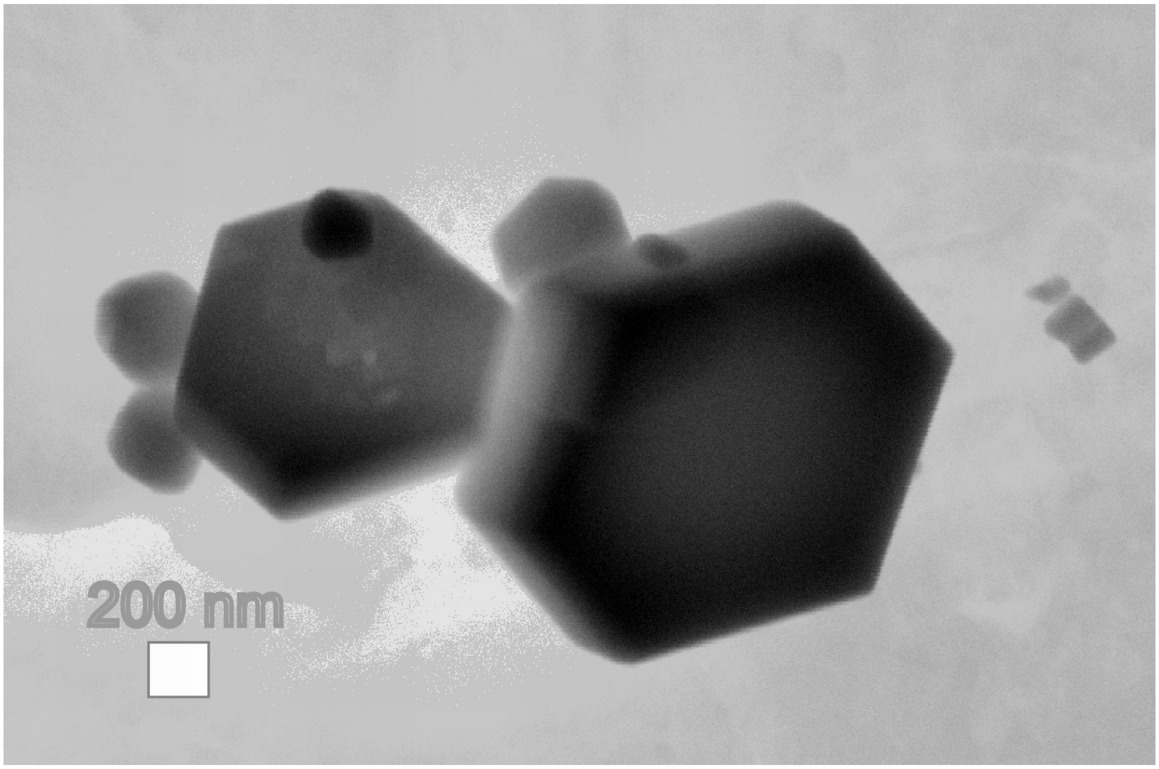

Figure 8b: SEM image of γ-MnS precipitated and aged at 170 °C for more than 20 hours (same sample as Figure 8a). Morphology includes relatively large hexagonal prisms approximately 1 μm in diameter. Marker indicates 200 nm.

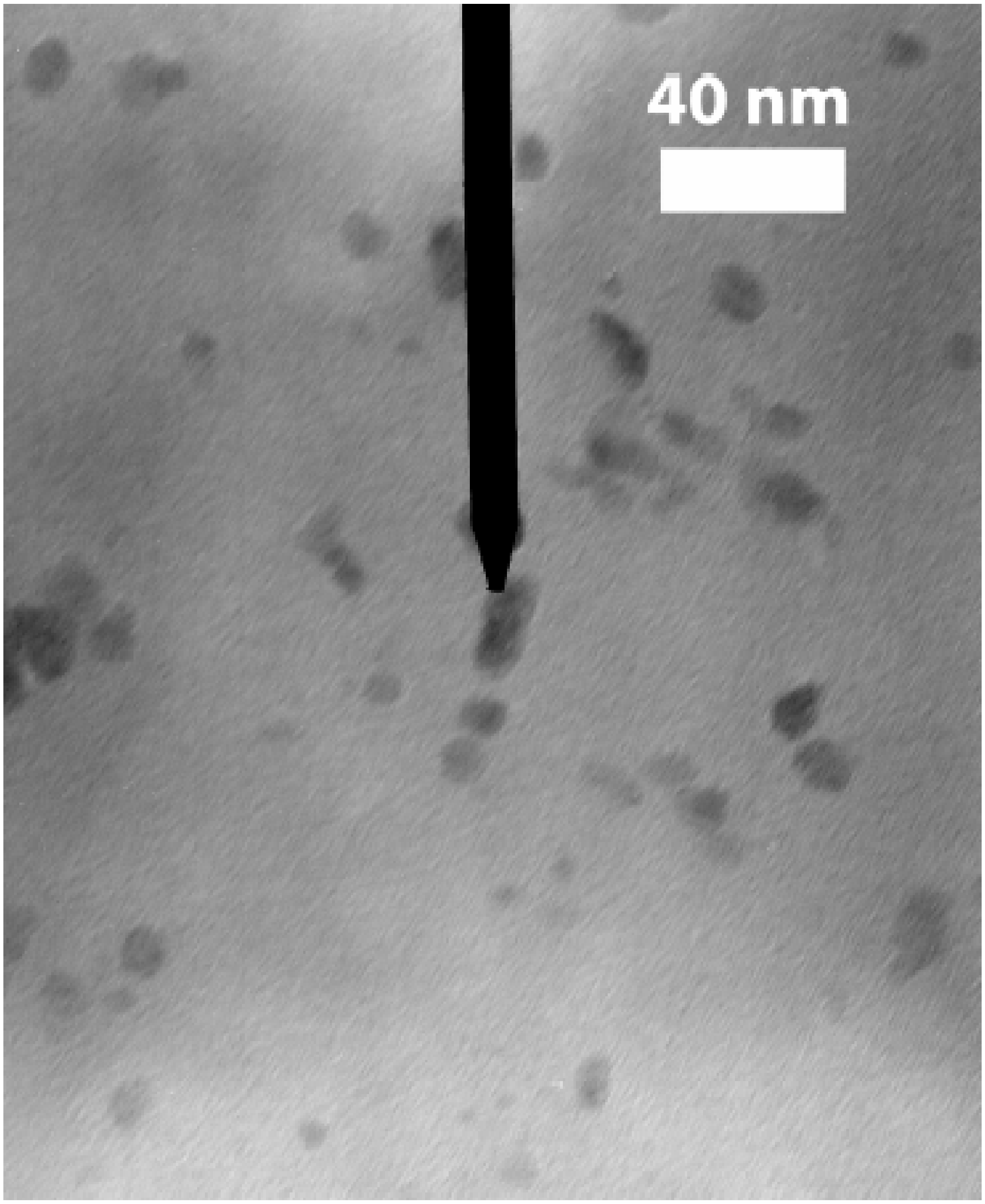

Figure 9: TEM image of the initial MnS precipitate (RT-Fresh) formed at room temperature with no additional heating or aging. The precipitate is nanocrystalline with sizes generally range from 5 to 10 nm with irregular morphology.

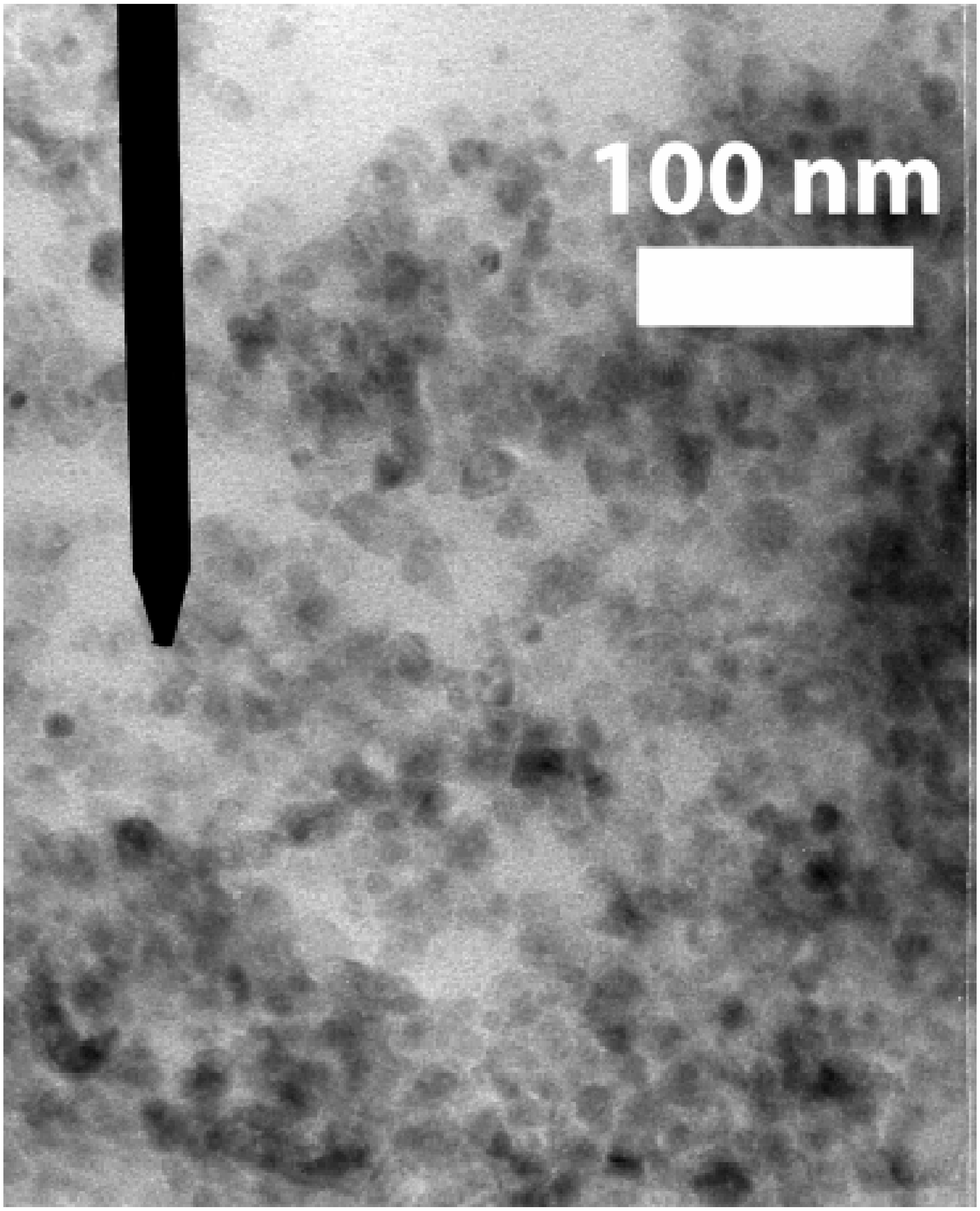

Figure 10: TEM image of the initial MnS precipitate (RT-Fresh) formed at room temperature with no additional heating or aging. Crystallites appear relatively monodisperse. Particle sizes generally range from 5 to 10 nm and are irregularly shaped.

Accurately determining crystallite size in natural and synthetic samples is commonly difficult to achieve by any one method. Various methods are often employed for measuring particle sizes, e.g., gas-sorption techniques (BET), microscopy, static or dynamic light scattering, or small-angle X-ray scattering (SAXS). In the Fe-S system, for example, the crystallite sizes reported in the literature for an initial precipitate have ranged from 2 – 400 nm as measured and calculated using a variety of these techniques (*51*). Although DLS, BET, and SAXS are statistically valid in that measurements are made over many particles, each of these techniques is of limited use in reporting individual crystallite sizes for samples that tend to aggregate in solution or as the result of processing (e.g., filtering or drying). Microscopic techniques, on the other hand, may be inaccurate because the number of particles examined is relatively low so that bias may be introduced by the observer. Recently, PDF analysis has been demonstrated as useful for determining the average particle size in nano-crystalline materials including ZnS (*42*), gold (*38*), and FeS (*43*). The PDF technique is statistically valid because the range of structural coherence is a mass-weighted indicator of crystallite size and is not affected by the aggregation. One drawback is that, for a sample having non-uniform distribution of particle sizes, the PDF signal becomes biased towards the largest particles (bulk) because they have long-range structural coherence. In this case, the high degree of attenuation in the PDF caused by the nano-sized fraction of particles may not be discernable in the presence of bulk particles.

The presence of structural disorder is also a factor that must be considered when attempting to extract particle size information from the PDF method. As discussed by Gilbert *et al.* (*42*), a discrepancy can exist between the size of finite particles estimated from PDF and that calculated from small-angle X-ray scattering or determined directly by electron imaging. Significant structural disorder (e.g., static disorder and/or strain) is caused in part by surface relaxation and internal strain found in extremely small particles and results in a loss of structural coherence, which is reflected in the PDF (*37, 42*). Static structural disorder causes broadening and loss of intensity for all PDF maxima. Broadened or shifted correlations can also arise from core-shell differences in a structure that has a large fraction of atoms on or near the surface of the crystallites compared to the interior (core). The TEM images of the present study, because of their low resolution, do not help in determining if the range of structural coherence in the PDF is solely a representation of the average particle size in a population of particles or if, instead, there is a significant component of disorder present. Since the nano-crystalline sample (RT-Fresh) was adequately fit by the two-phase bulk crystalline models (**Figure 4c**), such disorder may not be significant. The low-resolution TEM analysis in this study constrains the particles to less than 10 nm, which is reasonably close to the 6 nm determined from PDF. High-resolution TEM will be essential to further constrain the average particle size as well as to verify the spatial relationship between the two phases (γ and β) present in the sample.

Particle size determination from dynamic light scattering (DLS) showed a size distribution centered on approximately 5 μm (bimodal) for the initial MnS precipitate. Populations of particles were reported with a minimum size of 0.15 μm and maximum of 10 μm. These results are consistent with neither PDF nor TEM analyses. Furthermore, nano-sized particles would be anticipated in this method of synthesis because of the high supersaturation levels that result in the rapid nucleation of very small particles at the time of mixing (*42, 43*). The DLS technique becomes limited for determining individual crystallite sizes when there is aggregation of suspended particles in solution. Given that both PDF and TEM point to the presence of nano-scale particles, we conclude that the DLS-based distribution is likely to reflect the size distribution of aggregates in the slurry rather than the size distribution of the primary crystallites. A significant degree of aggregation was not avoided even when the pH of the solution was adjusted to a value well above its pH_{PZC}, which for MnS is less than 2 (*52*). DLS in this study was therefore not deemed to be a reliable tool for understanding the individual particle sizes of the run products.

Chemical Analysis:

EDAX analysis of the run products inspected by SEM confirmed manganese and sulfur as the primary components. An aluminum signal was also observed, which is attributable to the aluminum substrate of the mounting stub. A small peak, corresponding to the excitation energy of iron, also occurred, and was particularly evident in the products formed by preheating of the NaSH/NaOH solution to elevated temperature prior to mixing. Total iron content in selected run products and the initial starting reagents (**Table 5**) was evaluated using the UV-vis absorbance technique. For each of the three MnS samples, less then 400 mg of dry precipitate was dissolved in HCl and analyzed. The results indicate that the initial Mn(+II) and S(-II) reagents contain trace amounts of Fe. Incorporation of these Fe impurities in the MnS precipitate was confirmed by the analysis of the initial precipitate formed at room temperature. This sample was formed in a centrifuge tube and was never in contact with stainless steel. Leaching of iron from the 316 stainless steel vessel used in selected syntheses, particularly those conducted at elevated temperatures, was also confirmed. The heating of NaSH/NaOH solution to elevated temperatures apparently resulted in the corrosion of the interior surfaces of the vessel and the leaching of iron. The rate of leaching was apparently accelerated by increasing the pre-heat temperature of the NaSH/NaOH solution. The total Fe content measured in run products Inj-250 (0.001 wt. %) and Inj-350 (0.004 wt. %) corresponded to pre-heating of the NaSH/NaOH solution to 250 °C and 350 °C, respectively, prior to mixing. We cannot say if Fe replaced Mn in the MnS structure or if FeS was incorporated as clusters. However, in general the Fe content was trace (≤ 0.004 wt. %).

Product Yield:

The constraints on product yield vary for each protocol presented. For α-MnS formed at elevated temperature (>325 °C) using protocol A, the product yield is constrained primarily by the volume of reaction vessel and the concentration of the reagents. The total volume of the reaction vessel in this experimental setup was fixed at 42-mL, but a larger-volume vessel could also be employed. The maximum concentration of NaSH/NaOH was also a constraint in protocol A due to corrosion to the 316 stainless steel vessel, particularly when preheated to elevated temperature. The concentration of NaSH/NaOH was reduced to minimize the leaching of metal impurities (e.g., iron) from the stainless steel (*53*), and therefore acted as the limiting reagent. A vessel constructed of a titanium alloy (e.g., Ti-17) would be preferable to 316 stainless steel because it contains no iron and has a greater resistance to corrosion (*53*). The main drawback in utilizing vessels constructed of such materials (e.g., Ti) is that cost typically increases as much as five-fold.

Table 5: Analysis of total iron in solids

Sample ID	Total Iron (ppm)
RT-Fresh	1.25
Inj-250	10
Inj-350	40
Reagent	**Total Iron (ppm)**
$MnCl_2 \cdot 4H_2O$	3.2
$Na_2S \cdot 9H_2O$	2.2

The constraints on product yield in protocol B were not as strict as those for protocol A. This was primarily because the reaction of S(-II) and Mn(+II) forming MnS was conducted at room temperature, thereby reducing the corrosiveness of the reagent mixture by removing the majority of H_2S from solution. Hence, using a vessel constructed of stainless steel versus titanium is less critical for this protocol. The yield in protocol B is primarily constrained by the volume of the reaction vessel. By modifying protocol B to include a step in which the initial precipitate at room temperature is centrifuged to create a dense slurry, it is possible to increase the yield for a given reactor vessel considerably. In essence, by adding this step it is possible to age a larger quantity of MnS than can be precipitated in the reactor vessel itself. This method was successfully employed in a related study on ZnS (*54*) in which a ZnS was precipitated in a large-volume flask, centrifuged, supernatant removed, and the dense slurry loaded into a reaction vessel for aging at elevated temperatures. In protocol B, a slight excess of sulfide was added relative to $MnCl_2$ to ensure that the solution remained reducing during aging.

Conclusions

Three MnS polymorphs are known, and two of these, α-MnS and γ-MnS, were precipitated as pure phases under aqueous conditions without the use of organic reagents. Direct injection techniques using two experimental protocols were employed at temperatures ranging from 22 ± 3 ºC to 350 ± 5 ºC with varying amounts of aging time. The results confirm that varying the temperature of injection and subsequent aging time, the reaction can be directed towards production of a specific polymorph.

The initial MnS polymorph formed upon mixing is dependent on reaction temperature. The predominant phase precipitated from aqueous solutions of Mn(+II) and S(-II) at temperatures below 250 °C has tetrahedrally-coordinated wurtzite structure. At room temperature, the initial precipitate consists of a binary mixture of γ- and β-MnS. Given sufficient aging at temperatures of 200 °C and higher, the MnS makes a complete polymorphic transformation to the stable rock salt structure. MnS precipitated by direct injection at temperatures in excess of 325 ºC results in the formation of the thermodynamically stable α-phase within 5 minutes of mixing. The γ-phase could be the initial precipitate at these temperatures or instead it could rapidly transform to α-MnS in the 5 min prior to quenching.

A wide size distribution of MnS in both polymorphic forms was observed by a combination of techniques including SEM, TEM, and PDF in samples synthesized using both protocols A and B. Individual crystallite sizes in the samples synthesized and aged at elevated temperature ranged from tens of nanometers up to and exceeding one micrometer. Increasing the reaction temperature and aging time improved the crystallinity and increased the particles sizes. When formed at room temperature, the initial product is nano-crystalline and relatively monodisperse. This is of interest for us when evaluating nano-crystalline materials because disorder resulting from extremely small particle sizes may substantially modify the structural and chemical properties of the nano-phase when compared to the bulk. PDF analysis indicates, based upon the limited range of structural coherence, that the average crystallite size is ~6 nm. TEM images are consistent with these PDF results. Even so, the crystallite size obtained by this combination of techniques may still be insufficiently constrained if there are other factors such as surface relaxation or internal strain that would also affect the range of structural coherence in the PDF. Observations made by SEM indicate that the morphology of the α- and γ-MnS crystals are consistent with hexagonal and cubic structures, respectively.

References

1. X. V. Zhang, S. T. Martin, C. M. Friend, M. A. A. Schoonen, H. D. Holland, *Journal of the American Chemical Society* **126**, 11247 (2004).

2. C. N. R. Rao, K. P. R. Pisharody, *Progress in Solid State Chemistry* **10**, 207 (1976).

3. R. L. Clendenen, H. G. Drickamer, *Journal of Chemical Physics* **44**, 4223 (1965).

4. C. Sombuthawee, S. B. Bonsall, F. A. Hummel, *Journal of Solid State Chemistry* **25**, 391 (1978).

5. H. Wiedemeier, A. G. Sigai, *Journal of Crystal Growth* **6**, 67 (1969).

6. O. Goede, W. Heimbrodt, V. Weinhold, *Physica Status Solidi B* **136**, K49 (1986).

7. O. Goede, W. Heimbrodt, V. Weinhold, E. Schnurer, H. G. Eberle, *Physica Status Solidi B* **143**, 511 (1987).

8. E. Jahne, O. Goede, V. Weinhold, *Physica Status Solidi B* **146**, K157 (1988).

9. C. D. Lokhande *et al.*, *Thin Solid Films* **330**, 70 (1998).

10. M. Okajima, T. Tohda, *Journal of Crystal Growth* **117**, 810 (1992).

11. P. Praminik, M. A. Akhter, P. K. Basu, *Thin Solid Films* **158**, 271 (1988).

12. S. Sivananthan *et al.*, *Journal of Crystal Growth* **159**, 94 (1996).

13. B. J. Skromme, Y. Zhang, D. J. Smith, S. Sivananthan, *Applied Physics Letters* **67**, 2690 (1995).

14. R. Nomura, K. Konishi, S. Futenma, H. Matsuda, *Applied Organometallic Chemistry* **4**, 607 (1990).

15. L. D. Ahuja, D. Rajeshwar, K. C. Nagpal, *Journal of Colloid and Interface Science* **123**, 380 (1987).

16. J. J. Banewicz, R. Lindsay, *Physical Review* **104**, 318 (1956).

17. Y. Jun, Y. Jung, J. Cheon, *Journal of American Chemical Society* **124**, 615 (2002).

18. S. W. Kennedy, K. Harris, E. Summerville, *Journal of Solid State Chemistry* **31**, 355 (1980).

19. J. Lu *et al.*, *Chemistry of Materials* **13**, 2169 (2001).

20. Y. Zhang, H. Wang, B. Wang, H. Yan, M. Yoshimura, *Journal of Crystal Growth* **243**, 214 (2002).

21. Y.-C. Zhang *et al.*, *Optical Materials* **23**, 433 (2003).

22. J. Joo *et al.*, *Journal of American Chemical Society* **125**, 11100 (2003).

23. S. Wang, K. Li, R. Zhai, H. Wang, *Materials Chemistry and Physics* **91**, 298 (2005).

24. C. C. Tang, Y. Bando, T. Sato, *Applied Physics A: Materials Science & Processing* **75**, 681 (2002).

25. T. B. Tong, C. R. Li, *Chinese Journal of Physics* **36**, 280 (1998).

26. S. R. Poulson, M. A. A. Schoonen, *Chemical Geology* **116**, 305 (1994).

27. M. A. A. Schoonen, H. L. Barnes, 1991, *Geochimica et Cosmochimica Acta* **55**, 1495 (1991).

28. I. B. Butler, M. A. A. Schoonen, D. T. Rickard, *Talanta* **41**, 211 (1994).

29. S. D. Shastri *et al.*, *Journal of Synchrotron Radiation* **9**, 317 (2002).

30. "Fit2D" V. 9.129 Reference Manual V. 3.1.

31. A. P. Hammersley, S. O. Svenson, M. Hanfland, D. Hauserman, *High Pressure Research* **14**, 235 (1996).

32. X. Qiu, J. W. Thompson, S. J. L. Billenge, *Journal of Applied Crystallography* **37**, 678 (2004).

33. P. J. Chupas *et al.*, *Journal of Applied Crystallography* **36**, 1342 (2003).

34. T. Proffen, S. J. L. Billenge, *Journal of Applied Crystallography* **32**, 572 (1999).

35. S. J. L. Billinge, V. Petkov, T. Proffen, *Commission on Powder Diffraction of the International Union of Crystallography Newsletter* (2000).

36. B. D. Hall, D. Zanchet, D. Ugarte, *Journal of Applied Crystallography* **33**, 1335 (2000).

37. R. B. Neder, V. I. Korsunskiy, *Journal of Physics-Condensed Matter* **17**, S125 (2005).

38. K. Page *et al.*, *Chemical Physics Letters* **393**, 385 (2004).

39. S. W. Provencher, *Computer Physics Communications* **27**, 213 (1982).

40. I. D. Morrison, E. F. Grabowski, C. A. Herb, *Langmuir* **1**, 496 (1985).

41. G. A. Waychunas, in *Nanoparticles and the Environment* J. F. Banfield, A. Navrotsky, Eds. (The Mineralogical Society of America, Washington, D.C., 2001), vol. 44, pp. 105-162.

42. B. Gilbert, F. Huang, Z. Hengzhong, G. A. Waychunas, J. F. Banfield, *Science* **305**, 651 (2004).

43. F. M. Michel *et al.*, *Chemistry of Materials* **17**, 6246 (2005).

44. H. M. Rietveld, *Journal of Applied Crystallography* **2**, 65 (1969).

45. H. P. Klug, L. E. Alexander, *X-ray Diffraction Procedures for Polycrystalline and Amorphous Materials* (Wiley Interscience, New York, ed. 2nd, 1974), pp. 992.

46. S. J. L. Billinge, M. G. Kanatzidis, *Chemical Communications* **7**, 749 (2004).

47. T. Egami, S. J. L. Billenge, *Underneath the Bragg Peaks: Structural Analysis of Complex Materials*. R. W. Cahn, Ed., Pergamon Materials Series (Elsevier, Oxford, 2003), pp. 404.

48. L. Manna, E. C. Scher, A. P. Alivisatos, *Journal of the American Chemical Society* **122**, 12700 (2000).

49. J. Hu *et al.*, *Journal of American Chemical Society* **125**, 11306 (2003).

50. Y. Ding, Z. L. Wang, *Journal of Physical Chemistry B* **108**, 12280 (2004).

51. M. Wolthers, Ph.D. dissertation (2003).

52. J. Bebié, M. A. A. Schoonen, D. R. Strongin, M. Fuhrmann, *Geochimica et Cosmochimica Acta* **62**, 633 (1998).

53. G. C. Ulmer, H. L. Barnes, *Hydrothermal Experimental Techniques* (John Wiley & Sons, Inc., New York, 1987), pp. 523.

54. X. V. Zhang *et al.*, *Journal of Photochemistry and Photobiology a-Chemistry* **185**, 301 (2007).

Chapter 5: Similarities in 2- and 6-Line Ferrihydrite Based on Pair Distribution Function Analysis of X-ray Total Scattering

Reproduced with permission from Chemistry of Materials:

F. M. Michel [a,b], L. Ehm [a,b], G. Liu [a,c], W. Q. Han [f], S. M. Antao [h], P. J. Chupas [h], P. L. Lee [h], K. Knorr [e], H. Eulert [e], J. Kim [a,d], C. P. Grey [a,d], A. J. Celestian [a,b], J. Gillow [a,g], M. A. A. Schoonen [a,b], D. Strongin [a,c], J. B. Parise [a,b,d] (2007) Similarities in 2- and 6-Line Ferrihydrite Based on Pair Distribution Function Analysis of the X-ray Total Scattering, Chem. Mater., 19, 1489-1496. doi: 10.1021/cm062585n.

[a] *Center for Environmental Molecular Science (CEMS)*
[b] *Department of Geosciences, Stony Brook University, Stony Brook, New York 11794*
[c] *Department of Chemistry, Temple University, Philadelphia, Pennsylvania 19122*
[d] *Department of Chemistry, Stony Brook University, Stony Brook, New York 11794*
[e] *Christian-Albrechts-Universitaet zu Kiel, Institut fuer Geowissenschaften, Kiel, Germany, 24098*
[f] *Center for Functional Nanomaterials, Brookhaven National Laboratory, Upton, New York 11973*
[g] *Environmental Sciences Department, Brookhaven National Laboratory, Upton, New York 11973*
[h] *Advanced Photon Source, Argonne National Laboratory, Argonne, Illinois 60439*

Abstract

Iron(III) hydroxides are abundant in near-surface natural environments and play an important role in geochemical processes and the fate of contaminants. The issue of the structure of the common nanophase material ferrihydrite (ferric hydroxide) is controversial and has been debated in the literature for many years without definitive resolution. At least two types of ferrihydrite, the 2-line and 6-line forms, are conventionally recognized. It has been suggested that these forms possess different structures built up by different mixtures of distinct nanophase components. However, traditional crystallographic methods provide depictions of structure that are most sensitive either to short-range order (X-ray absorption) or long-range periodicity (X-ray diffraction or electron diffraction). We used high-energy X-ray total scattering for pair

distribution function analysis to observe both the short- and intermediate-range ordering (exceeding ~15 Å) of synthetic ferrihydrite with three distinct average domain sizes of 2, 3 and 6 nm. We show that there are no significant differences in the underlying structures of these materials, and that the differences in the diffraction patterns can be entirely interpreted by variations in the average size of the coherent scattering domains. The average crystallite sizes inferred from the PDF analysis are in good agreement with direct observation by high-resolution transmission electron microscopy.

Introduction

Ferric hydroxides are important mineral components and the subject of much scientific research in environmental and soil sciences due to their ubiquity in soils, groundwater and aquatic sediments (*1-3*). The oxidation and dissolution through weathering of Fe-bearing sulfide minerals associated with ore deposits and mining activities consequently results in the formation of secondary iron oxides, including ferrihydrite. Its large surface area and high reactivity results in a large adsorptive capacity for toxic contaminants such as U, As, Cd, and Pb (*4*). Accordingly, ferrihydrite has been important in metallurgical processing and used as an absorbent to remove contaminants from waste waters (*5*). Ferrihydrite has also been observed in meteorites and its presence on Mars may have important implications for understanding the magnetic properties of its soils (*6, 7*).

Ferrihydrite, otherwise commonly referred to as amorphous iron hydroxide, protoferrihydrite, and colloidal or hydrous ferric hydroxide, has long been described as poorly crystalline, disordered and X-ray amorphous (*8-10*). Evidence from direct imaging using electron microscopy (*11*), atomic force microscopy (AFM), and scanning tunneling microscopy (STM) (*12*) indicates that ferrihydrite is a nanocrystalline material. The number of broadened maxima in individual powder X-ray diffraction (XRD) patterns obtained with conventional X-ray sources is customarily used to designate the material as "2-line" or "6-line" ferrihydrite. The most widely reported nominal formula for ferrihydrite is $5Fe_2O_3{\cdot}9H_2O$ (*13*) although a number of other similar formulae (e.g., $Fe_5HO_8{\cdot}4H_2O$, $Fe(OH)_3$, $Fe_2O_3{\cdot}2FeOOH{\cdot}26H_2O$) have also been proposed (*10, 14, 15*).

Despite the numerous studies of this material using a variety of techniques, the structure of ferrihydrite has not yet been solved (*4*). The poorly delineated diffraction features have inhibited the use of traditional techniques of structural analysis resulting in ongoing debate regarding its atomic structure (*11, 16-18*). There is presently disagreement on whether 2- and 6-line ferrihydrite are best described by a single (defective) phase or by mixtures of phases. Moreover, no consensus has been reached on whether these two materials differ only in domain size or also exhibit distinct structural differences. Contemporary models are based on a variety of studies conducted using extended X-ray absorption fine structure (EXAFS), wide-angle and anomalous X-ray scattering, neutron diffraction (*17*) and electron nanodiffraction (*16, 19*). Two recent electron diffraction studies by Janney *et al.* (*16, 19*) have proposed different multi-phase structures models for 2- and 6-line ferrihydrite. However, several studies (*20-22*) now support the notion that the primary difference between the least and most crystalline forms of ferrihydrite (i.e., 2- and 6-line, respectively) is the size of the coherent scattering domains. In one such study, Guyodo et al. (*21*) concluded, using EXAFS analysis of samples with average particle sizes ranging from 3 to 5.4 nm, that the local environment of Fe in these samples is identical. Here we present results from synchrotron-based X-ray total scattering experiments which indicate that both the short- *and* intermediate-range ordering in nanocrystalline ferrihydrite are essentially the same and independent of changes in particle size. We believe that our results represent an important step in quantifying the terms of the so-called 2- and 6-line forms and significantly advance our understanding of the atomic arrangements in nanocrystalline ferrihydrite; this will lead to a better understanding its structure, reactivity, and other interesting properties.

Experimental

Ferrihydrite nanoparticles with three different average domain sizes (2, 3, and 6 nm) were prepared using different non-biological routes that are briefly described. The samples included in the present study will not be referred to by the nomenclature traditionally used to describe the number of diffraction maxima (e.g., 2-, 3-, 6-line, etc.). The term “ferrihydrite” (or abbreviated “Fhyd”) will hereinafter be followed by the estimated average coherent scattering domain size (e.g., Fhyd2, Fhyd3, or Fhyd6) when describing the least and most crystalline forms of ferrihydrite, respectively. To evaluate the potential for sample variation resulting from differences in synthesis conditions, our study also included analysis of three samples of 2 nm ferrihydrite made by independent groups at BNL, Temple, and Stony Brook University with all using the same general preparation method discussed below.

Fhyd2 and Fhyd6 were synthesized by Gang Liu at Temple University using a method developed by Schwertmann and Cornell (*13*). For sample Fhyd2 a 1 M solution of NaOH (Sigma-Aldrich) was added at a rate of 2 mL/min to a 0.2 M solution of $Fe(NO_3)_3 \cdot 9H_2O$ (Sigma-Aldrich) with constant stirring until the pH reached 7.5. The solution was repeatedly washed with deionized water (DI) (18 MΩ·cm in resistivity) and centrifuged to remove remaining electrolytes. Here we use centrifuging and drying naturally in a hood (both conducted at Temple) because previous studies show that processing ferrihydrite nanoparticles by freeze-drying leads to the formation of more crystalline 3-line ferrihydrite nanoparticles and goethite (*23*). Sample Fhyd3 was also synthesized by Gang Liu using a method adapted from Anschutz and Penn (*24*) in which 1.0 L of 0.48 M $NaHCO_3$ (Fischer, ACS grade) was added dropwise at a rate of 4.58 mL/min to a continuously stirred 1.0 L solution of 0.40 M $Fe(NO_3)_3 \cdot 9H_2O$ to form a homogeneous dark brownish suspension. The resulting suspension was placed into 200 mL Nalgene bottles and microwaved until boiling occurred. During heating, the bottles were agitated by shaking every 40 s to achieve homogenous heating of the suspension. Immediately after heating, the suspension was rapidly cooled in an ice bath to room temperature. The suspension was subsequently dialyzed in DI for three days, with the water being changed several times daily. Finally, dry-samples were prepared by drying in air. The 6 nm ferrihydrite nanoparticles were synthesized by dissolving 20 g $Fe(NO_3)_3 \cdot 9H_2O$ into 2 L of DI at a temperature of 75 ºC, with rapid stirring for 10-12 min to form a homogeneous dark reddish suspension. The suspension was rapidly cooled inside an ice bath to room temperature and dialyzed in DI for at least seven days, with the water being changed several times daily. Finally, the suspension was freeze-dried. Additional samples of ferrihydrite were synthesized by Jeff Gillow and Jonsik Kim using the same general preparation method used to form Fhyd2. All chemicals were used as received and without additional purification.

Characterization of ferrihydrite was carried out in part by the collection of high energy X-ray total scattering data coupled with pair distribution function analysis (PDF). Finely powdered dry samples were loaded into 1 mm polyimide (Kapton®) capillaries. A portion of each powdered sample was also re-dispersed in DI and subsequently loaded into 3 mm polyimide capillaries for analysis in an aqueous medium. Scattering data were collected at the 11-ID-B (*25*) (~90.3 keV, λ = 0.1372(2) Å) and 1-ID-C (*26*) (~100.1 keV, λ = 0.1238(6) Å) beamlines of the Advanced Photon Source (APS). The diffraction data were collected at ambient temperature on either a MAR345 image plate detector system or an Angio detector, an amorphous-Si detector manufactured by General Electric. To obtain properly normalized experimental PDFs, diffraction data were collected on both the samples and blanks over a wide *Q*-range (maximum of ~30 Å^{-1}). The independent measurement of the true background intensity by the collection of a blank allows for the direct subtraction of the parasitic scatter (e.g., capillary, aqueous medium (if present)). Equal exposure times were used for each sample and blank. Two blanks were necessary for properly removing background associated with the container (capillary) and water (for the samples re-dispersed in aqueous solution only). A CeO_2 standard (NIST diffraction intensity standard set: 674a) was used to calibrate the sample-to-detector distance and the tilt of the detector relative to the incident beam. The conversion of data from 2-D to 1-D was performed using the program Fit2D (*27, 28*) and a polarization correction was applied during integration of the data. The sample-to-detector distance was increased to improve resolution in the low-*Q* region for certain data collected at 11-ID-B. Details regarding the experimental setup at each beamline and for each sample are included in **Table 1**.

The total scattering structure function, $S(Q)$, and PDF ($G(r)$), were obtained using PDFgetX2 (*29*) where standard corrections were applied as well as those unique to the image-plate geometry (*30*). The Fourier transform of the normalized and weighted $S(Q)$, or $Q[S(Q)-1]$, results in the PDF, or $G(r)$, which corresponds to real space interatomic distances. The positions of the first three correlations in each PDF were determined from profile fitting with a linear combination of Gaussian and Lorentzian profiles using the program WinPLOTR (*31*). The PDF method differs from traditional techniques of X-ray diffraction (e.g., Rietveld) in that it directly yields information on the local, intermediate

Table 1. Experimental Details

Sample ID	Beamline	λ (Å)	Sample-Detector Distance (mm)	Detector Type	*Maximum* *Q*-Range ($Å^{-1}$)
Fhyd2, 3, & 6	1-ID-C	0.1238(6)	259.8	*a*-Si	23.0 - 25.0
	11-ID-B	0.1370(2)	207.9	*a*-Si	~29.5
	11-ID-B	0.1372(2)	745.5	Mar345	10.1

The reported maximum *Q*-range corresponds to the range of data incorporated in the transformation of *S*(*Q*) to the resulting PDF. The data collected at 11-ID-B using a larger sample-detector distance were not collected for PDF analysis.

and long-range (if present) structure. The PDF method also provides a useful tool for understanding the average scattering domain size of nanocrystalline materials through an evaluation of PDF attenuation (*32-37*). In brief, the exponential decay of the PDF can be attributed to a limited range of structural coherence if within the resolution of the instrument, as usually determined by a crystalline standard (e.g., CeO_2). In the case of highly crystalline samples, the exponential decay is primarily an indication of the resolution of the instrument (*37*) or instrument envelope. The resolution for these two beamlines was determined previously using CeO_2 and included in earlier communications (*34, 35*). The presence of structural disorder (e.g., static disorder and/or strain) at the surface or the interior of a nanocrystalline material can also effect the attenuation of the PDF and thereby result in an underestimate of the average crystallite size through the range of structural coherence. Therefore, the extrapolation of average crystallite size based on the range of structural coherence in the PDF should be considered as a minimum value. This aspect of the PDF has been reviewed elsewhere (*36*) and was demonstrated in the case of nanocrystalline ZnS (*38*). Therefore, the use of a separate technique, such as direct imaging by electron microscopy, is often necessary to corroborate the size estimates from PDF.

High-resolution transmission electron microscopy (HRTEM) was performed by W. Q. Han at Brookhaven National Laboratory (BNL) using a 300 kV JEOL-3000FEG microscope equipped with an energy-dispersive X-ray spectrometer. Fast Fourier Transform (FFT) diffraction patterns were taken from the whole areas of selected images. To prepare the TEM samples, first, ferrihydrite as a dry powder was re-dispersed into DI water and sonicated in an ice bath to form a homogeneous suspension, and also prevent any phase transformation to a more stable phase such as goethite or hematite. Second, a drop of the ferrihydrite suspension was placed onto an amorphous holey-carbon film supported by a standard TEM Cu grid (Ted Pella, Inc.). The excess suspension on the TEM grid was removed by absorbing the fluid with filter paper and the samples were allowed to dry at ambient conditions.

Thermogravimetric analysis (TGA) was performed by K. Knorr and H. Eulert at Christian-Albrechts-Universitaet using a Shimadzu DTG-60H apparatus. Weight loss was determined on <30 mg of each sample loaded in an open Pt pan. Heating was carried out at a rate of 10 K/min from ambient to 1073/1273 K under flowing dry N_2.

Results

The initial identification of synthetic ferrihydrite was performed using the low 2-theta region of XRD patterns (**Figure 1**). The resolution was improved in these patterns by increasing the sample-to-detector distance to ~50 cm at the 11-ID-B beamline. The patterns included in **Figure 1** for Fhyd2 and Fhyd6 illustrate how the number of peaks in individual diffraction patterns is customarily used to designate the material as "2-line" or "6-line" ferrihydrite, respectively. The broadened features corresponding to *d*-spacing values of 0.26, ~0.20, and 0.15 nm are indicative of those reported in prior studies of ferrihydrite (*4*). Due to peak broadening caused by nanocrystalline particle sizes and resulting in diminished intensity and increased overlap, the features in the pattern for Fhyd2 are less pronounced and some peaks nearly unrecognizable compared to those of Fhyd6. However, comparison of the diffraction patterns for all three samples reveals the presence of essentially all the same diffraction maxima.

High-Resolution Transmission Electron Microscopy (HRTEM):

The results of HRTEM imaging for the three samples indicate that the average crystallite size ranges from 2 - 3 nm (Fhyd2) up to 5 - 7 nm (Fhyd6). The representative images (**Figures 2 – 4**) show that each sample consists of a relatively monodisperse population of nanocrystalline particles. Lattice fringes are subtle and not easily resolved (**Figure 2)** in part because these particles are extremely small and show similar contrast to the amorphous holey-carbon support film. The FFT diffraction pattern (**Figure 2 – Inset**) of the entire image shows distinct diffraction rings at 0.26, 0.21, and 0.15 nm. **Figure 3** shows the representative image of sample Fhyd3 which was formed using the synthesis method for ~4 nm nanoparticles. In contrast to Fhyd2, lattice fringes are more clearly visible, indicating a higher degree of crystallinity with most particles on the order of 3 - 4 nm in diameter. Sample Fhyd6 (**Figure 4**) shows the highest degree of

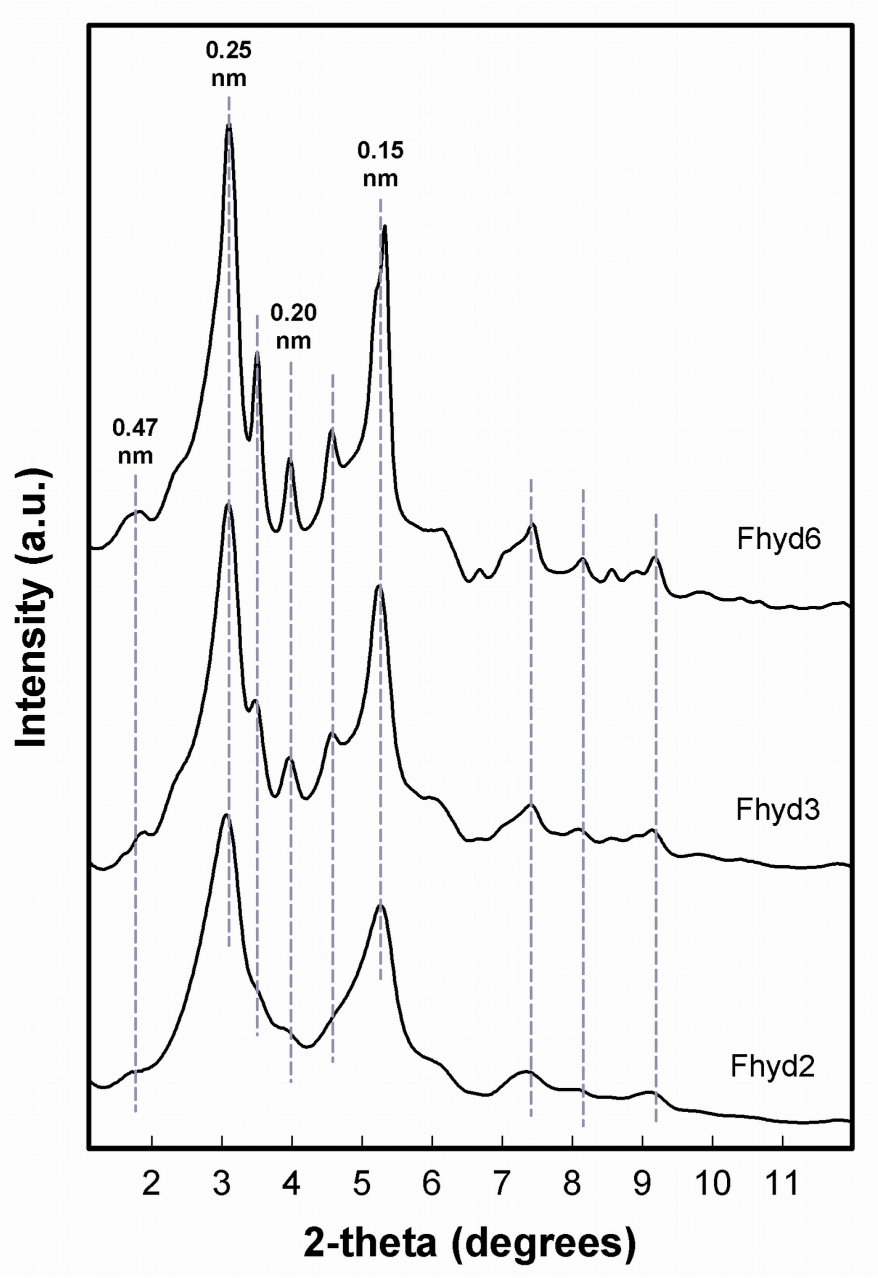

Figure 1: Background-subtracted diffraction data with intensity plotted in arbitrary units on the ordinate versus 2-theta in degrees on the abscissa. The patterns from top to bottom are for 6, 3, and 2 nm ferrihydrite, respectively. The features in the pattern for Fhyd2 are relatively broadened and overlapping, although all of the diffraction maxima are the same, as indicated by the vertical dotted lines. The *d*-spacings for several of the commonly referenced maxima are indicated in nm.

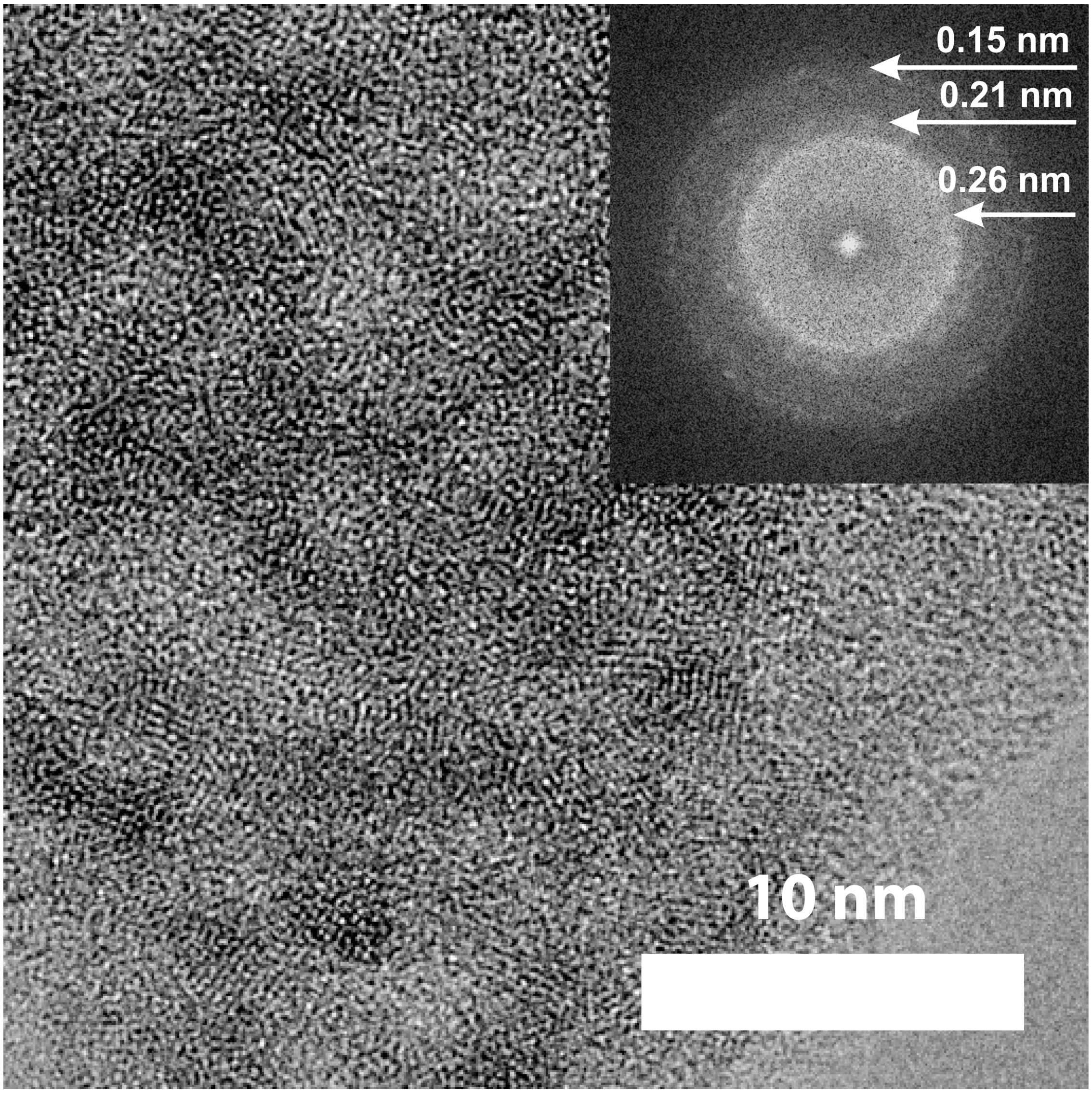

Figure 2: High-resolution transmission electron micrograph of Fhyd2. Individual particles appear to be on the order of 2 – 3 nm in diameter. Lattice fringes are present but difficult to discern due to lack of contrast relative to support film on the TEM grid. The Fast Fourier Transform diffraction pattern taken from the whole area of the image is included as an inset. The calculated *d*-spacings for the most prominent diffraction rings are indicated.

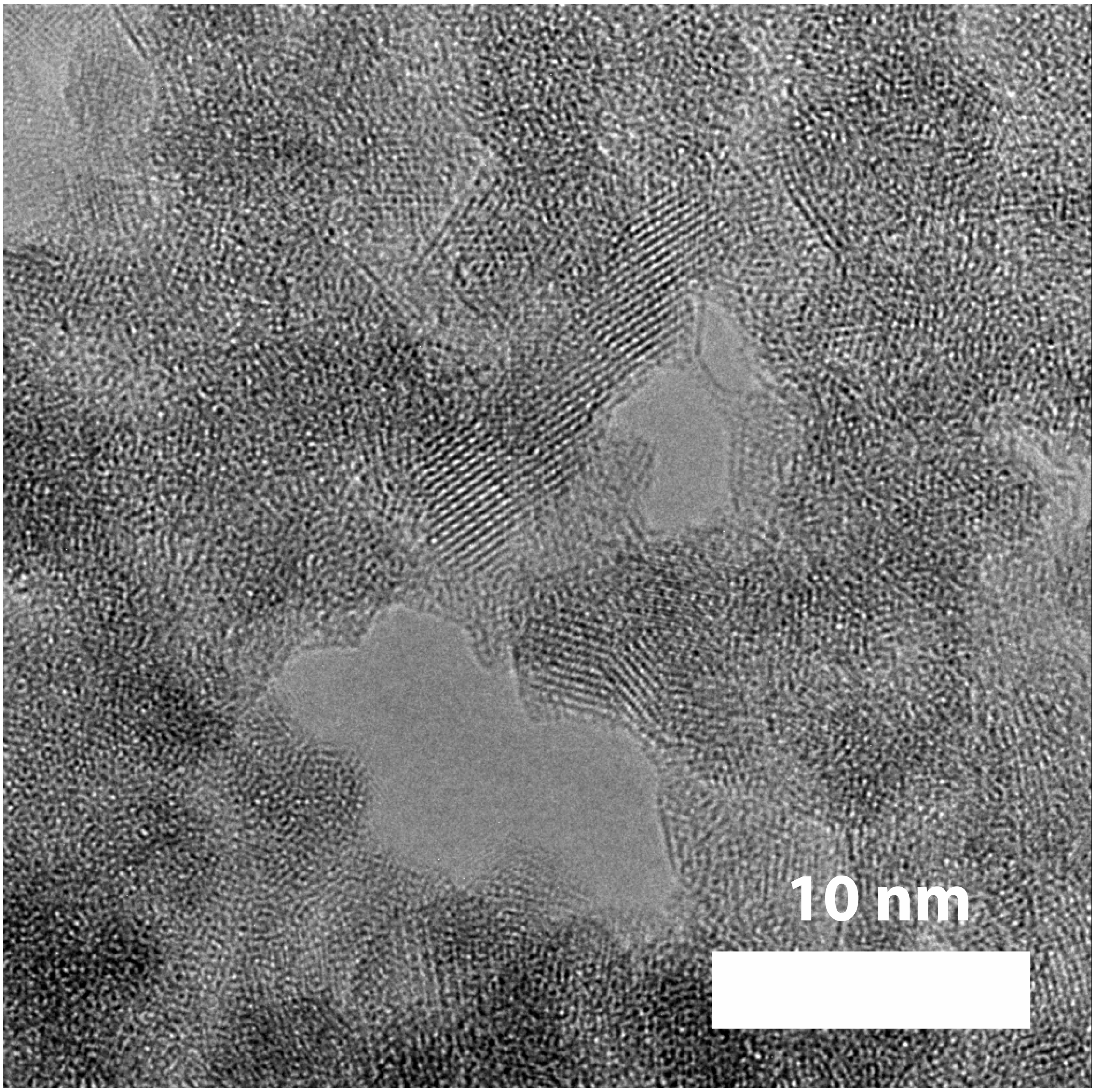

Figure 3: High-resolution transmission electron micrograph of Fhyd3. The particles appear to be on the order of 3 - 4 nm in diameter and show a higher degree of crystallinity than sample Fhyd2. The particles also appear to be in preferred-orientation on the TEM grid suggesting a plate-like morphology.

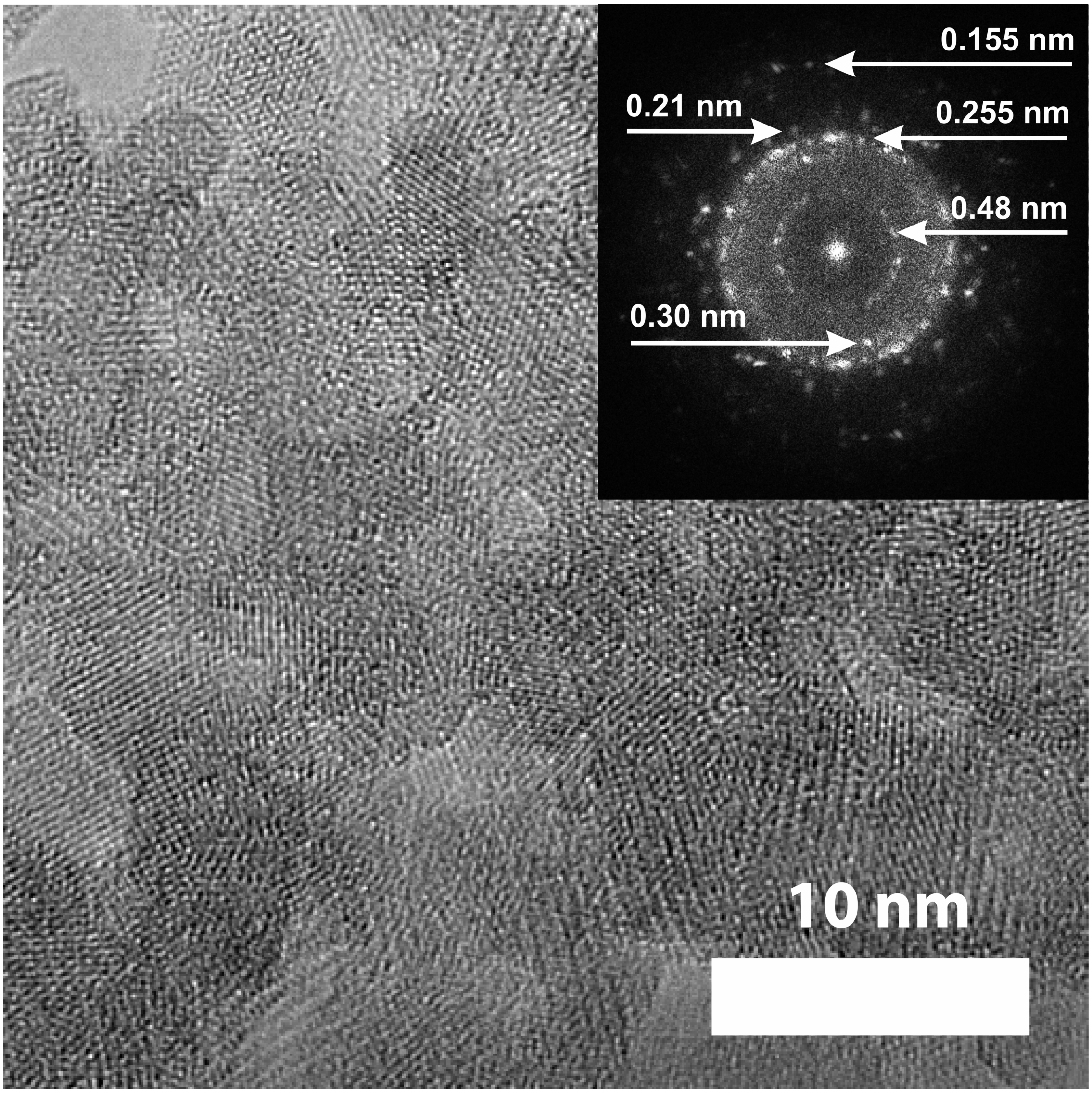

Figure 4: High-resolution transmission electron micrograph of Fhyd6. The particles show a higher degree of crystallinity than both Fhyd2 and Fhyd3 with average particle sizes of 5 – 7 nm in diameter. The particles also appear to be in preferred-orientation on the TEM grid suggesting a plate-like morphology. The Fast Fourier Transform diffraction pattern taken from the whole area of the image is included as an inset. The calculated *d*-spacings for the most prominent diffraction spots are indicated.

crystallinity, as evidenced by the particle sizes on the order of 5 - 7 nm and resolvable lattice fringes. The FFT diffraction pattern (**Figure 4 – Inset**) of the entire image shows strong diffraction features at 0.48, 0.30, 0.255, 0.21, and 0.155 nm. The measured *d*-spacings in the FFT patterns for Fhyd2 and Fhyd6 show good agreement with those observed in X-ray total scattering diffraction data (**Figure 1**). The full morphology of the nanoparticles is not easily discernable from HRTEM imaging alone but it appears that the particles are in preferred-orientation on the TEM grids suggesting they are plate-like.

High-energy X-ray total scattering and pair distribution function analysis:

The nominal formula for ferrihydrite ($5Fe_2O_3{\cdot}nH_2O$) was used during the normalization of the data to obtain $S(Q)$ and the resulting PDFs. To emphasize the diffuse components at high Q-values the data are represented as $F(Q)$ or $Q[S(Q)-1]$ (**Figure 5**). The composition necessary for properly normalizing the data collected on powdered ferrihydrite precipitates was possible by adding small amounts of stoichiometric water (**Figure 5 – Inset Table**) to the formula $5Fe_2O_3{\cdot}1H_2O$. Without this addition the normalization of $S(Q)$ was only possible by subtracting additional background relative to the amount warranted based on the equal exposure times used for both the sample and blank. The properly normalized patterns in **Figure 5** again show obvious similarities in diffraction features even out in the region dominated by diffuse scattering between 15 and 30 $Å^{-1}$. The Fourier Transform of $S(Q)$ (~30 $Å^{-1}$ for the dry samples in the present study) yields the PDF or $G(r)$, which is a real space representation of the atomic ordering of the material (*39*). The resulting PDFs (**Figure 6**) confirm that the short and intermediate-range atomic ordering are nearly identical for the dry ferrihydrite

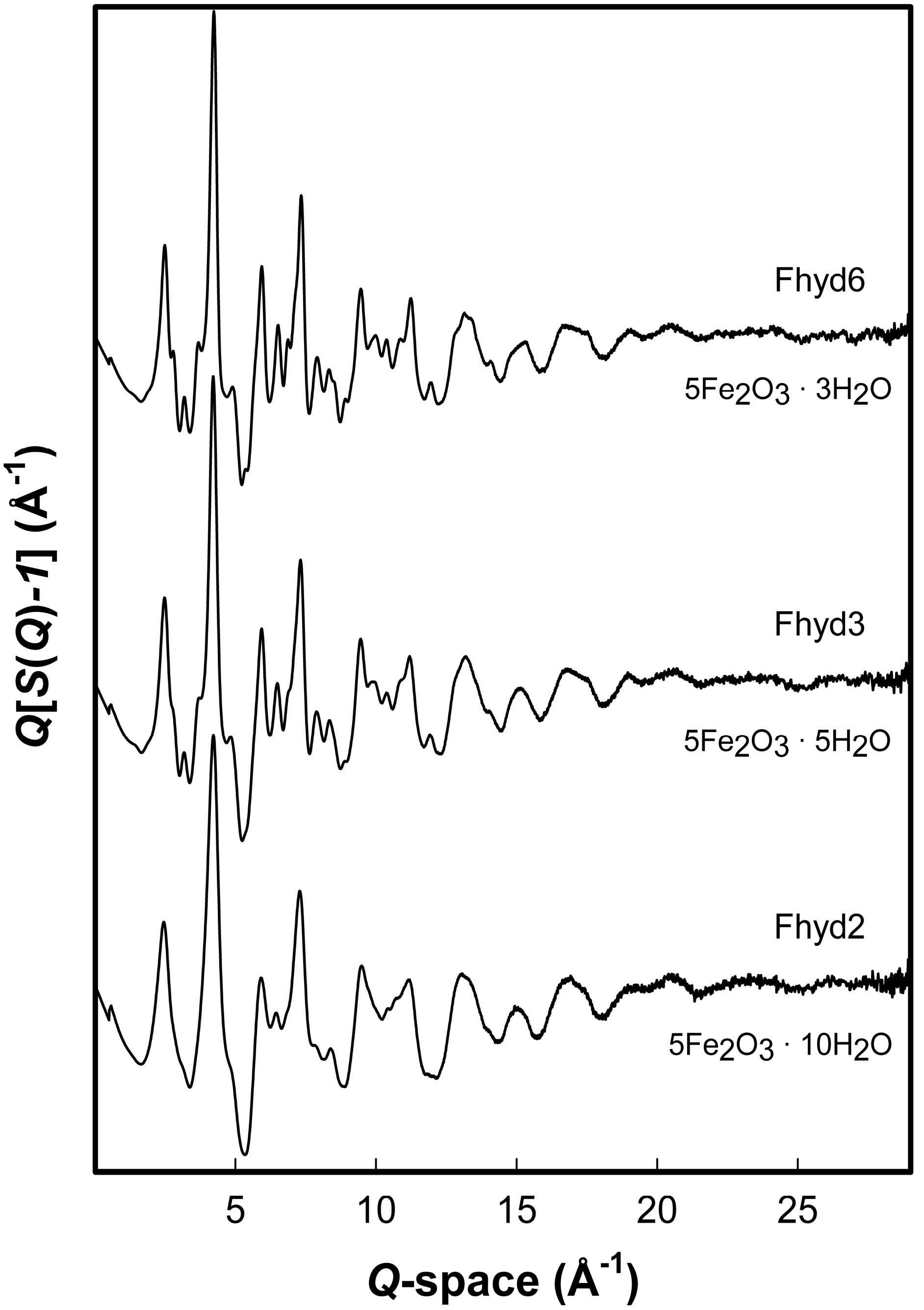

Figure 5: The weighted total scattering structure function $Q[S(Q)-1]$ properly normalized for ferrihydrite samples Fhyd2, Fhyd3, and Fhyd6 analyzed as dry powders. The three patterns show striking similarity in terms of the distances and occurrences of diffraction maxima.

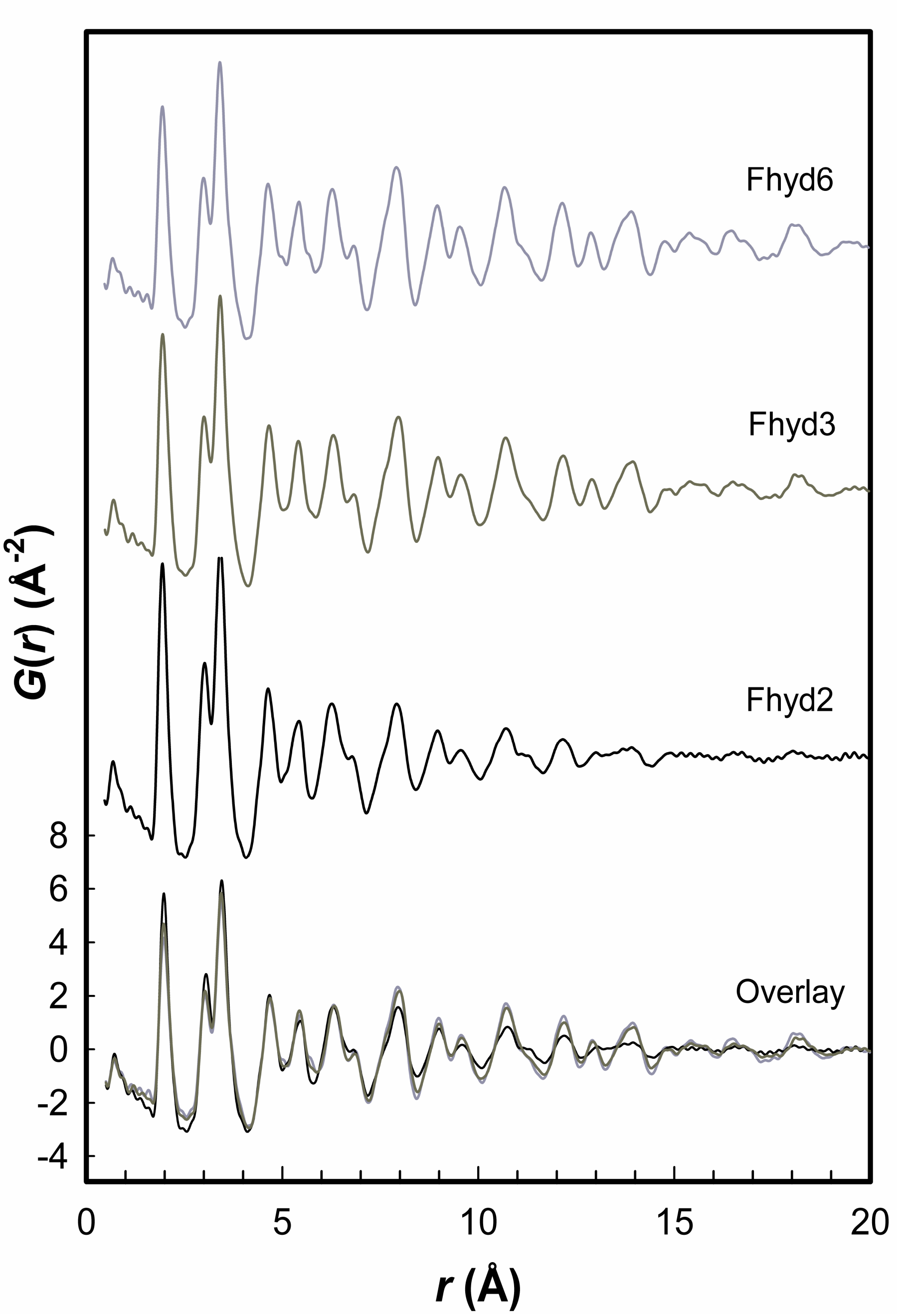

Figure 6: The PDF *G*(*r*) versus distance *r* is plotted for Fhyd2, Fhyd3, and Fhyd6 analyzed as dry powders. The PDFs are nearly identical over nearly 20 angstroms indicating that these samples share the same structural arrangement. Beyond approximately 7 angstroms the correlations for the 2 nm and 3 nm samples occur at the same distances but diminish more rapidly compared to those of the 6 nm sample. The bottom plot shows the overlay of the PDFs for the three samples.

precipitates examined. The PDFs for the same three precipitates analyzed in aqueous media (data not shown) are indistinguishable from those presented in **Figure 6**. As will be discussed, the PDF is not limited to the local ordering; it also provides atom pair correlations for all three samples beyond 15 Å and in certain cases can extend beyond 50 Å (**Figure 7**).

Thermogravimetric analysis:

TGA curves for Fhyd2, Fhyd3, and Fhyd6 show a relatively smooth weight loss, totaling 27.48%, 21.96%, and 15.57%, respectively (**Figure 8**). At temperatures ≤393 K, Fhyd2 lost ~17% by weight, or approximately 60% of its total weight loss. Fhyd3 and Fhyd6 lost ~11% and ~8% by weight, respectively, or approximately 50% of their total weight loss. The weight loss at lower temperatures (i.e. ≤393 K) is normally attributed to removal of surface adsorbed water. Based on the TGA measurements the stoichiometry for Fhyd2, Fhyd3, and Fhyd6 is $5Fe_2O_3 \cdot nH_2O$ with n equal to 10, 6, and 5, respectively. The TGA results presented here are generally consistent with previous studies (*15, 40*).

Discussion

The primary difference between the ferrihydrite precipitates formed by three different methods in this study is the size of the coherent scattering domains imposed by differences in average crystallite sizes. Until now, this idea has not been entirely appreciated since being initially suggested by Drits et al (1993) (*20*). The crystallinity of all the ferrihydrite precipitates examined in this study is relatively poor, in general, i.e., having broadened and weak XRD reflections (**Figure 1**). Also contributing to the

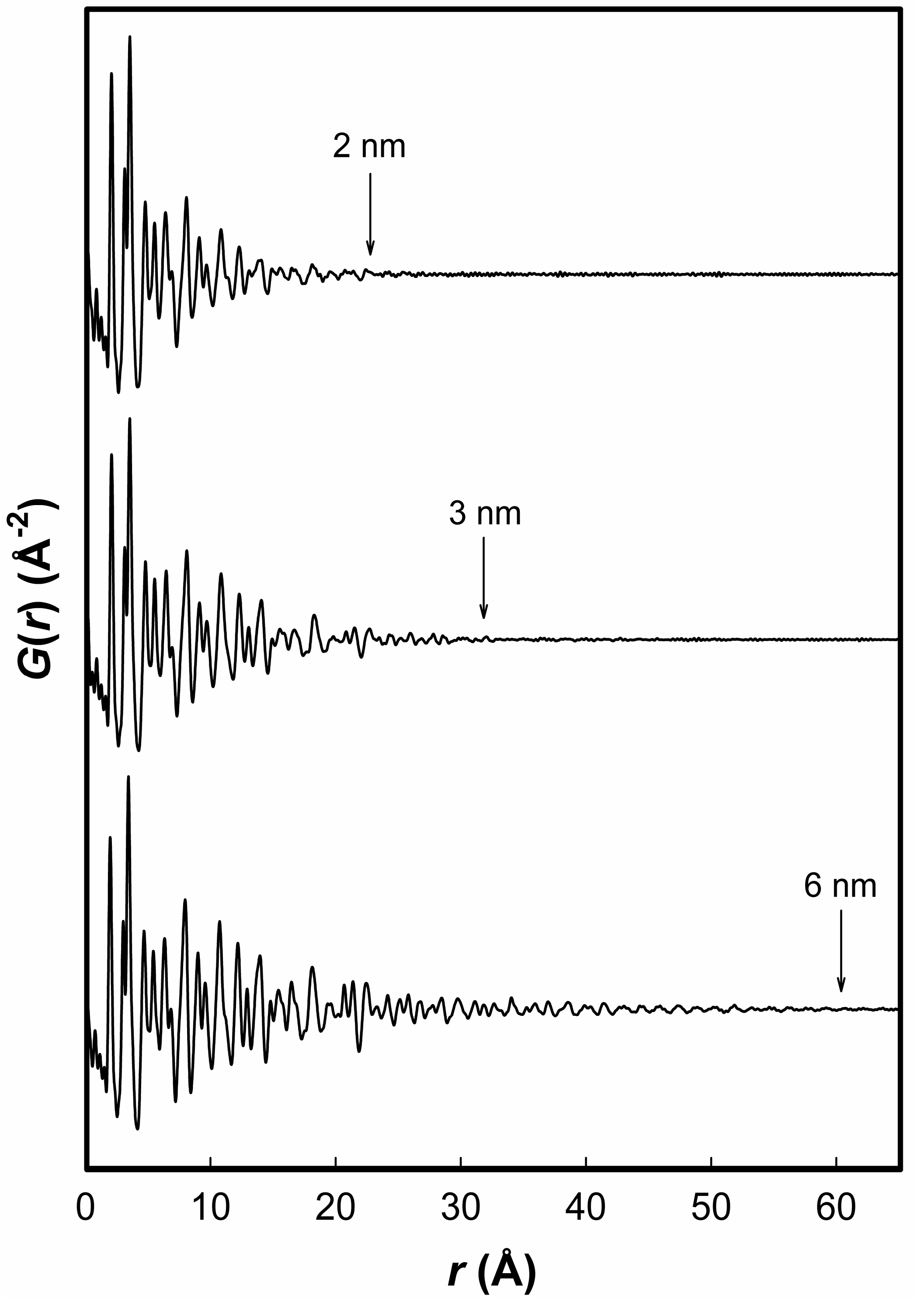

Figure 7: The PDF $G(r)$ plotted out to 65 Å to illustrate the degree of attenuation due to the range of structural coherence for Fhyd2 (top), Fhyd3, and Fhyd6 (bottom).

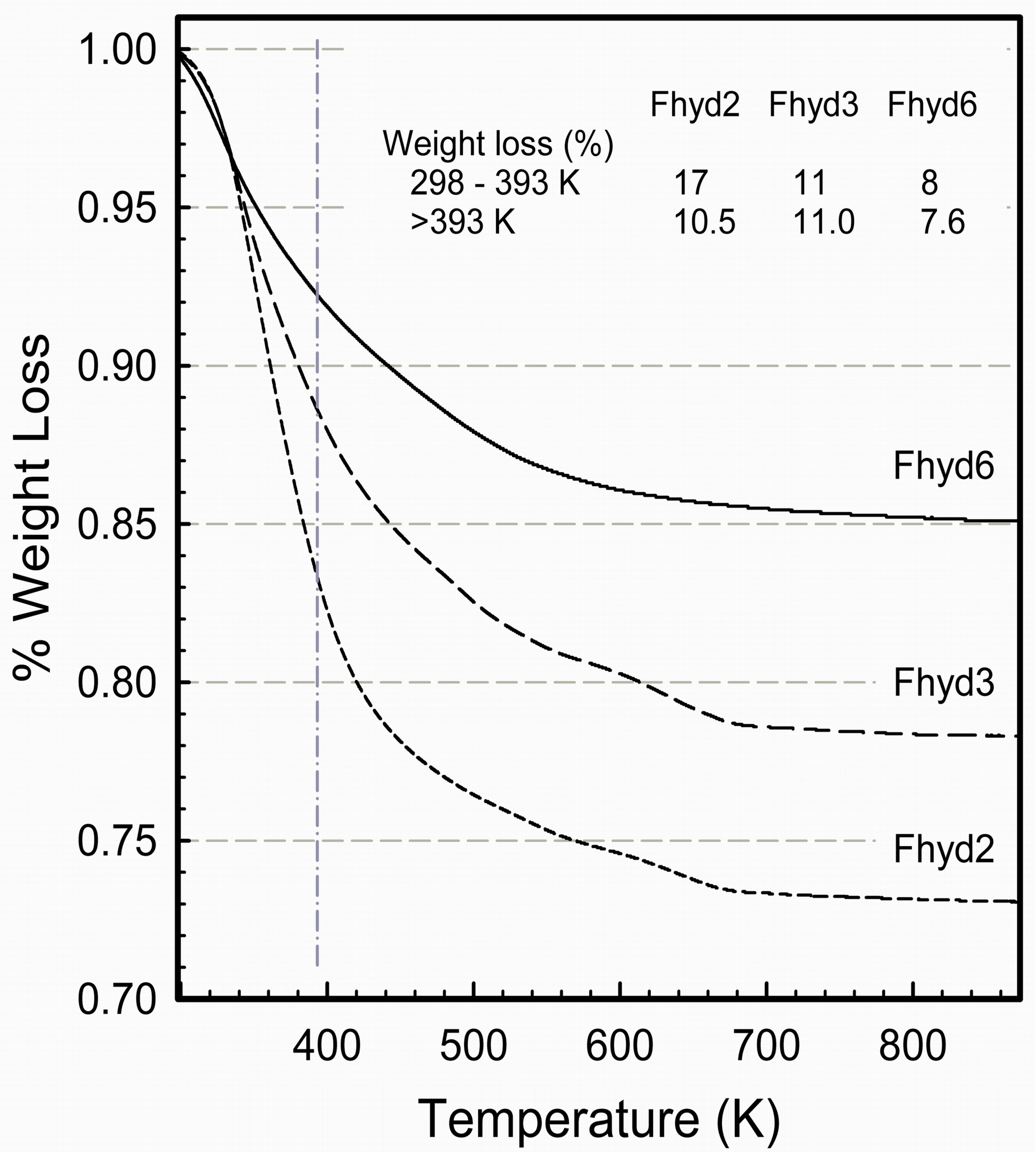

Figure 8: TGA results for samples Fhyd2, Fhyd3, and Fhyd6 showing percent weight loss as a function of temperature. The initial weight loss occurring between 298 and 393 K (See inset table) is primarily attributable to removal of surface adsorbed water.

broadening of maxima may be the effects of defects and disorder in the structure which are manifested as a diffuse scattering component. These characteristics may have hindered prior structural studies of nanocrystalline ferrihydrite using crystallographic techniques which rely on clearly defined Bragg peaks.

The PDFs for the precipitates show a significant degree of attenuation (**Figure 7**) due to limited coherent scattering domain sizes imposed by nanocrystalline particle sizes. The radial distance plotted along the abscissa is extended to 65 Å in **Figure 7** to emphasize the difference in attenuation between the three samples. It is apparent that Fhyd2 exhibits the shortest range of structural coherence and therefore consists of the smallest average coherent scattering domain. The correlations in the PDF for Fhyd2 attenuate at a distance of approximately 20 Å and the remainder of the pattern (>20 Å) reduces to statistical noise. The correlations in the PDF for Fhyd3 attenuate slightly further out at approximately 3.0 - 3.2 nm and those of Fhyd6 show the greatest range of structural coherence extending out beyond 50 Å. These results clearly are consistent with the increased broadening of diffraction features illustrated in **Figure 1** that occur with decreasing domain size. Direct imaging using HRTEM also indicates that Fhyd2, Fhyd3 and Fhyd6 differ in terms of average particle size and degree of crystallization (**Figures 2 – 4**). In the present study, as well as in other studies where ferrihydrite precipitates are imaged using HRTEM, the estimated average particle sizes reported are consistently slightly larger than what would be estimated based on PDF analysis alone. The discrepancy may be in part attributable to variability in samples formed in different laboratories. However, in the present study it is attributable to differences in what is fundamentally being measured by these techniques. In the case of HRTEM, the overall size of the visible particles are measured compared to PDF where the attenuation provides an indication of the average size of the coherent scattering domain. The PDF may not reflect atom pairs affected by surface relaxation and types of internal disorder which do not result in coherent scattering. In such cases the estimated average size using PDF attenuation is always likely to underestimate the true size of a particle. These results are consistent with prior estimates in studies by other researchers using HRTEM (*11, 21*), and with those obtained in recent work on the same precipitates using STM and AFM (*12*).

An evaluation of the pair correlations between 1 - 20 Å in the PDFs for Fhyd2, Fhyd3, and Fhyd6 reveals that all share the same atomic arrangement (**Figure 6)**. The positions from profile fitting of the first three correlations are included in **Table 2**. The first correlation at ~2.0 Å suggests that Fe and O are predominantly in an octahedral coordination (*41*). It has been suggested that tetrahedrally-coordinated Fe-O may also be present in 2-line ferrihydrite (*16*) or possibly occurring as the result of surface distortion resulting from the nanocrystalline particle sizes (*15, 42*). Evidence for this conjecture is not yet directly supported by PDF, but it should be noted that the difference in bond lengths in FeO_4 and FeO_6 polyhedra is only ~0.15 Å, for example as is found in the structure of maghemite (γ-Fe_2O_3) (*43*). Additionally, distortions in the FeO_6 polyhedra would result in Fe-O bond lengths deviating from an ideal geometry and result in a broader correlation in the PDF at ~2.0 Å. Such a distortion would also have the potential for obscuring the correlation corresponding to FeO_4 polyhedra, especially if the tetrahedrally-coordinated Fe were in relatively minor abundance (i.e., <25%). In this circumstance, the contribution of FeO_4 to this region of the PDF would likely be manifested as a subtle asymmetry of the left side of the FeO_6 correlation. Such asymmetry is not obvious in the PDFs presented here but cannot be ruled out for the reasons described above. The second and third correlations at 3.03 and 3.44 Å are characteristic of Fe-Fe distances for FeO_6 polyhedra linked in edge-sharing and corner sharing configurations, respectively. These distances and configurations are consistent with prior EXAFS work on ferrihydrite (*44*) and do not suggest the presence of polyhedra in the face-sharing configuration that has been suggested in prior work (*16, 17, 19*).

The main advantage to using high energy X-ray scattering and PDF analysis over spectroscopic techniques such as EXAFS for comparing ferrihydrite with different particle sizes, and ultimately comparing its structure, is that the PDF is not limited to information associated with the first three shells. As one recent study of nanocrystalline MnS demonstrated, multiple structural models may provide a satisfactory fit when considering only the short-range atomic order (< ~5 Å) (*35*). In the Fe-O-H system there are a number of potential structural models that have edge and corner sharing octahedra and thereby result in a very similar radial distribution function to ferrihydrite (e.g., goethite, akaganéite) out to ~5 Å (**Figure 9**). As shown in chapter 6, the PDF provides

Table 2. Peak-fitting of the PDF *G(r)*

Sample ID	**First Correlation**	**Second Correlation**	**Third Correlation**
	r (Å)	*r* (Å)	*r* (Å)
Fhyd2	1.98(0)	3.03(7)	3.44(3)
Fhyd3	1.97(9)	3.03(4)	3.44(2)
Fhyd6	1.98(3)	3.03(1)	3.44(1)

The positions from profile fitting of the first three correlations in each PDF for the dry ferrihydrite precipitates.

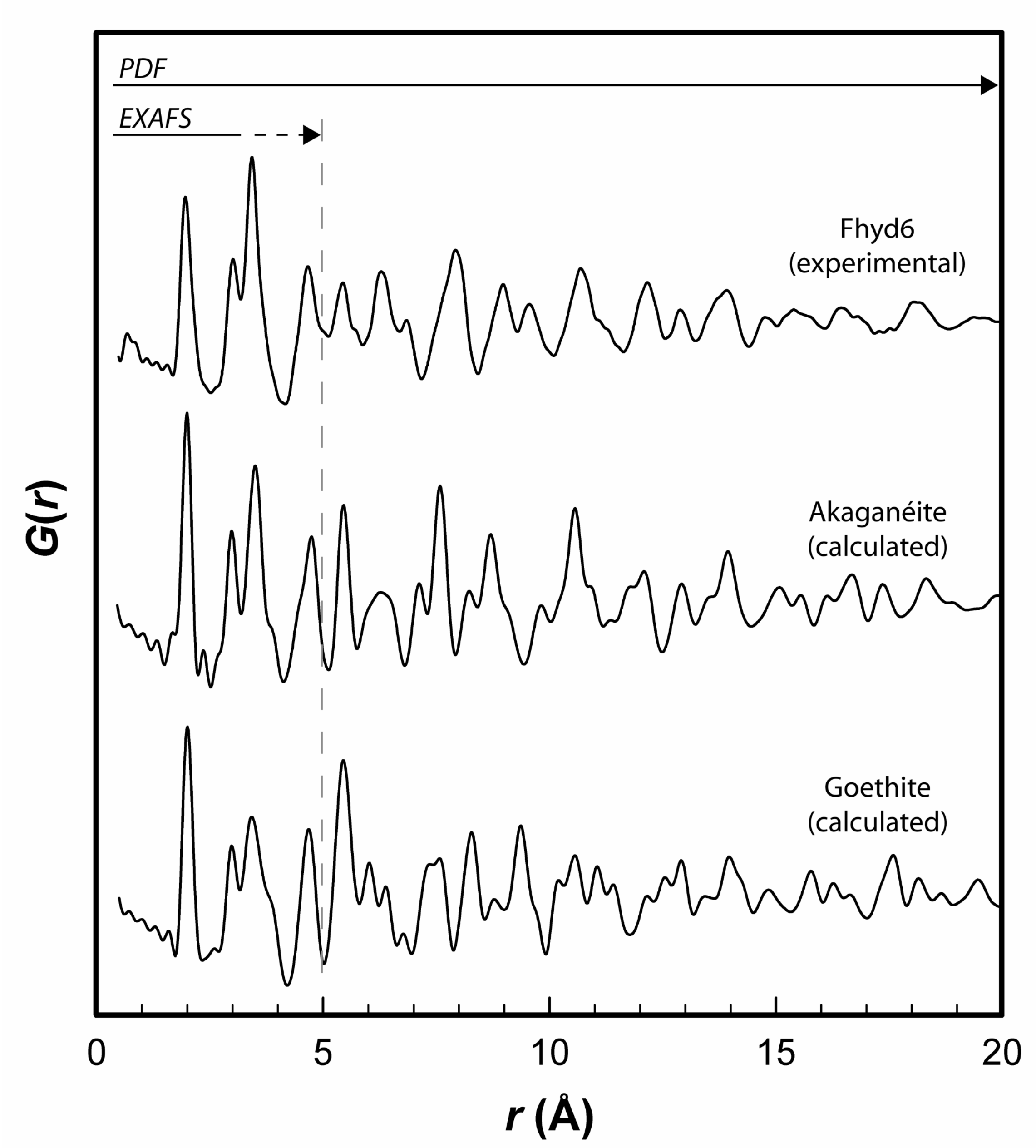

Figure 9: The experimental PDF $G(r)$ versus distance r is plotted for sample Fhyd6. Calculated PDFs for akaganéite and goethite are also plotted to show the similarities in the atom-atom distances over the first ~5 Å; typical of the range of distances reported by EXAFS. The PDF provides additional data which is essential for differentiating between competing structural models.

the invaluable additional information on the intermediate-range atomic ordering of ferrihydrite that allows for differentiation between competing structural models.

Variability in the quality of samples formed in separate laboratories using different starting materials and with subtle variations in synthesis conditions has been identified as a possible source of complexity and reason for disagreement between previous studies of structure and composition (*4*). Our study also included PDF analysis of three samples made by independent groups at BNL, Temple, and Stony Brook University with all using the same general preparation method (*13*). The PDFs for the three samples (**Figure 10**) were virtually identical suggesting no significant differences in structure or domain size. The potential structural changes in ferrihydrite caused by the interaction of the nanocrystalline solid-phase with aqueous solution were evaluated by also analyzing the precipitates (Fhyd2, Fhyd3, and Fhyd6) re-dispersed in aqueous solution. Again, no discernable changes for ferrihydrite nanoparticles in either state were observed in the resulting PDFs (also not shown). Although stoichiometric water was added as part of the normalization in both wet and dry samples, the abundance of structural water is still uncertain. Prior work has suggested that the presence of hydroxyl is essential for maintaining the ferrihydrite structure, (*45*) although this idea has also been disputed (*9, 10, 14*). Based on the formula used to normalize the data in the present study it is necessary to have only 1 water (2 protons) in the structure to charge-balance the Fe and O. TGA curves show a significant weight loss for each sample at temperatures ≤393 K (**Figure 8**) indicating removal of weakly bound surface adsorbed water. This evidence for the presence of variable amounts of surficial water provides support for the additional H_2O necessary during the PDF normalization procedure and is in good agreement with the stoichiometry estimated from TGA. Subsequent weight loss at temperatures >393 K indicates the loss of more strongly bound structural water and are not yet fully understood. We currently have experiments in progress using neutron scattering and PDF analysis on samples of ferrihydrite synthesized carefully with deuterium to minimize the incoherent scattering interference resulting from hydrogen contamination. This study will be essential for understanding the role of protons in the structure of ferrihydrite and will be a part of future communications.

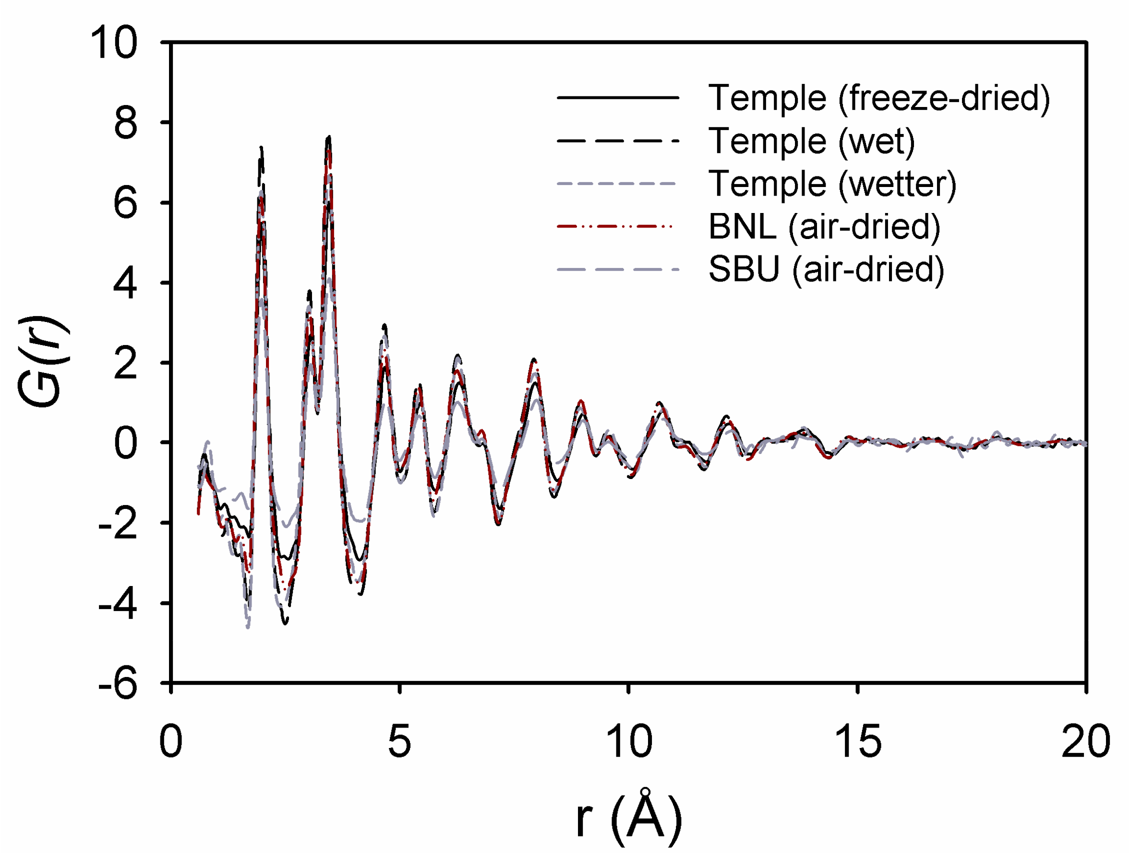

Figure 10: The PDF *G*(*r*) versus distance *r* is plotted for samples of 2 nm ferrihydrite formed in three independent laboratories. The PDFs are virtually identical over approximately 15 Å indicating that these samples share the same structural arrangement. The differences in intensity result from variations in the composition used during the normalization procedure. Specifically, the additional stoichiometric water added for the samples that were not intentionally dried (i.e., "wet" and "wetter") causes changes in the overall density and therefore differences in the resulting intensities.

Conclusions

With the development and application of advanced analytical and experimental techniques at synchrotron facilities and in the laboratory, we now have the tools to rigorously characterize fundamental atomic properties of traditionally challenging materials, such as nanocrystalline ferrihydrite. Based on PDF analysis of high energy X-ray total scattering data, the primary difference between so-called 2- and 6-line ferrihydrite is the limited size of the coherent scattering domains imposed by differences in average primary crystallite size, rather than a fundamental difference in atomic arrangement. A comparison of the PDFs for the samples with three distinct average particle sizes in this study indicates that all share the same atomic arrangement based on atom pair correlations extending beyond 15 Å. The average domain sizes of the precipitates examined in this study are estimated using the PDF method to be in the range of 2 - 6 nm and are supported by HRTEM. The local atomic arrangement from PDF analysis also does not show any significant changes when analyzed in powder form or when re-dispersed in aqueous media. Surface adsorbed water content varied with particle size, as indicated by both PDF analysis and TGA. The results presented here provide the foundation for quantitatively testing previously-proposed structural models for ferrihydrite and may also lead to the development of a new structural model which better describes this phase. These ideas will be explored in future communications.

References

1. D. G. Rancourt *et al.*, *American Mineralogist* **86**, 834 (2001).
2. U. Schwertmann, L. Carlson, E. Murad, *Clays and Clay Minerals* **35**, 297 (1987).
3. Y. Shaked, Y. Erel, A. Sukenik, *Geochimica et Cosmochimica Acta* **68**, 1439 (2004).
4. J. L. Jambor, J. E. Dutrizac, *Chemical Reviews* **98**, 2549 (1998).
5. J. A. Dyer, P. Trivedi, S. J. Sanders, N. C. Scrivner, D. L. Sparks, *Journal of Colloid and Interface Science* **270**, 66 (2004).
6. J. L. Bishop, C. M. Pieters, R. G. Burns, *Geochimica et Cosmochimica Acta* **57**, 4583 (1993).
7. R. V. Morris, D. C. Golden, J. F. Bell, H. V. Lauer, J. B. Adams, *Geochimica et Cosmochimica Acta* **57**, 4597 (1993).
8. K. C. Ivarson, M. Sojak, *Canadian Journal of Soil Science* **58**, 1 (1978).
9. U. Schwertmann, W. R. Fischer, *Geoderma* **10**, 237 (1973).
10. K. M. Towe, W. F. Bradley, *Journal of Colloid and Interface Science* **24**, 384 (1967).
11. D. E. Janney, J. M. Cowley, P. R. Buseck, *Clays and Clay Minerals* **48**, 111 (2000).
12. G. Liu *et al.*, *Langmuir* **22**, 9313 (2006).
13. U. Schwertmann, R. M. Cornell, *Iron Oxides in the Laboratory: Preparation and Characterization* (Wiley - VCH, Weinheim, ed. 1st, 2000), pp. 89-94.
14. F. V. Chukhrov, B. B. Zvyagin, A. I. Gorshkov, L. P. Yermilova, V. V. Balashove, *International Geology Review* **16**, 1131 (1973).
15. R. A. Eggleton, R. W. Fitzpatrick, *Clays and Clay Minerals* **36**, 111 (1988).
16. D. E. Janney, J. M. Cowley, P. R. Buseck, *American Mineralogist* **85**, 1180 (2000).
17. E. Jansen, A. Kyek, W. Schafer, U. Schwertmann, *Applied Physics A-Materials Science & Processing* **74**, S1004 (2002).

18. A. Manceau, V. A. Drits, *Clay Minerals* **28**, 165 (1993).

19. D. E. Janney, J. M. Cowley, P. R. Buseck, *American Mineralogist* **86**, 327 (2001).

20. V. A. Drits, B. A. Sakharov, A. L. Salyn, A. Manceau, *Clay Minerals* **28**, 185 (1993).

21. Y. Guyodo *et al.*, *Physics of the Earth and Planetary Interiors* **154**, 222 (2006).

22. R. K. Kukkadapu *et al.*, *American Mineralogist* **88**, 1903 (2003).

23. C. Greffie, M. Amouric, C. Parron, *Clay Minerals* **36**, 381 (2001).

24. A. J. Anschutz, R. L. Penn, *Geochemical Transactions* **6**, 60 (2005).

25. U. Rutt *et al.*, *Nuclear Instruments & Methods in Physics Research Section a-Accelerators Spectrometers Detectors and Associated Equipment* **467**, 1026 (2001).

26. S. D. Shastri *et al.*, *Journal of Synchrotron Radiation* **9**, 317 (2002).

27. "Fit2D" V. 9.129 Reference Manual V. 3.1.

28. A. P. Hammersley, S. O. Svenson, M. Hanfland, D. Hauserman, *High Pressure Research* **14**, 235 (1996).

29. X. Qiu, J. W. Thompson, S. J. L. Billinge, *Journal of Applied Crystallography* **37**, 110 (2004).

30. P. J. Chupas *et al.*, *Journal of Applied Crystallography* **36**, 1342 (2003).

31. T. Roisnel, J. Rodriguez-Carvajal, paper presented at the Materials Science Forum, Proceedings of the Seventh European Powder Diffraction Conference (EPDIC 7) 2000.

32. S. J. L. Billinge, V. Petkov, T. Proffen, *Commission on Powder Diffraction of the International Union of Crystallography Newsletter*, 21 (2000).

33. B. D. Hall, D. Zanchet, D. Ugarte, *Journal of Applied Crystallography* **33**, 1335 (2000).

34. F. M. Michel *et al.*, *Chemistry of Materials* **17**, 6246 (2005).

35. F. M. Michel, M. A. A. Schoonen, X. V. Zhang, S. T. Martin, J. B. Parise, *Chemistry of Materials* **18**, 1726 (2006).

36. R. B. Neder, V. I. Korsunskiy, *Journal of Physics-Condensed Matter* **17**, S125 (2005).

37. K. Page *et al.*, *Chemical Physics Letters* **393**, 385 (2004).

38. B. Gilbert, F. Huang, H. Z. Zhang, G. A. Waychunas, J. F. Banfield, *Science* **305**, 651 (2004).

39. H. P. Klug, L. E. Alexander, *X-ray Diffraction Procedures for Polycrystalline and Amorphous Materials* (Wiley Interscience, New York, ed. 2nd, 1974), pp. 992.

40. A. M. Saleh, A. A. Jones, *Clay Minerals* **19**, 745 (1984).

41. R. D. Shannon, *Acta Crystallographica Section A* **32**, 751 (1976).

42. J. Zhao *et al.*, *Journal of Catalysis* **143**, 499 (1993).

43. C. Greaves, *Journal of Solid State Chemistry* **49**, 325 (1983).

44. J. M. Combes, A. Manceau, G. Calas, *Geochimica et Cosmochimica Acta* **54**, 1083 (1990).

45. C. W. Childs, N. Kanasaki, N. Yoshinaga, *Applied Clay Science* **9**, 65 (1993).

Chapter 6: The Structure of Ferrihydrite, a Nanocrystalline Material

Published in Science:

F. Marc Michel [a,b], Lars Ehm [a,b], Sytle M. Antao [c], Peter L. Lee [c], Peter J. Chupas [c], Gang Liu [a,d], Daniel R. Strongin [a,d], Martin A. A. Schoonen [a,b], Brian L. Phillips [a,b], John B. Parise [a,b,e] (2007) The Structure of Ferrihydrite, a Nanocrystalline Material, Science, 316 (5832), 1726-1729, doi: 10.1126/science.1142525

[a] *Center for Environmental Molecular Science (CEMS)*
[b] *Department of Geosciences, Stony Brook University, Stony Brook, New York 11794F*
[c] *Advanced Photon Source, Argonne National Laboratory, Argonne, Illinois 60439*
[d] *Department of Chemistry, Temple University, Philadelphia, Pennsylvania 19122*
[e] *Department of Chemistry, Stony Brook University, Stony Brook, New York 11794*

Abstract

Despite the ubiquity of ferrihydrite in natural sediments and its importance as an industrial sorbent, the nanocrystallinity of this iron oxyhydroxide has hampered accurate structure determination by traditional methods which rely on long-range order. Here we uncover the atomic arrangement by real-space modeling of the pair distribution function (PDF) derived from direct Fourier transformation of the total x-ray scattering. The PDF for ferrihydrite synthesized using different routes is consistent with a single phase (hexagonal spacegroup $P6_3mc$; a = ~5.95, c = ~9.06 Angstroms). In its ideal form, this structure contains 20% tetrahedrally and 80% octahedrally coordinated iron and has a basic structural motif closely related to the Baker-Figgis δ-Keggin cluster. Real-space fitting indicates structural relaxation with decreasing particle size and also suggests that second-order effects such as internal strain, stacking faults and particle shape contribute to the PDFs.

Introduction

Ferrihydrite is ubiquitous in many near-surface environments (*1, 2*) and is routinely used in industrial applications such as in direct coal liquefaction and metallurgical processing (*3, 4*). It occurs in pristine soils and sediments as the precursor to hematite (*5*) and often in areas contaminated by acid mine drainage. Due to its extremely high surface area and reactivity, ferrihydrite plays a significant role in the sequestration of contaminants from groundwater and streams through adsorption and coprecipitation. As such, it is also manufactured for use as a scavenger of heavy metals and metalloids during the treatment of wastewaters and in remedial activities. It also forms the inorganic core of ferritin, an iron storage protein that plays a key role in controlling the levels of iron in plants, animals, and microbes (*6*).

Even with the considerable attention given to the chemical and physical properties of ferrihydrite in prior research, there is no consensus on the crystal structure of this mineral. The primary impediment to the development of a definitive structural determination is the size of individual ferrihydrite crystallites which are typically <10 nm (nanocrystalline). With regard to structure, most of the disagreement centers on the possible presence of multiple structural phases and the local environment of iron (*7-10*), and has implications for understanding its reactivity, magnetic properties, and overall chemical composition. No single formula is widely accepted for ferrihydrite and this is attributed to variable water content and a lack of a known crystal structure (*11*). Ferrihydrite is commonly designated as "2-line" or "6-line" on the basis of the number of poorly defined, broadened maxima observed in x-ray diffraction (XRD) patterns. Determining a starting structural model for this phase is particularly challenging because ferrihydrite has no known well-crystalline counterpart that can be synthesized in the laboratory or found in nature. We recently showed that the short- and intermediate-range ordering in synthetic nanocrystalline ferrihydrite is consistent for scattering domain sizes ranging from 2 to 6 nm, and therefore the structure of ferrihydrite appears to be single phase (*12*). This result contradicts some prior studies (*7-10*) and is fundamentally different from the current multi-phase structure model that is increasingly cited for this phase.

Experimental

Synthetic ferrihydrite with three distinct average coherent scattering domain sizes of approximately 2 (Fhyd2), 3 (Fhyd3), and 6 nm (Fhyd6) were synthesized by Gang Liu at Temple University and evaluated as part of this study. The samples were formed using different synthesis procedures (*13, 14*) involving the hydrolysis of Fe at varying temperatures and resulting in precipitates with distinct particle sizes. In brief, Fhyd2 was synthesized at room temperature (23 ºC) by adding a 1 M solution of NaOH (Sigma-Aldrich) at a rate of 2 mL/min to a 0.2 M solution of $Fe(NO_3)_3{\cdot}9H_2O$ (Sigma-Aldrich) with constant stirring until the pH reached 7.5. Fhyd3 was formed by the dropwise addition of 1.0 L of a 0.48 M $NaHCO_3$ (Fisher) solution at a rate of 4.58 mL/min to a continuously stirred 1.0 L solution of 0.4 M $Fe(NO_3)_3{\cdot}9H_2O$ to form a homogenous dark brown suspension. The resulting suspension was transferred into 200 mL Nalgene bottles and microwaved with agitation until boiling occurred. Sample Fhyd6 was synthesized by dissolving 20 g of $Fe(NO_3)_3{\cdot}9H_2O$ into 2 L of deionized water (DI) water maintained at a temperature of 75 ºC with rapid stirring for 10 to 12 min. A homogenous dark reddish suspension formed which was then rapidly cooled in an ice bath to room temperature. All of the resulting precipitates were repeatedly washed with DI using centrifugation or dialysis to remove remaining electrolytes before drying.

Direct imaging using high-resolution transmission electron microscopy (HRTEM) indicates that the three samples have average sizes of 2-3, 3-4 and 5-7 nm, respectively. The particles of Fhyd3 and Fhyd6 appear to be in preferred orientation on the TEM grids and have uniform thickness, suggesting a plate-like morphology. This interpretation is consistent with previous work (*14*) but may be incomplete because the HRTEM method produces a two dimensional representation of a three dimensional object. The coherent scattering domain sizes estimated from attenuation of the pair distribution functions (PDFs) are 2, 3, and 6 nm respectively; slightly smaller but consistent with the overall particles sizes estimated from HRTEM. The PDFs for the three samples are nearly identical in terms of the distribution of interatomic distances extending beyond ~15 Å suggesting strongly that their structure is virtually the same, and by implication, single phase (*12*).

High energy x-ray total scattering data were collected from powders of the three ferrihydrite precipitates at the 11-ID-B beamline (*15*) at the Advanced Photon Source at Argonne National Laboratories. The incident radiation was ~90 keV (λ = 0.1370(2) Å) and the scattered beam was collected on an Angio detector, an amorphous-Si detector manufactured by General Electric. The conversion of data from 2D to 1D was performed using the program Fit2D (*16, 17*). The PDFs were obtained by the Fourier Transform using PDFgetX2, (*18*) of the total scattering structure function *S(Q)* collected to a resolution of approximately 30 $Å^{-1}$; standard methods were applied as well as those unique to image-plate geometry (*19*) and are described in the initial part of this investigation (*12*). The experimental PDFs are refined using the program PDFFIT (*20*) and each refinement includes initial atomic coordinates, cell parameters, isotropic displacement parameters (*U*), and symmetry constraints based on spacegroup $P6_3mc$. These parameters are refined in the following order: 1) scale, resolution dampening (σ_Q); 2) lattice parameters; 3) atom positions; 4) isotropic-displacement parameters and a unit less peak sharpening factor (δ); 5) occupancy of Fe. A "goodness of fit" indicator for each refinement is expressed as a weighted residual value (R_w) and is included in this table. Two additional parameters δ and σ_Q were incorporated in each refinement to model sharpening of near neighbor peaks due to correlated motion between atom pairs and the exponential decay of the PDF, respectively.

Results & Discussion

Structural analysis using the PDF method involves a comparison between PDFs generated from the experimental scattering data and those calculated from structural models (see (*21*) for review). A highly constrained 'Rietveld-like' refinement can be performed on a properly normalized PDF in which the unit cell dimensions, atomic positions, displacement, occupancies, and other model-dependent parameters are varied to improve the fit between the observed and calculated PDF (*22*). The starting model best describing the distribution of interatomic distances in ferrihydrite was identified by using the few positions of the most identifiable Bragg features in the XRD patterns. The model presented here for ferrihydrite has an isostructural counterpart in the Al-O-H system that is formed synthetically ("tohdite") and found in nature ("akdalaite") with the composition $Al_{10}O_{14}(OH)_2$ (*23*). There is confusion in the literature regarding this material because early reported data for an akdalaite-type specimen were in error. This inconsistency has recently been reviewed (*23*) and the mineral akdalaite and synthetic tohdite are now understood as equivalent in both structure and composition. As reported in that study, akdalaite is the approved name for the natural alumina hydrate phase having the stoichiometry $Al_{10}O_{14}(OH)_2$ and described by the hexagonal spacegroup $P6_3mc$, with a = 5.58(1) Å, c = 8.86(2) Å.

Based on the real-space fitting results, we contend that the structure of ferrihydrite with domain sizes ranging from 2 to 6 nm can be adequately described by a single phase model with the hexagonal spacegroup $P6_3mc$ and a unit cell with average dimensions of a = ~5.95 Å and c = ~9.06 Å (**Figure 1**). Refinement results for each of the three samples are included in **Tables 1** and **2**. On the basis of this structure in its ideal form the chemical formula for ferrihydrite is $Fe_{10}O_{14}(OH)_2$. Thermal analysis strongly suggests the presence and particle size dependence of additional surface-bound water (*12*). Although the structure of ferrihydrite can be satisfactorily described by a periodic model (**Figure 2**), residuals in the fitting results suggest that second-order effects such as disorder, surface relaxation, internal strain, defects (e.g., stacking faults), particle shape (*24*), and/or inter-particle correlations may also contribute to the experimental PDFs. Misfits in the region between 2.5 and ~6 Å (**Figure 2A-C**) are reminiscent of those found in a similar study of γ-Al_2O_3, where differences are attributed to nanometer-sized domains (~1 nm) reflecting stacking faults in the matrix (*25*).

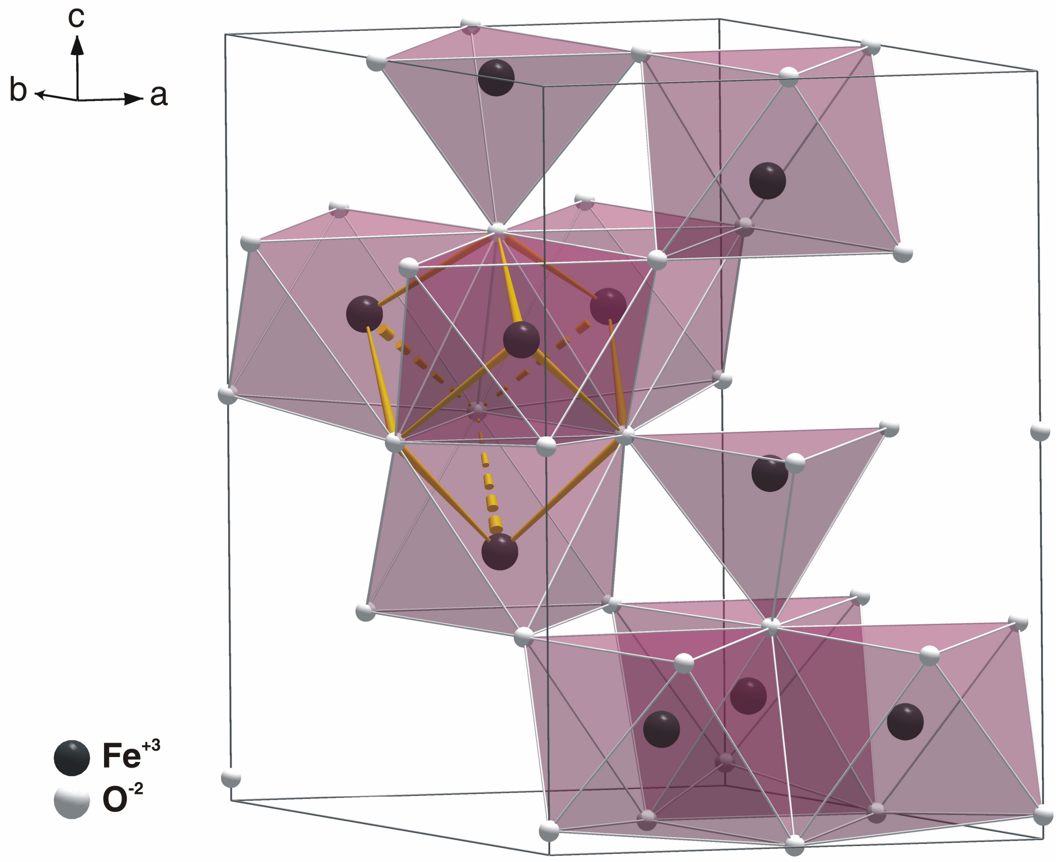

Figure 1. Polyhedral representation of the hexagonal unit cell for ferrihydrite. The bonded atoms (shown in yellow) define a cubane-like moiety that connects the basic structural motif of the model.

Table 1. Refined Lattice Parameters, PDF Sharpening and Attenuation Parameters, Residual Values, and Scale Factors using space group $P6_3mc$

Parameters	**Fhyd6**	**Fhyd3**	**Fhyd2**
a (Å)	5.928(9)	5.953(7)	5.958(7)
c (Å)	9.126(7)	9.096(7)	8.965(7)
σ_Q (Å^{-1})	0.137(8)	0.157(8)	0.217(9)
δ	0.400(7)	0.406(1)	0.336(9)
R_w (%)	26.7	24.9	26.2
Scale (%)	86.3	94.9	124.1

Table 2. Refined Atom Coordinates, Occupancies, and Isotropic Displacement Parameters using space group $P6_3mc$

Fhyd6						
Atom	**Wyck. Pos.**	***x***	***y***	***z***	**Occupancy**	***U* (Å^2)**
Fe1	6c	0.1695(9)	0.8304(2)	0.6365(9)	1.00(2)	0.011(2)
Fe2	2b	1/3	2/3	0.3379(4)	0.97(3)	
Fe3	2b	1/3	2/3	0.9595(3)	0.96(1)	
O1	2a	0	0	0.0446(9)	1.0	0.007(6)
O2	2b	1/3	2/3	0.7634(4)	1.0	
O3	6c	0.1697(7)	0.8302(3)	0.2467(9)	1.0	
O4	6c	0.5227(3)	0.4773(3)	0.9796(2)	1.0	
Fhyd3						
Fe1	6c	0.1688(5)	0.8311(5)	0.6358(1)	1.00(5)	0.010(8)
Fe2	2b	1/3	2/3	0.3347(3)	0.94(1)	
Fe3	2b	1/3	2/3	0.9600(8)	0.93(6)	
O1	2a	0	0	0.0460(2)	1.0	0.008(7)
O2	2b	1/3	2/3	0.7651(3)	1.0	
O3	6c	0.1670(6)	0.8329(6)	0.2457(9)	1.0	
O4	6c	0.5258(3)	0.4742(3)	0.9778(6)	1.0	
Fhyd2						
Fe1	6c	0.1688(4)	0.8312(4)	0.6356(6)	1.01(9)	0.008(9)
Fe2	2b	1/3	2/3	0.3414(6)	0.90(1)	
Fe3	2b	1/3	2/3	0.9538(1)	0.85(1)	
O1	2a	0	0	0.0147(1)	1.0	0.014(6)
O2	2b	1/3	2/3	0.7353(1)	1.0	
O3	6c	0.1671(1)	0.8329(1)	0.2547(8)	1.0	
O4	6c	0.5238(1)	0.4762(1)	0.0053(8)	1.0	

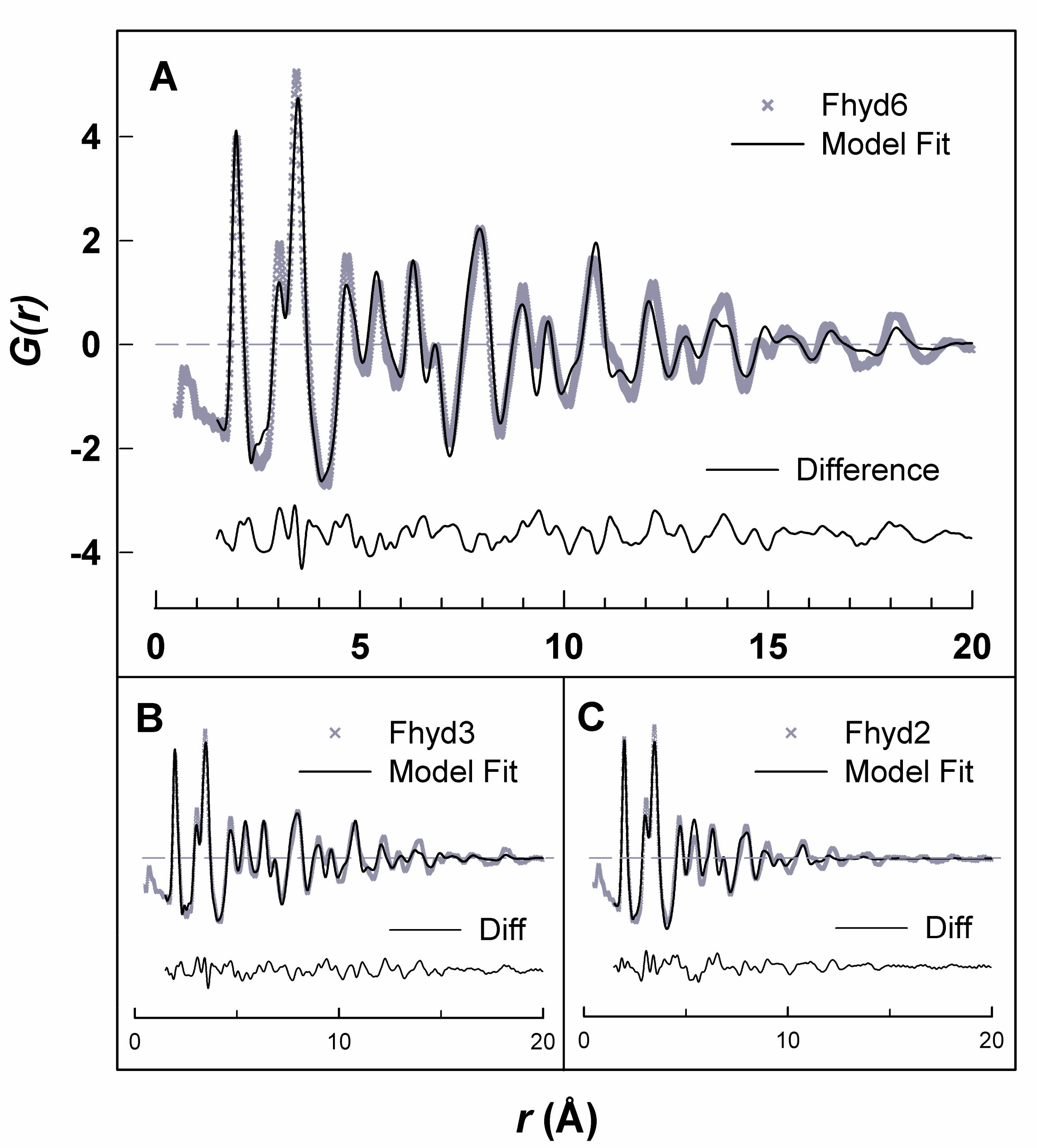

Figure 2a - c. *G(r)* or the PDFs for Fhyd6 (A), Fhyd3 (B), and Fhyd2 (C) plotted to 20 Å (grey x) with the refined fit of the model with group $P6_3mc$ overlain (solid black) for each. Difference plots are shown immediately below.

The basic structural motif of the model, which is closely related to the Baker-Figgis δ-Keggin cluster (*26*), consists of 13 iron atoms and 40 oxygens (**Figure 3**). The central tetrahedrally coordinated Fe is connected via μ_4-oxo bridges to twelve peripheral octahedrally coordinated Fe atoms arranged in edge-sharing groups of three. The 2-to-6 nm ferrihydrite nanoparticles can then be described as a 3-dimensional packing of these clusters with adjacent clusters connected by a common pair of edge-shared octahedra, forming μ_4-oxo bridges from the three μ_2-OH groups *cis* to each of the μ_4-oxo centers in the bare cluster. This arrangement creates a cubane-like moiety corresponding to four edge-shared Fe octahedra (**Figure 1**). Fitting results indicate that some parameters such as unit cell dimensions and occupancies change systematically as the average domain size decreases from 6 nm to 2 nm for Fhyd6 and Fhyd2, respectively. Additionally, the degree of distortion of the Fe1 polyhedra varies as indicated in part by the change in the refined *z*-parameter for the O1 site, but despite these differences, the cluster-like structural motif remains. Such changes could reflect the occurrence of stacking defects or internal strain in the structure but are not fully understood at present.

This structure in its ideal form consists of 20% FeO_4 and 80% FeO_6 polyhedra. However, the Fe2 and Fe3 sites show a decrease in occupancy with decreasing particle size whereas no particle size dependent changes are observed for the fully occupied Fe1 site. This trend might reflect an overall increase in disorder resulting from the change in ratio of Fe atoms near the surface versus interior with decreasing particle size (*27*). These surface regions of ferrihydrite are anticipated to be predominantly octahedrally coordinated given the overall topology of the structure presented and the unlikely

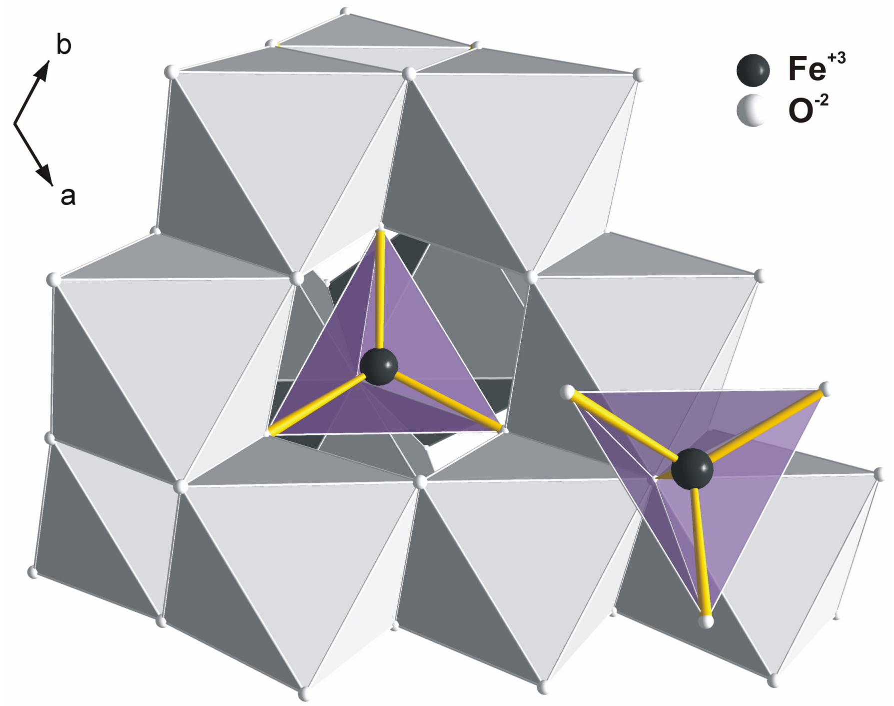

Figure 3. Polyhedral representation of the ideal ferrihydrite structure viewed along the *c*-axis. The central FeO_4 tetrahedra are surrounded by 12 FeO_6 octahedra.

existence of coordinatively unsaturated Fe at the hydrated surfaces. The refined parameters for each sample are available in the supporting online text.

The presence of tetrahedrally coordinated iron in ferrihydrite has been the subject of considerable debate. Previous estimates based on a variety of techniques have ranged from 0% to ~40%, approximately the same amount found in maghemite (γ-Fe_2O_3), and even up to 100% (*28-30*). In a recent study using electron energy loss spectroscopy (EELS) to evaluate the effects of electron beam damage to ferrihydrite, Pan *et al.* (*31*) observed the reduction of Fe^{3+} to Fe^{2+} and a migration of Fe from octahedral to tetrahedral sites with increasing electron dose. These results highlight how investigations carried out under the high vacuum of the transmission electron microscope may cause significant, and perhaps undetected, changes to occur in a sample. Such changes must now be considered when evaluating the most current and increasingly cited multi-phase model for ferrihydrite that was purportedly confirmed using electron nanodiffraction (*7, 8*). Pan *et al.* estimate, by linear extrapolation to very low electron dose (1 electron nm^{-2}), that tetrahedrally coordinated Fe^{3+} could be absent from the pristine structure of ferrihydrite and only appears due to electron beam damage. However, this is a minimum estimate. Peak fitting of the energy loss spectrum recorded at the lowest measured electron dose (3×10^4 electron nm^{-2}) indicates that at this dose as much as 25 ±15 % of the total iron in the mineral is tetrahedrally coordinated Fe^{3+} (*32*). Mössbauer studies performed at temperatures as low as 4.2 K by our group and others (*33*) show spectra completely split magnetically and appearing as sextets. Although this behavior does not rule out the existence of discretely different iron sites, the existence of 4-coordinated iron remains inconclusive (*34*). Future Mössbauer studies at sub-liquid He temperatures may prove useful for further resolving this debate as was demonstrated in a study of a structurally-related Fe_{13} cluster ($((C_5H_6N^+)_5[Fe_{13}F_{24}(OCH_3)_{12}O_4]\cdot CH_3OH\cdot 4H_2O)$) (*35*).

Previously proposed structural models for ferrihydrite were also evaluated as part of this study. In particular, the multi-phase model originally proposed by Drits *et al.* (*7*) which consists of both a defect-free and a defective component was used to calculate individual PDFs. Comparison of the calculated PDFs with the observed experimental PDF for Fhyd6 (**Figure 4**) indicates a relatively poor agreement. There are obvious differences in the correlations of the calculated PDFs found in the regions of both the

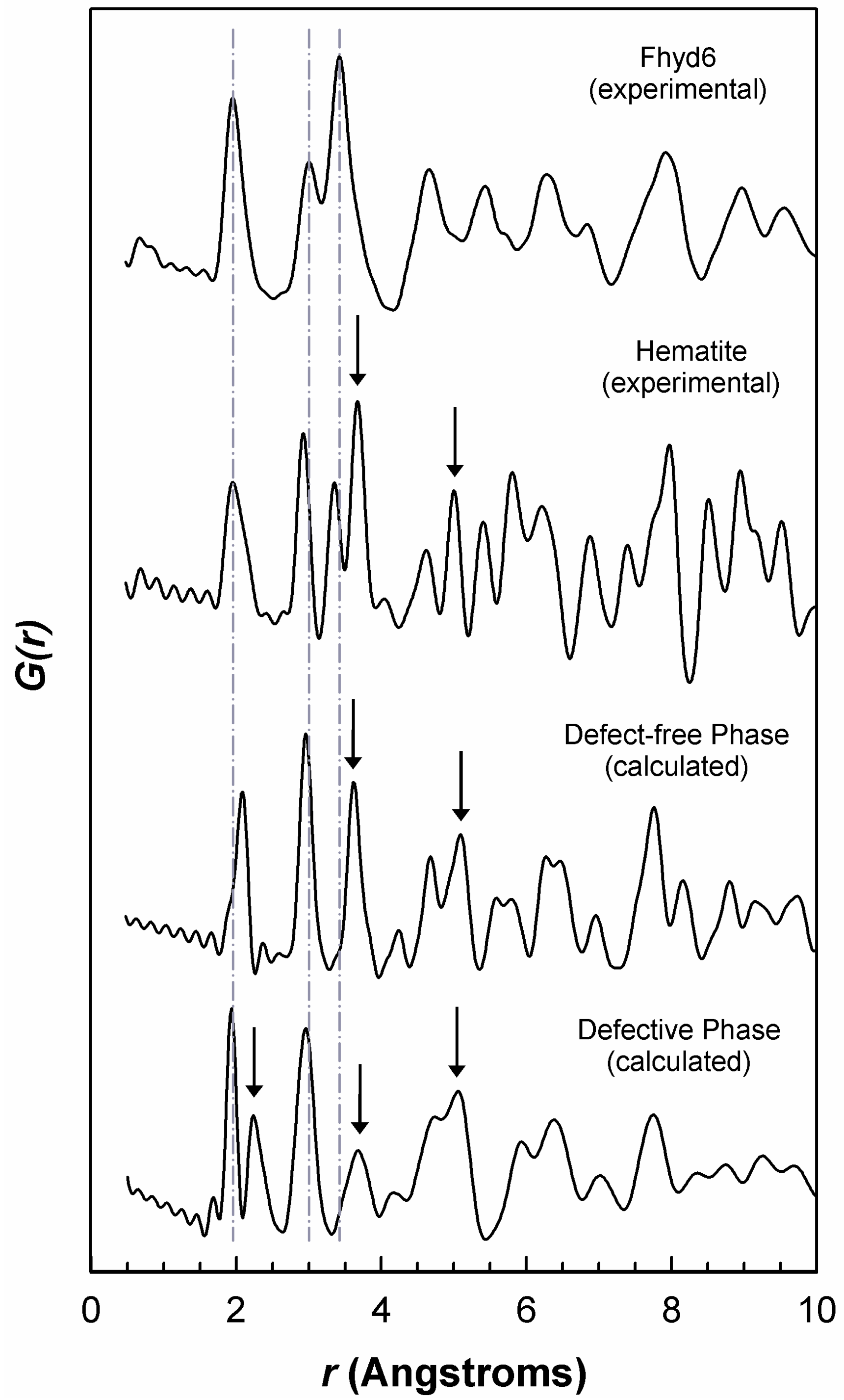

Figure 4. Comparison of calculated PDFs from models originally proposed by Drits *et al.* (*7*) which include the defect-free and defective phases for ferrihydrite as well as so-called ultradisperse hematite to the experimental PDF for Fhyd6. Vertical dashed grid lines (grey) are for reference. Arrows indicate features in the three proposed phases that are not reproduced in the experimental PDF.

local (i.e., <5 Å) and intermediate (5 to 20 Å) range ordering. Differences include both extra correlations (e.g., ~4.2 Å) and mismatches in the intensity of multiple correlations compared to what is observed experimentally. The model presented here was also compared to the raw total X-ray scattering data (**Figure 5**) as well as previous neutron diffraction data collected by Jansen *et al.* (*10*) (**Figure 6**). In the case of X-rays, the the positions of calculated maxima provide a satisfactory match to the observed scattering for all three samples. Some intensity differences are apparent (e.g., ~2.3 and ~4.8 Å) between the calculated and observed maxima. This difference likely results from the combined effects of particle size, morphology, strain (which can be anisotropic), disorder (e.g., stacking faults), and preferred orientation on the diffraction data. These effects are complex and not fully understood, particularly in nanocrystalline compounds like ferrihydrite. Although the combination of the calculated magnetic contribution and the calculated patterns based on the multi-phase structure model presented by Drits *et al.* (*7*) provide partial agreement with the observed neutron diffraction pattern, there are several features left unexplained by any of these three phases (e.g., 18 – 22 ° 2-theta). The model proposed for ferrihydrite in the present study not only describes the most prominent diffraction maxima, but also the subtle features as well.

Whether a 2 nm (i.e., ~30 unit cells) or even a 6 nm plate-like particle can be described using a periodic model is debatable. It has been argued that a particle with maximum dimensions of only several nanometers and possessing significant disorder may itself be described by a single large super cell. The satisfactory fit obtained by the single phase defect-free unit cell for ferrihydrite in the present study does not support this view. Synthetic ferrihydrite samples with average coherent scattering domain sizes ranging from 2 to 6 nm can be described by a single phase periodic structure that does not require multiphase, size-dependent models. The structure model proposed here for ferrihydrite does not address the positions for H-sites. However, we anticipate that, with the iron and oxygen framework established, neutron total scattering studies on deuterated ferrihydrite will provide a complete model.

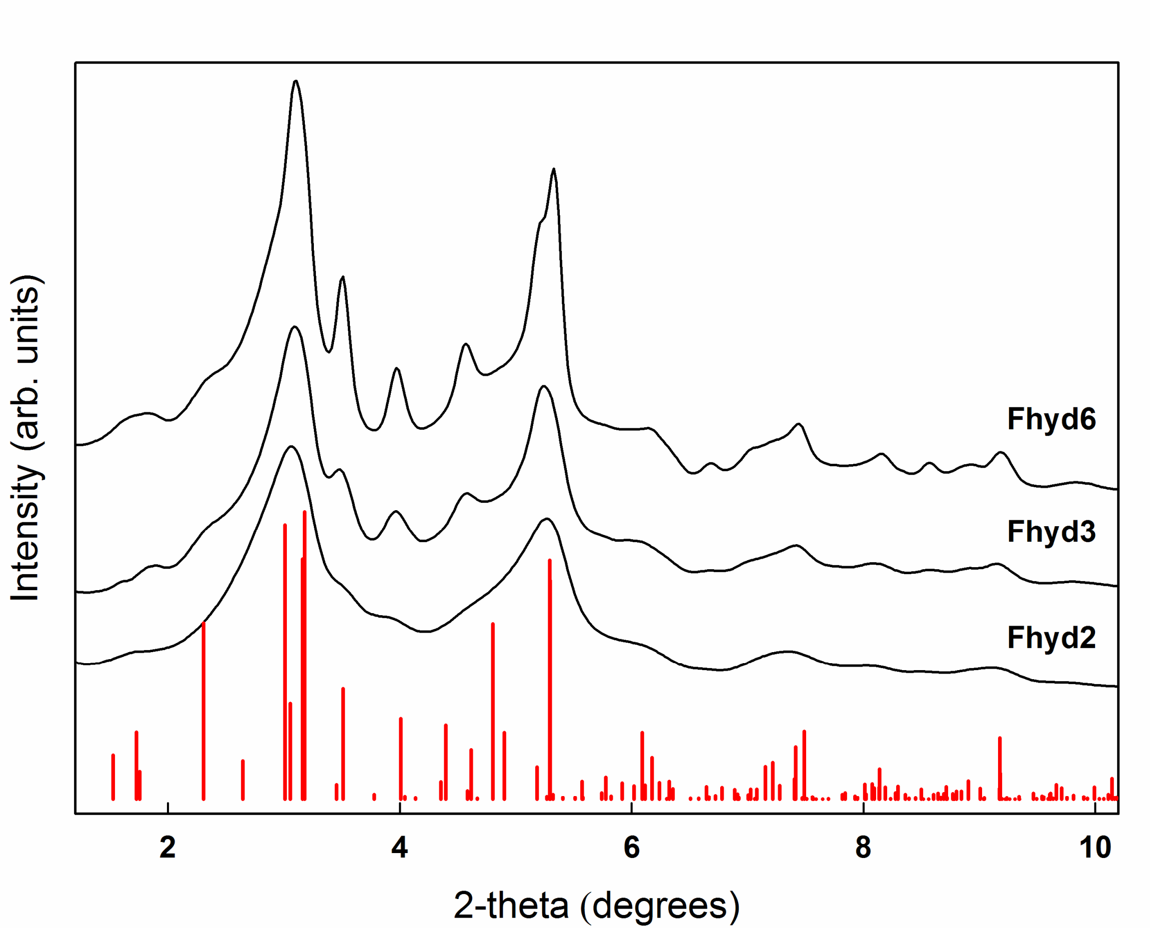

Figure 5. Comparison of the raw X-ray total scattering data for Fhyd2, Fhyd3, and Fhyd6 (*solid black*) to the calculated positions and intensities of maxima for the new model presented for ferrihydrite that is based on space group $P6_3mc$ are included below (*red*).

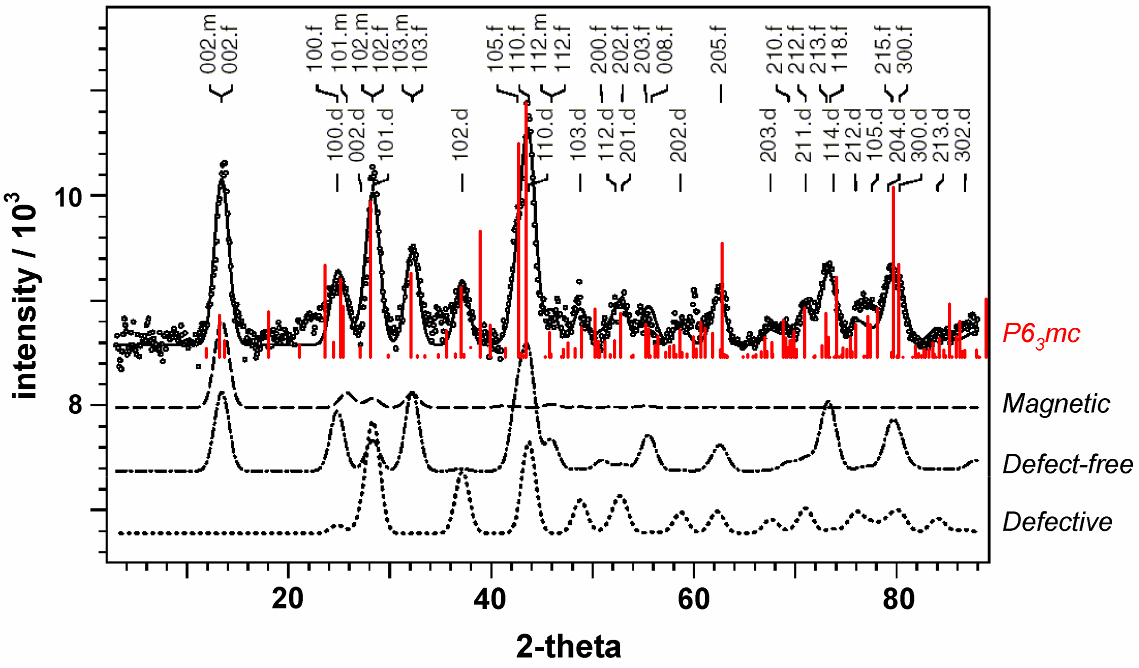

Figure 6. Comparison of the neutron diffraction pattern for a non-deuterated sample of 6-line ferrihydrite (*dots*) to calculated patterns based on the multi-phase model (defect-free and defective) originally proposed by Drits *et al.* (*7*). The calculated positions and intensities of maxima for the model presented for ferrihydrite in this study based on space group $P6_3mc$ are overlain (*red*). Figure adapted from that originally presented in (*10*).

Conclusions

Quantitatively evaluating the structures of materials that exhibit coherent periodicity only on length scales of the order <10 nm and are sensitive to changes under vacuum, represents a considerable challenge for conventional diffraction methods and electron imaging techniques. Although *ab initio* structure determination of nanocrystalline materials is in its infancy (*36*), domain-limited PDFs from total scattering data to very high reciprocal space values (i.e., ≥25 Angstroms^{-1}) provide a map of interatomic distances, which can be fitted with competing structure models (e.g., (*37*)). Such models may appear to be quite similar in terms of short range ordering (i.e., distances of 1 to 5 Angstroms) but are distinguishable over intermediate-range length scales (i.e., 5 to 20 Angstroms) due to differences in overall topology. Although it is not possible to demonstrate the uniqueness of a successful model, a solution which is consistent with the experimental PDF over 20 Angstroms, or more, provides strong confidence in the result. Traditional structure solution in well-ordered periodic materials relies on the interpretation of sharp Bragg reflections to derive an initial unit cell. This conventional approach is generally not feasible for nanocrystalline materials like ferrihydrite due to the lack of discernable Bragg reflections in diffraction patterns dominated by broad diffuse scattering. This diffuse component results not only from extremely small coherent scattering domain sizes, but also from surface relaxation, strain, and complex disorder which often distinguishes the structures of nanocrystalline materials from their bulk counterparts (*38*). Thus, the interpretation of the broad diffuse diffraction patterns of nanometer-sized crystals through observation of structural details in real space via the pair distribution function method provides the best means of discrimination between existing, and potentially closely related models.

References

1. D. G. Rancourt *et al.*, *American Mineralogist* **86**, 834 (2001).
2. U. Schwertmann, L. Carlson, E. Murad, *Clays and Clay Minerals* **35**, 297 (1987).
3. G. P. Huffman *et al.*, *Energy & Fuels* **7**, 285 (1993).
4. P. A. Riveros, J. E. Dutrizac, P. Spencer, *Canadian Metallurgical Quarterly* **40**, 395 (2001).
5. R. M. Cornell, U. Schwertmann, *The Iron Oxides: Structure, Properties, Reactions, Occurrence and Uses.* (VCH, Weinheim, Germany, 1996), pp. 1-659.
6. A. Lewin, G. R. Moore, N. E. Le Brun, *Dalton Transactions*, 3597 (2005).
7. V. A. Drits, B. A. Sakharov, A. L. Salyn, A. Manceau, *Clay Minerals* **28**, 185 (1993).
8. D. E. Janney, J. M. Cowley, P. R. Buseck, *American Mineralogist* **85**, 1180 (2000).
9. D. E. Janney, J. M. Cowley, P. R. Buseck, *American Mineralogist* **86**, 327 (2001).
10. E. Jansen, A. Kyek, W. Schafer, U. Schwertmann, *Applied Physics A-Materials Science & Processing* **74**, S1004 (2002).
11. J. L. Jambor, J. E. Dutrizac, *Chemical Reviews* **98**, 2549 (1998).
12. F. M. Michel *et al.*, *Chemistry of Materials* **19**, 1489 (2007).
13. A. J. Anschutz, R. L. Penn, *Geochemical Transactions* **6**, 60 (2005).
14. U. Schwertmann, R. M. Cornell, *Iron Oxides in the Laboratory: Preparation and Characterization* (Wiley - VCH, Weinheim, ed. 1st, 2000), pp. 89-94.
15. U. Rutt *et al.*, *Nuclear Instruments & Methods in Physics Research Section a-Accelerators Spectrometers Detectors and Associated Equipment* **467**, 1026 (2001).
16. "Fit2D" V. 9.129 Reference Manual V. 3.1.
17. A. P. Hammersley, S. O. Svenson, M. Hanfland, D. Hauserman, *High Pressure Research* **14**, 235 (1996).

18. X. Qiu, J. W. Thompson, S. J. L. Billinge, *Journal of Applied Crystallography* **37**, 110 (2004).

19. P. J. Chupas *et al.*, *Journal of Applied Crystallography* **36**, 1342 (2003).

20. T. Proffen, S. J. L. Billinge, *Journal of Applied Crystallography* **32**, 572 (1999).

21. S. J. L. Billinge, M. G. Kanatzidis, *Chemical Communications* **7**, 749 (2004).

22. T. Egami, S. J. L. Billinge, *Underneath the Bragg Peaks: Structural Analysis of Complex Materials*. R. W. Cahn, Ed., Pergamon Materials Series (Elsevier, Oxford, 2003), pp. 1-404.

23. S. L. Hwang, P. Y. Shen, H. T. Chu, T. F. Yui, *International Geology Review* **48**, 754 (2006).

24. K. Kodama, S. Iikubo, T. Taguchi, S. Shamoto, *Acta Crystallographica Section A* **62**, 444 (2006).

25. G. Paglia, E. S. Bozin, S. J. L. Billinge, *Chemistry of Materials* **18**, 3242 (2006).

26. W. H. Casey, *Chemical Reviews* **106**, 1 (2006).

27. I. Joumard *et al.*, *Physical Review B* **74** (2006).

28. G. W. Brady *et al.*, *Biochemistry* **7**, 2185 (1968).

29. R. A. Eggleton, R. W. Fitzpatrick, *Clays and Clay Minerals* **36**, 111 (1988).

30. Q. A. Pankhurst, R. J. Pollard, *Clays and Clay Minerals* **40**, 268 (1992).

31. Y. Pan *et al.*, *Micron* **37**, 403 (2006).

32. Y. Pan, University of Leeds (2007).

33. Y. Guyodo *et al.*, *Physics of the Earth and Planetary Interiors* **154**, 222 (2006).

34. E. Murad, U. Schwertmann, *American Mineralogist* **65**, 1044 (1980).

35. J. van Slageren *et al.*, *Physical Review B* **73** (2006).

36. P. Juhas, D. M. Cherba, P. M. Duxbury, W. F. Punch, S. J. L. Billinge, *Nature* **440**, 655 (2006).

37. V. Petkov *et al.*, *Physical Review B* **65** (2002).

38. B. Gilbert, F. Huang, H. Z. Zhang, G. A. Waychunas, J. F. Banfield, *Science* **305**, 651 (2004).

Crystallographic Information Files.

```
data_Fhyd6
_ccdc_journal_manuscript_code    1142525
_publ_requested_journal          Science
_publ_contact_author_name        'F. Marc Michel'
_publ_contact_author_address
;Department of Geosciences
Stony Brook University
255 Earth & Space Sciences Bldg.
Stony Brook, NY 11794-2100
;
_publ_contact_author_email       fmichel@ic.sunysb.edu
_publ_contact_author_phone       631-632-6839
_publ_contact_author_fax         631-632-8240

_audit_creation_method           'Created with Diamond
                                 (www.crystalimpact.com)'
_audit_creation_date             07-04-24
_audit_update_record             07-04-24
_chemical_name_systematic        '6 nm Iron oxyhydroxide'
_chemical_formula_structural     'Fe9.86 O14 (OH)2'
_chemical_formula_sum            'H2 Fe9.86 O16'
_chemical_name_mineral           Ferrihydrite
_chemical_formula_weight         808.651
_chemical_compound_source        Synthetic

_cell_length_a                   5.928(9)
_cell_length_b                   5.928(9)
_cell_length_c                   9.126(7)
_cell_angle_alpha                90.
_cell_angle_beta                 90.
_cell_angle_gamma                120.
_cell_volume                     277.8
_cell_formula_units_Z            1

_symmetry_cell_setting           hexagonal
_symmetry_space_group_name_H-M   'P 63 m c'
_symmetry_int_tables_number      186
_symmetry_space_group_name_Hall  P_6c_-2c

_diffrn_radiation_probe          x-ray
_diffrn_radiation_type           monochromatic
_diffrn_radiation_wavelength     0.1370(2)
_diffrn_source                   synchrotron
_diffrn_source_type              'APS Beamline 11-ID-B'

loop_
_symmetry_equiv_pos_site_id
_symmetry_equiv_pos_as_xyz
1 'x, y, z'
2 'x-y, x, 1/2+z'
3 '-y, x-y, z'
4 '-x, -y, 1/2+z'
5 '-x+y, -x, z'
6 'y, -x+y, 1/2+z'
7 '-x+y, y, z'
8 'x, x-y, z'
9 '-y, -x, z'
10 'y, x, 1/2+z'
11 'x-y, -y, 1/2+z'
12 '-x, -x+y, 1/2+z'
```

```
loop_
_atom_type_symbol
_atom_type_oxidation_number
Fe3+ 3
O2-  -2
H1+  1

loop_
_atom_site_label
_atom_site_type_symbol
_atom_site_symmetry_multiplicity
_atom_site_Wyckoff_symbol
_atom_site_fract_x
_atom_site_fract_y
_atom_site_fract_z
_atom_site_occupancy
_atom_site_attached_hydrogens
_atom_site_u_iso_or_equiv
Fe1 Fe3+ 6 c 0.1695(9) 0.8304(2) 0.6365(9) 1.00(2) 0 0.011(2)
Fe2 Fe3+ 2 b 0.3333 0.6667 0.3379(4) 0.97(3) 0 0.011(2)
Fe3 Fe3+ 2 b 0.3333 0.6667 0.9595(3) 0.96(1) 0 0.011(2)
O1 O2- 2 a 0 0 0.0446(9) 1. 0 0.007(6)
O2 O2- 2 b 0.3333 0.6667 0.7634(4) 1. 0 0.007(6)
O3 O2- 6 c 0.1697(7) 0.8302(3) 0.2467(9) 1. 0 0.007(6)
O4 O2- 6 c 0.5227(3) 0.4773(3) 0.9796(2) 1. 0 0.007(6)

#Position of 2 Elements of H Are Undetermined.
#End of data_Fhyd6
```

```
data_Fhyd3
_ccdc_journal_manuscript_code    1142525
_publ_requested_journal          Science
_publ_contact_author_name        'F. Marc Michel'
_publ_contact_author_address
;Department of Geosciences
Stony Brook University
255 Earth & Space Sciences Bldg.
Stony Brook, NY 11794-2100
;
_publ_contact_author_email       fmichel@ic.sunysb.edu
_publ_contact_author_phone       631-632-6839
_publ_contact_author_fax         631-632-8240

_audit_creation_method           'Created with Diamond
                                 (www.crystalimpact.com)'
_audit_creation_date             07-04-24
_audit_update_record             07-04-24
_chemical_name_systematic        '3 nm Iron oxyhydroxide'
_chemical_formula_structural     'Fe9.76 O14 (OH)2'
_chemical_formula_sum            'H2 Fe9.76 O16'
_chemical_name_mineral           Ferrihydrite
_chemical_formula_weight         803.067
_chemical_compound_source        Synthetic

_cell_length_a                   5.953(7)
_cell_length_b                   5.953(7)
_cell_length_c                   9.096(7)
_cell_angle_alpha                90.
_cell_angle_beta                 90.
_cell_angle_gamma                120.
_cell_volume                     279.2
_cell_formula_units_Z            1

_symmetry_int_tables_number        186
_symmetry_space_group_name_H-M     'P 63 m c'
_symmetry_space_group_name_Hall    'P_6c_-2c'
_symmetry_cell_setting             hexagonal

_diffrn_radiation_probe            x-ray
_diffrn_radiation_type             monochromatic
_diffrn_radiation_wavelength       0.1370(2)
_diffrn_source                     synchrotron
_diffrn_source_type                'APS Beamline 11-ID-B'

loop_
_symmetry_equiv_pos_site_id
_symmetry_equiv_pos_as_xyz
1 'x, y, z'
2 'x-y, x, 1/2+z'
3 '-y, x-y, z'
4 '-x, -y, 1/2+z'
5 '-x+y, -x, z'
6 'y, -x+y, 1/2+z'
7 '-x+y, y, z'
8 'x, x-y, z'
9 '-y, -x, z'
10 'y, x, 1/2+z'
11 'x-y, -y, 1/2+z'
12 '-x, -x+y, 1/2+z'

loop_
_atom_type_symbol
_atom_type_oxidation_number
```

```
Fe3+  3
O2-   -2
H1+   1

loop_
_atom_site_label
_atom_site_type_symbol
_atom_site_symmetry_multiplicity
_atom_site_Wyckoff_symbol
_atom_site_fract_x
_atom_site_fract_y
_atom_site_fract_z
_atom_site_occupancy
_atom_site_attached_hydrogens
_atom_site_u_iso_or_equiv
Fe1 Fe3+ 6 c 0.1688(5) 0.8311(5) 0.6358(1) 1.00(5) 0 0.010(8)
Fe2 Fe3+ 2 b 0.3333 0.6667 0.3347(3) 0.94(1) 0 0.010(8)
Fe3 Fe3+ 2 b 0.3333 0.6667 0.9600(8) 0.93(6) 0 0.010(8)
O1 O2- 2 a 0 0 0.0460(2) 1. 0 0.008(7)
O2 O2- 2 b 0.3333 0.6667 0.7651(3) 1. 0 0.008(7)
O3 O2- 6 c 0.1670(6) 0.8329(6) 0.2467(9) 1. 0 0.008(7)
O4 O2- 6 c 0.5258(3) 0.4742(3) 0.9778(6) 1. 0 0.008(7)

#Position of 2 Elements of H Are Undetermined.
#End of data_Fhyd3
```

```
data_Fhyd2
_ccdc_journal_manuscript_code    1142525
_publ_requested_journal          Science
_publ_contact_author_name        'F. Marc Michel'
_publ_contact_author_address
;Department of Geosciences
Stony Brook University
255 Earth & Space Sciences Bldg.
Stony Brook, NY 11794-2100
;
_publ_contact_author_email       fmichel@ic.sunysb.edu
_publ_contact_author_phone       631-632-6839
_publ_contact_author_fax         631-632-8240

_audit_creation_method           'Created with Diamond
                                 (www.crystalimpact.com)'
_audit_creation_date             07-04-24
_audit_update_record             07-04-24
_chemical_name_systematic        '2 nm Iron oxyhydroxide'
_chemical_formula_structural     'Fe9.5 O14 (OH)2'
_chemical_formula_sum            'H2 Fe9.5 O16'
_chemical_name_mineral           Ferrihydrite
_chemical_formula_weight         788.547
_chemical_compound_source        Synthetic

_cell_length_a                   5.958(7)
_cell_length_b                   5.958(7)
_cell_length_c                   8.965(7)
_cell_angle_alpha                90.
_cell_angle_beta                 90.
_cell_angle_gamma                120.
_cell_volume                     275.7
_cell_formula_units_Z            1

_symmetry_int_tables_number   186
_symmetry_space_group_name_H-M      'P 63 m c'
_symmetry_space_group_name_Hall     'P_6c_-2c'
_symmetry_cell_setting              hexagonal

_diffrn_radiation_probe             x-ray
_diffrn_radiation_type              monochromatic
_diffrn_radiation_wavelength        0.1370(2)
_diffrn_source                      synchrotron
_diffrn_source_type                 'APS Beamline 11-ID-B'

loop_
_symmetry_equiv_pos_site_id
_symmetry_equiv_pos_as_xyz
1 'x, y, z'
2 'x-y, x, 1/2+z'
3 '-y, x-y, z'
4 '-x, -y, 1/2+z'
5 '-x+y, -x, z'
6 'y, -x+y, 1/2+z'
7 '-x+y, y, z'
8 'x, x-y, z'
9 '-y, -x, z'
10 'y, x, 1/2+z'
11 'x-y, -y, 1/2+z'
12 '-x, -x+y, 1/2+z'

loop_
_atom_type_symbol
_atom_type_oxidation_number
```

```
Fe3+  3
O2-   -2
H1+   1

loop_
_atom_site_label
_atom_site_type_symbol
_atom_site_symmetry_multiplicity
_atom_site_Wyckoff_symbol
_atom_site_fract_x
_atom_site_fract_y
_atom_site_fract_z
_atom_site_occupancy
_atom_site_attached_hydrogens
_atom_site_u_iso_or_equiv
Fe1 Fe3+ 6 c 0.1688(4) 0.8312(4) 0.6356(6) 1.01(9) 0 0.008(9)
Fe2 Fe3+ 2 b 0.3333 0.6667 0.3414(6) 0.90(1) 0 0.008(9)
Fe3 Fe3+ 2 b 0.3333 0.6667 0.9538(1) 0.85(1) 0 0.008(9)
O1 O2- 2 a 0 0 0.0147(1) 1. 0 0.014(6)
O2 O2- 2 b 0.3333 0.6667 0.7353(1) 1. 0 0.014(6)
O3 O2- 6 c 0.1671(1) 0.8329(1) 0.2547(8) 1. 0 0.014(6)
O4 O2- 6 c 0.5238(1) 0.4762(1) 0.0053(8) 1. 0 0.014(6)

#Position of 2 Elements of H Are Undetermined.
#End of data_Fhyd2
```

Chapter 7: Structure of the Iron Core in Horse-Spleen Ferritin

F. M. Michel [a,b], *S. Debnath* [a,c], *D. R. Strongin* [a,c], *L. Ehm* [a,b], *C. Tarabrella* [b], *P. L. Lee* [d], *P. J. Chupas* [d], *M. A. A. Schoonen* [a,b], *J. B. Parise* [a,b,e],

[a] *Center for Environmental Molecular Science (CEMS)*
[b] *Department of Geosciences, Stony Brook University, Stony Brook, New York 11794*
[c] *Department of Chemistry, Temple University, Philadelphia, Pennsylvania, 19122*
[d] *Advanced Photon Source, Argonne National Laboratory, Argonne, Illinois 60439*
[e] *Department of Chemistry, Stony Brook University, Stony Brook, New York 11794*

Abstract

Iron storage proteins known as ferritins are essential for the regulation of iron in most living organisms. This roughly spherical protein has evolved with the remarkable ability to absorb soluble Fe^{2+} species into its hollow interior and reversibly store the iron as a nano-sized ferric oxyhydroxide particle. While it is long recognized that the Fe^{3+} core resembles the mineral ferrihydrite, a quantitative structure model is lacking. Analysis of high-energy total x-ray scattering data collected from native horse-spleen ferritin shows that the inorganic core is a single phase and adopts a structure that is consistent with a recently-determined structure model for ferrihydrite. Additionally, comparison to data collected on apoferritin reconstituted with 3000 iron atoms/protein shows that the heat treatment (5 – 10 min, 75 ºC) routinely done on commercially-available samples does not result in a structural transformation of the iron core.

Introduction

The evolutionary solution to the problem of storing and releasing iron, an essential element for cellular activity in humans and most animals, plants, and microbes, is through protein-encapsulated iron(III) oxyhydroxide nanoparticles. The class of proteins known as ferritins has the remarkable ability to absorb soluble Fe^{2+} species into its hollow interior and reversibly store the iron as relatively insoluble, ferric oxyhydroxide particles (**Figure 1**) (See (*1*) for review). These nano-sized and generally

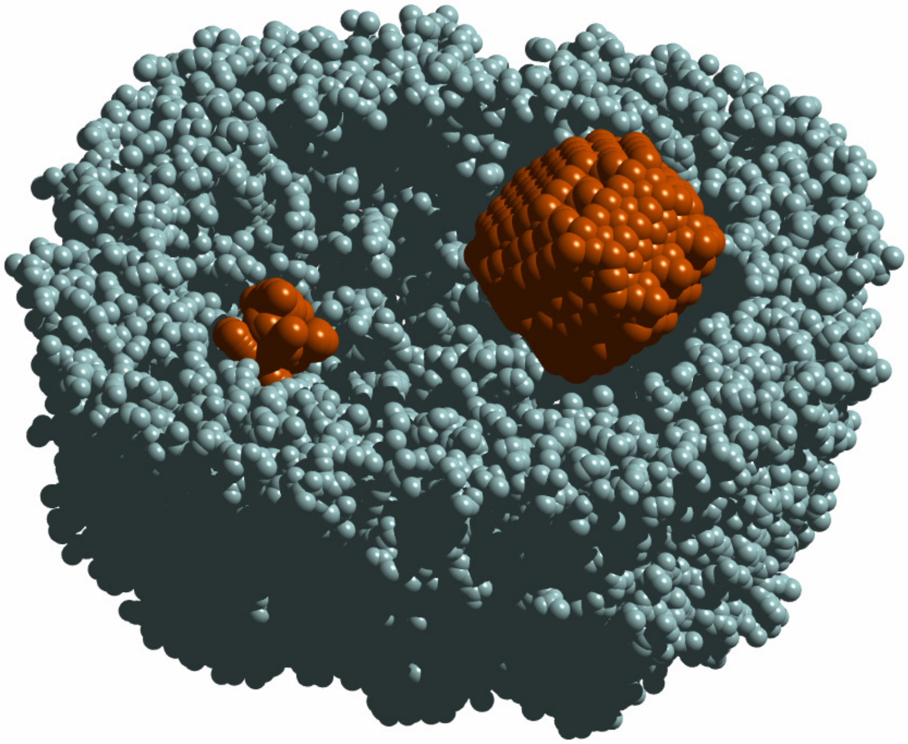

Figure 1. A three-dimensional conceptual representation showing half a molecule of HoSF, an intracellular iron storage protein (blue-grey). Ferritin is roughly spherical in shape, and iron is stored as one or more nano-sized ferrihydrite particles (orange) in its interior.

spherical storage vessels (outer/inner diameter ~12.5/8.0 nm) catalyze the oxidation of iron from its soluble 2+ valence state through ferroxidase activity (*2*). While the structure of the native horse-spleen ferritin (HoSF) protein is established (*3*), the nano-sized iron core (< ~7 nm) has most recently been described as a mixture of phases, including maghemite, hematite, and ferrihydrite (*4*). Now that the elusive structure of synthetic, inorganically-derived ferrihydrite has been solved (*5*), similar methods can be applied to evaluate the structure of the native ferric core of naturally occurring ferritin. We believe that the nanocrystallinity of the core, presence of significant parasitic scattering from the organic protein shell, and an incorrect starting model for ferrihydrite all have impeded prior attempts to fully understanding the core structure.

Experimental

A concentrated sample of horse-spleen ferritin (HoSF) was purchased from Calzyme Laboratories. The as-obtained native ferritin had a concentration of 50 mg/ml in sodium chloride buffer solution, as stated by the manufacturer. The HoSF solution was diluted to a concentration of 1 mg/ml and the protein concentration was checked using our Bradford Assay standard curve. After dialysis of native ferritin for 48 hours using deionized water (DI), the solution was flash frozen in liquid nitrogen and freeze dried (FD) until a dry powder of ferritin with a reddish color was obtained. A small portion of FD ferritin sample was subsequently re-suspended in DI resulting in a dark brown suspension. The protein concentration of the FD and re-suspended ferritin was again checked with our standard curve and an identical protein concentration was obtained indicating that the protein stays intact with virtually no detectable fragmentation. It should be noted that commercial samples of ferritin like the one used here are routinely heat treated for 5 – 10 minutes at 75 ºC as part of the purification and extraction process (e.g., (*6*)).

Apoferritin (APO) was obtained by performing demineralization on the native ferritin. The iron(III) core was reduced to iron(II) by treating native ferritin with TGA (thioglycolic acid) under anoxic conditions. The reduced iron(II) is leached out of the protein interior into the sodium acetate buffer solution at pH 4.5 until the protein becomes colorless. The colorless ferritin indicates the loss of iron(III) from the core. The

APO was then dialyzed in sodium chloride buffer at pH 4.5, followed by dialysis in MES buffer at pH 6.5. The concentration of APO was adjusted to 1mg/ml and confirmed using by the Coomassie test. The APO was dialyzed again in DI for 48 hours to remove the buffer prior to FD.

A fraction of the APO (demineralized HoSF) was reconstituted in vitro with a loading of 3000 Fe atoms/protein (FeFn-3000). The sample was prepared by addition of deoxygenated ferrous ammonium sulfate solution ($(NH_4)_2Fe(SO_4)\cdot 6H_2O$, 10 mg/ml, Sigma-Aldrich) to 5 mg of APO in 20 mL of MES buffer (0.1 M) at pH 6.5 followed by air oxidation. Six 0.2 ml aliquots of ferrous ammonium sulfate were added to APO with intervals of 1 hour between each addition. The reconstituted ferritin was dialyzed in 0.1 M tris buffer at pH 8.5 and subsequently dialyzed in DI prior to freeze-drying according to the method described above.

The dry sample of HoSF with the protein shell still intact was evaluated using high-energy total x-ray scattering and pair distribution function (PDF) analysis. In order to evaluate the scattering from the core only, the parasitic scattering from the protein and sample holder was removed by independently measuring the scattering of APO, iron-free protein loaded into an identical container. The differential scattering pattern of the core shows broadened diffraction maxima in the low-angle region (< 8 Å^{-1}), typical of nano-sized ferrihydrite (**Figure 2**).

High energy x-ray total scattering data were collected at the 1-ID (~100 keV, $\lambda = 0.1240(6)$ Å) beamline at the Advanced Photon Source at Argonne National Laboratory. A CeO_2 standard (NIST diffraction intensity standard set: 674a) was used to calibrate the sample-to-detector distance and the non-orthogonality of the detector relative to the incident beam path. The radiation scattered by the calibrant and samples was collected on an amorphous Si detector system manufactured by General Electric. Conversion of data from 2D to 1D was done using the program Fit-2D (*7, 8*). A polarization correction was applied during integration of the data.

The total scattering structure function $S(Q)$ and PDF $G(r)$ were obtained using PDFgetX2 (*9*) where standard corrections were applied as well as those unique to image-plate geometry (*10*). The composition incorporated in the normalization was $Fe_{10}O_{14}(OH_2)\cdot 3H_2O_{ads}$. The three additional units of stoichiometric water were estimated

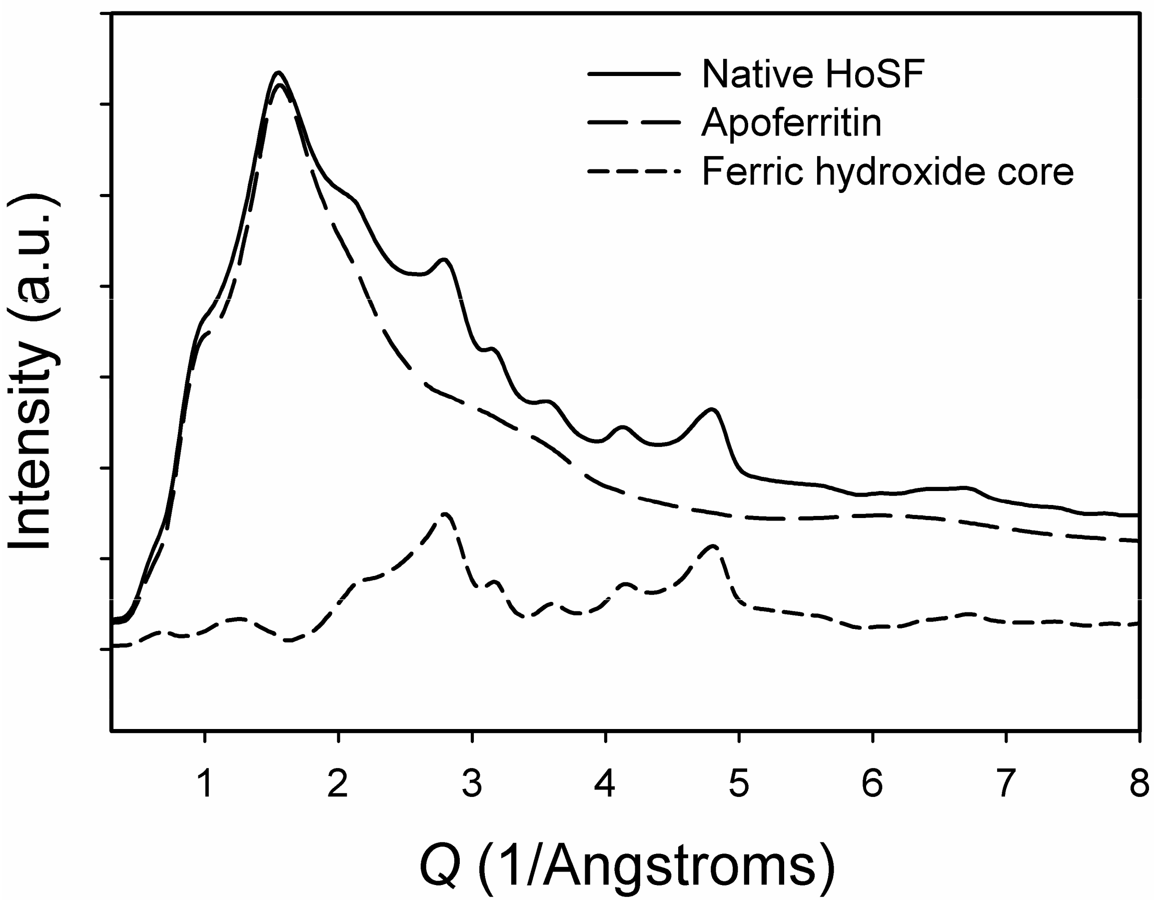

Figure 2. The low-angle portion of the experimental total x-ray scattering for native HoSF (solid) shows the scattering of the entire sample (ferritin molecules and Fe core) and includes the capillary holder. The parasitic scattering of the APO and capillary (long dashes) is subtracted directly from that of the sample. The resulting pattern of the iron core (short dashes) shows broadened diffraction maxima typical of nano-sized ferrihydrite.

by PDF only but are consistent with previous estimates of surface-adsorbed water associated with nanocrystalline ferrihydrite (*11*). The PDF was calculated from the Fourier transform of the experimental reduced structure function truncated at ~26 Å^{-1} (**Figure 3 -** bottom inset).

The new model for ferrihydrite (*5*) was fitted to the experimental PDF and the structural parameters of the model were refined using the program DiffPy (*12*). The parameters varied during the refinement were included in the following order: 1) scale, resolution dampening (σ_Q); 2) unit cell parameters; 3) *r*-dependent peak-width ratio (srat); 4) atomic coordinates; 5) isotropic displacement parameters (U); 6) correlated motion (δ); and 7) occupancy of Fe. Additional global parameters related to the PDF and a "goodness of fit" indicator, expressed as a weighted residual value (R_w), are included in **Table 1**. Refined atomic coordinates, occupancies, and isotropic displacement parameters are included in **Table 2**. The refined parameters pertaining to the structure are included in the Crystallographic Information File included at the end of this chapter.

If within the resolution of the instrument, the exponential decay of the PDF can be attributed to a limited range of structural coherence in nanocrystalline materials (i.e. average particle size) (*13*). The PDFs for HoSF and FeFn-3000 attenuate at approximately 45 (**Figure 3** and top inset) and 50 Å (not shown), respectively, both are within the resolution of this instrument (*14*). This is only an average value and the actual distribution of core sizes may be quite large (*15*), particularly for the native HoSF.

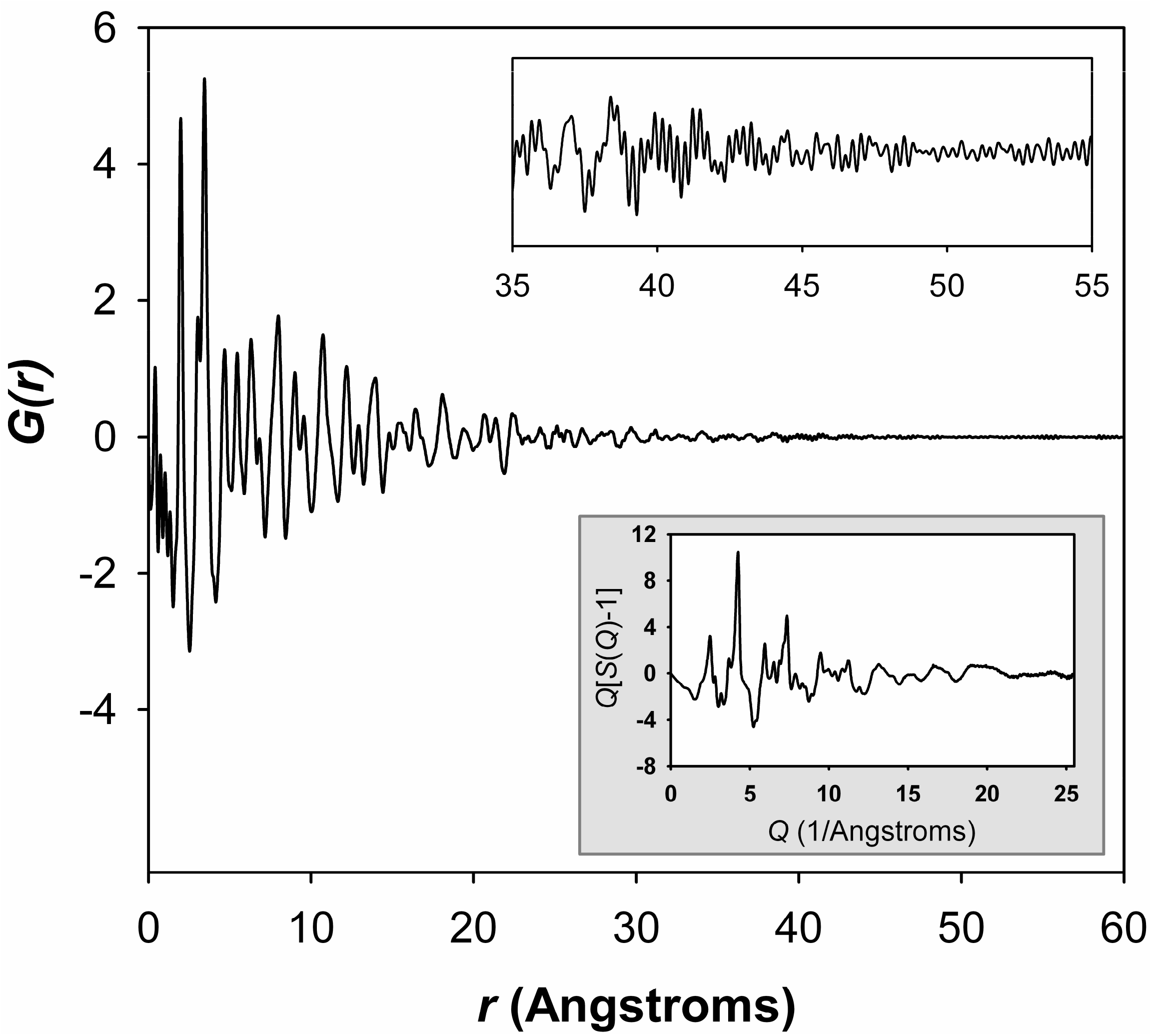

Figure 3. The main pane shows the PDF for the native HoSF core plotted to 60 Å. The average domain size, estimated from the coherence length of the PDF, is approximately 45 Å (upper inset). The lower inset shows the experimental structure function used in the calculation of the PDF. The composition used during the normalization is $Fe_{10}O_{14}(OH_2)\cdot 3H_2O_{ads}$, which includes a small amount of additional water assumed to be surface adsorbed.

Table 1. Refined Lattice Parameters, PDF Global Sharpening and Attenuation Parameters, Residual Values, and Scale Factors using space group $P6_3mc$ for the native HoSF core

Parameters	**Native Ferritin**
a (Å)	5.9745(6)
c (Å)	9.0793(4)
σ_Q (Å^{-1})	1.823(2)
Linear Corr. Factor (δ)	0.138(4)
Low r sigma ratio (*srat*)	0.709(8)
Low r-cutoff (Å)	4.1
R_w (%)	27.6
Scale (%)	110.5

Table 2. Refined Atom Coordinates, Occupancies, and Isotropic Displacement Parameters using space group $P6_3mc$ for the native HoSF core

Native Ferritin						
Atom	**Wyck. Pos.**	***x***	***y***	***z***	**Occupancy**	U **(Å^2)**
Fe1	6c	0.1688(8)	0.8311(2)	0.6305(6)	0.99(3)	0.024(1)
Fe2	2b	1/3	2/3	0.3245(8)	0.97(6)	
Fe3	2b	1/3	2/3	0.9505(8)	0.91(1)	
O1	2a	0	0	0.0525(4)	1.0	0.007(3)
O2	2b	1/3	2/3	0.7592(8)	1.0	
O3	6c	0.1612(9)	0.8387(2)	0.2379(4)	1.0	
O4	6c	0.5393(6)	0.4606(4)	0.9793(1)	1.0	

Results & Discussion

Commercially-available samples of HoSF are concentrated mixtures derived from multiple equine sources and it is therefore expected that the inorganic cores will be in various stages of nucleation, growth, and even dissolution. Further, as conceptualized in **Figure 1**, single proteins can at one time contain multiple individual particles that may vary widely in size (*15*). Performing a quantitative evaluation of the atomic arrangement of the nanocrystalline iron core in HoSF is possible by fitting the real-space interatomic distances in the PDF using structural models. The new single-phase structure model for ferrihydrite (*5*) provides an excellent fit to the PDF of the native core in HoSF (**Figure 4**). The refined structural parameters (**Tables 1 & 2**) of the inorganic core are consistent with those reported for nanocrystalline ferrihydrite with particle sizes < 7 nm (*5*). The average coherent scattering domain size of the core estimated from PDF is ~45 Å (**Figure 3**). As discussed below, this estimate of domain size may in fact reflect a relatively wide distribution of actual particle sizes.

The effects of heat treatment on the iron core as part of the processing of the commercial sample of native HoSF was also evaluated here. While previous studies have shown that the reactivity of the iron core is not substantially affected by heat treatment (*16*), to our knowledge changes in the atomic arrangement have not been evaluated using advanced structure determination methods. Sample FeFn-3000 was formed from reconstituted APO ferritin with no subsequent heat treatment. The PDF of nanocrystalline core formed in FeFn-3000 is virtually identical to that observed in native HoSF (**Figure 5**). This finding suggests strongly that the short duration of heat treatment and moderate temperatures do not cause a structural transformation from ferrihydrite to a relatively stable phase such as hematite (Fe_2O_3).

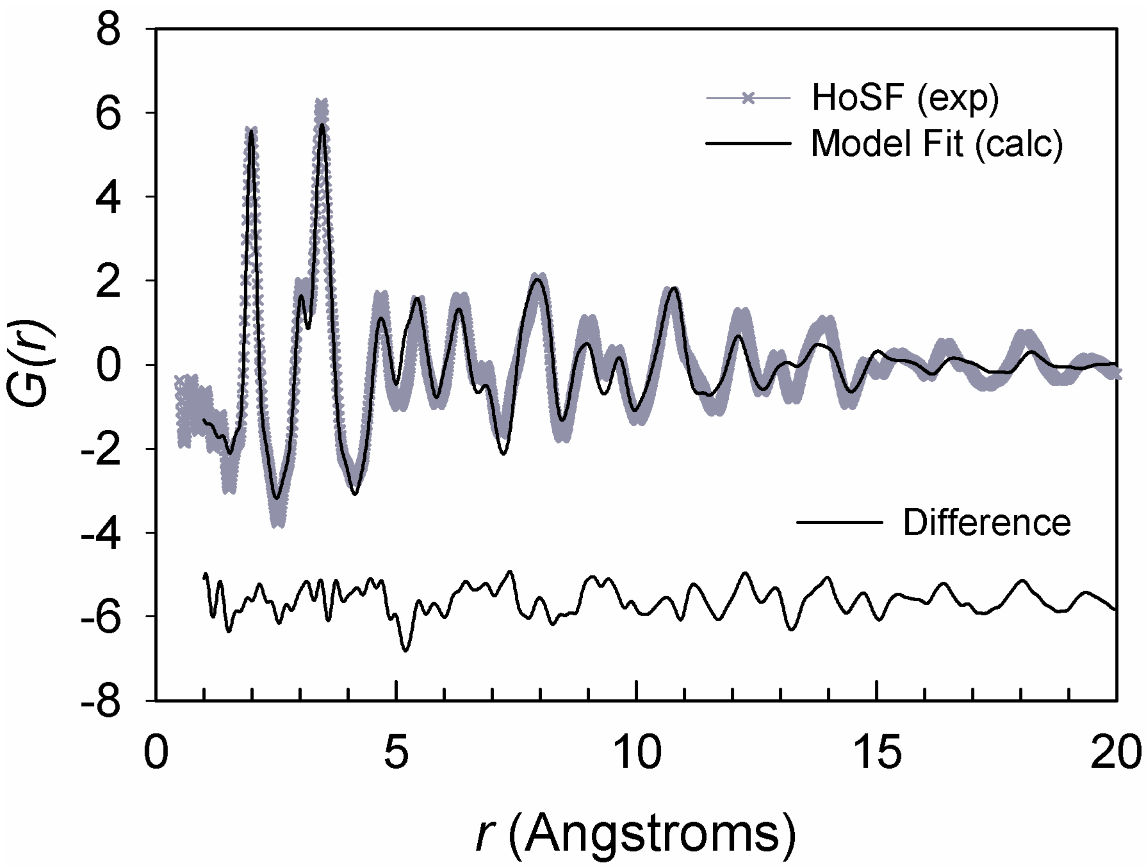

Figure 4. The real-space experimental PDF for the inorganic core in HoSF (grey x). The PDF is calculated from the experimental structure function (SOM Figure 2S) obtained from the scattering data shown in Figure 2. The calculated fit using the structural model for inorganically-derived ferrihydrite is overlain (solid black). The difference between the observed and calculated PDFs is included below. The small feature observed in the difference pattern at ~1.3 Å may be attributable to residual correlations associated with the ferritin shell (e.g., C – C distances).

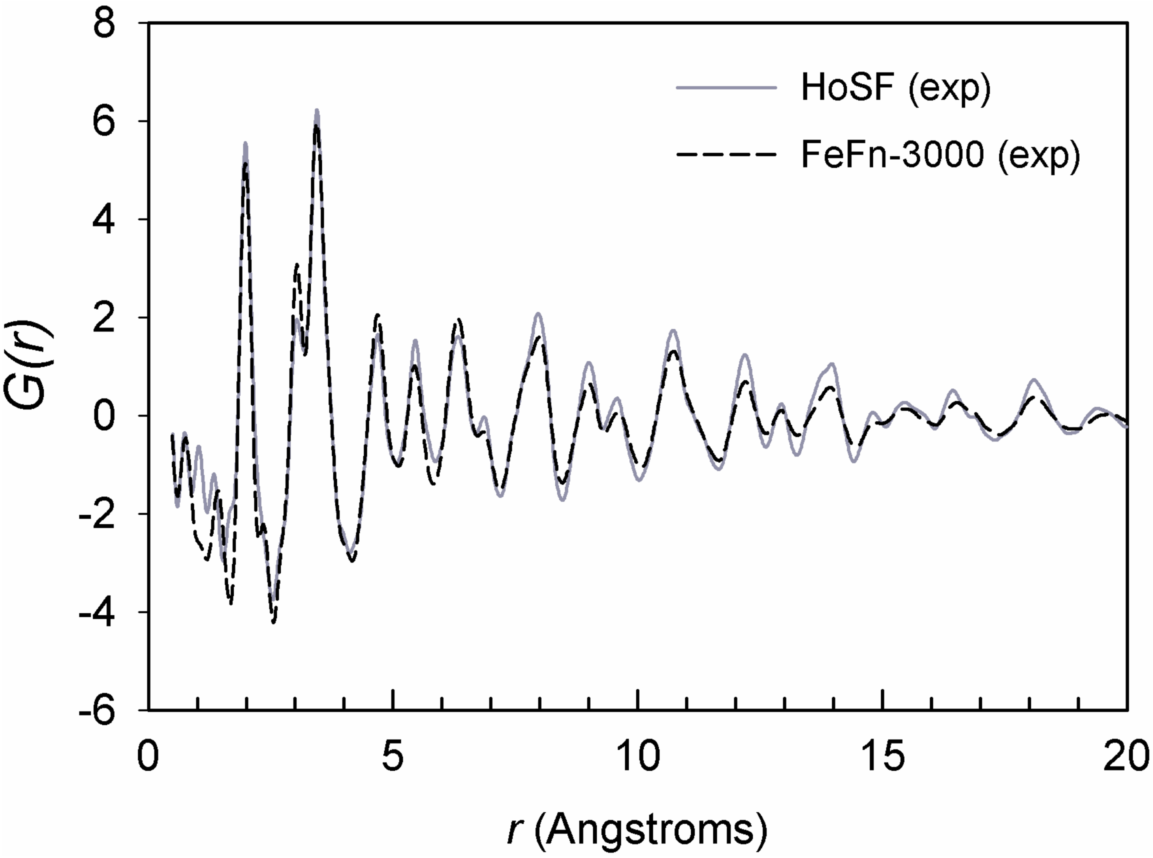

Figure 5. The real-space experimental PDFs for the inorganic cores in FeFn-3000 (solid grey) and in native HoSF (black dashes). The PDFs for these two samples are virtually identical over more than 20 Å. The features at distances shorter than the first coordination shell for iron at ~2 Å are a consequence of the Fourier transformation and not meaningful.

The role of phosphorus in ferritin is only partially understood, although its association with the native ferrihydrite core is reported in varying amounts ranging from ~10-20 : 1 Fe : P (*1*). Phosporus is generally found in relatively low abundance in HoSF and has been suspected as being primarily surface adsorbed (*17*). The PDF presented here does not show any obvious features suggesting the presence of P-O pair correlations, for example if PO_4^{3-} tetrahedra were decorating the hydrated surface a correlation would be expected at ~1.5 Å. Alternatively, it is feasible for P to be incorporated in the crystal structure of ferrihydrite as a substitute for oxygen. The adequate fit of the model suggests that P substitution in the ferrihydrite core does not significantly affect the overall structure; however it is likely beyond the resolution of the technique in low abundance.

Conclusions

Using high-energy total x-ray scattering coupled with PDF analysis, we show that the structure of the iron core found in commercially available native horse-spleen has a structure consistent with single-phase ferrihydrite. This suggests strongly that even the particles in the very early stages of nucleation, perhaps as very small iron clusters, have an atomic arrangement consistent with that of ferrihydrite. The validity of this conjecture will have to be tested in future studies. Further, we show that the heat treatment routinely used in the processing of commercially available samples does not result in a fundamental structural change of the ferrihydrite core. Hence, the mineral assembled within ferritin in living organisms, is within our experimental resolution, the same ubiquitous inorganically-derived nanocrystalline material that controls chemistry in soils and aquatic environments

.

References:

1. A. Lewin, G. R. Moore, N. E. Le Brun, *Dalton Transactions*, 3597 (2005).
2. X. K. Yang, N. D. Chasteen, *Biochemical Journal* **338**, 615 (1999).
3. D. W. Rice, G. C. Ford, J. L. White, J. M. A. Smith, P. M. Harrison, *Advances in Inorganic Biochemistry* **5**, 39 (1983).
4. J. M. Cowley, D. E. Janney, R. C. Gerkin, P. R. Buseck, *Journal of Structural Biology* **131**, 210 (2000).
5. F. M. Michel *et al.*, *Science* **316**, 1726 (2007).
6. B. W. Gabrio, A. Shoden, C. A. Finch, *Journal of Biological Chemistry* **204**, 815 (1953).
7. A. P. Hammersley. (*ESRF Internal Report,* ESRF98HA01T, 1998).
8. A. P. Hammersley, S. O. Svenson, M. Hanfland, D. Hauserman, *High Pressure Research* **14**, 235 (1996).
9. X. Qiu, J. W. Thompson, S. J. L. Billinge, *Journal of Applied Crystallography* **37**, 110 (2004).
10. P. J. Chupas *et al.*, *Journal of Applied Crystallography* **36**, 1342 (2003).
11. F. M. Michel *et al.*, *Chemistry of Materials* **19**, 1489 (Mar, 2007).
12. C. L. Farrow *et al.*, *Journal of Physics: Condensed Matter* **19**, 335219 (2007).
13. B. D. Hall, D. Zanchet, D. Ugarte, *Journal of Applied Crystallography* **33**, 1335 (2000).
14. F. M. Michel *et al.*, *Chemistry of Materials* **17**, 6246 (2005).
15. N. D. Chasteen, P. M. Harrison, *Journal of Structural Biology* **126**, 182 (Jun, 1999).
16. M. L. Bertrand, D. C. Harris, *Experientia* **35**, 300 (1979).
17. J. L. Johnson, M. Cannon, R. K. Watt, R. B. Frankel, G. D. Watt, *Biochemistry* **38**, 6706 (1999).

Crystallographic Information File

```
data_Native_Ferritin

_ccdc_journal_manuscript_code     #######
_publ_requested_journal           Science
_publ_contact_author_name         'F. Marc Michel'
_publ_contact_author_address
;Department of Geosciences
Stony Brook University
255 Earth & Space Sciences Bldg.
Stony Brook, NY 11794-2100
;
_publ_contact_author_email        fmichel@ic.sunysb.edu
_publ_contact_author_phone        631-632-6839
_publ_contact_author_fax          631-632-8240

_audit_creation_method            'Created with Diamond
                                  (www.crystalimpact.com)'
_audit_creation_date              07-07-21
_audit_update_record              07-07-21
_chemical_name_systematic         'Horse-spleen ferritin core'
_chemical_formula_structural      'Fe9.73 O14 (OH)2'
_chemical_formala_sum             'H2 Fe9.73 O16'
_chemical_name_mineral            Ferrihydrite
_chemical_formula_weight          799.237
_chemical_compound_source         Natural

_cell_length_a                    5.9745(6)
_cell_length_b                    5.9745(6)
_cell_length_c                    9.0793(4)
_cell_angle_alpha                 90
_cell_angle_beta                  90
_cell_angle_gamma                 120
_cell_volume                      280.7
_cel_formula_units_z              1

_symmetry_cell_setting            hexagonal
_symmetry_space_group_name_H-M    'P 63 m c'
_symmetry_int_table_number        186
_symmetry_space_group_name_Hall   P_6c_-2c

_diffrn_radiation_probe           x-ray
_diffrn_radiation_type            monochromatic
_diffrn_radiation_wavelength      0.1240(6)
_diffrn_source                    synchrotron
_diffrn_source_type               'APS Beamline XOR 1-ID'

loop_
_symmetry_equiv_pos_site_id
_symmetry_equiv_pos_as_xyz
1 'x, y, z'
2 'x-y, x, 1/2+z'
3 '-y, x-y, z'
4 '-x, -y, 1/2+z'
5 '-x+y, -x, z'
6 'y, -x+y, 1/2+z'
7 '-x+y, y, z'
```

```
8 'x, x-y, z'
9 '-y, -x, z'
10 'y, x, 1/2+z'
11 'x-y, -y, 1/2+z'
12 '-x, -x+y, 1/2+z'

loop_
_atom_type_symbol
_atom_type_oxidation_number
Fe3+ 3
O2-  -2
H1+  1

loop_
_atom_site_label
_atom_site_type_symbol
_atom_site_symmetry_multiplicity
_atom_site_Wyckoff_symbol
_atom_site_fract_x
_atom_site_fract_y
_atom_site_fract_z
_atom_site_occupancy
_atom_site_attached_hydrogens
_atom_site_u_iso_or_equiv
Fe1 Fe3+ 6 c 0.1688(8) 0.8311(2) 0.6305(6) 0.99(3) 0.024(1)
Fe2 Fe3+ 2 b 0.33334 0.66667 0.3245(8) 0.97(6) 0.024(1)
Fe3 Fe3+ 2 b 0.33334 0.66667 0.9505(8) 0.91(1) 0.024(1)
O1 O2- 2 a 0.00000 0.00000 0.0525(4) 1. 0.007(3)
O2 O2- 2 b 0.33334 0.66667 0.7592(8) 1. 0.007(3)
O3 O2- 6 c 0.1612(9) 0.8387(2) 0.2379(4) 1. 0.007(3)
O4 O2- 6 c 0.5393(6) 0.4606(4) 0.9793(1) 1. 0.007(3)

#Position of Elements of H are undetermined
#End of data_Native_Ferritin
```

Chapter 8: Summary and Outlook

Working with the nanosized compounds involved in this dissertation presented a variety of experimental challenges. Difficulties were initially encountered in synthesizing, processing, and handling of samples, particularly in the case of air-sensitive compounds, and also in evaluating the fundamental attributes of interest. These hurdles were overcome by first developing and utilizing straightforward albeit careful laboratory procedures for synthesis, processing, and handling. Subsequently, a combination of laboratory and synchrotron-based techniques provided insight into the fundamental aspects of size, shape, composition, and structure for several important compounds relevant to environmental, industrial, and biological systems.

In terms of procedures for handling nanoparticles, a characteristic observed in these studies was the tendency for nanoparticulate sulfides and oxides to aggregate strongly in solution. Consequently, the common method of drying and washing using membrane filters was not feasible due to rapid clogging of the filter apparatus. Nanoparticles also tend to scavenge artifacts (e.g., NH_4^+ and SO_4^{2-}) left over from the reagent solutions during synthesis due to an enormous amount of reactive surface area. Without removal, such artifacts ultimately precipitate during drying as impurity phases and complicate subsequent analyses. As such, procedures for repeatedly washing these samples prior to drying were developed and all were performed under a controlled atmosphere. Working with air-sensitive nanoparticles of MnS and FeS added additional challenges and necessitated not only the development of specific handling procedures, but also the use of reliable equipment. The anoxic chamber used for synthesizing and processing of these samples was upgraded with gas monitoring, gas delivery, and a catalyst system to ensure an atmosphere devoid of oxygen. The development of additional strategies for transporting these reactive compounds to synchrotron facilities for analysis was also required. These procedures were necessary to ensure sample integrity throughout each experiment. In order to obtain consistent and reliable results in future experiments, these procedures are described in detail in Chapters 3 and 4.

Once the challenges of synthesizing, processing, and handling of nanosized samples were managed, high-energy X-ray total scattering and PDF analysis proved to be a powerful tool for evaluating their atomic arrangements. Although other techniques such as direct imaging and thermal analysis provided complementary information, the most important results in this dissertation relate to the determination of the atomic arrangements of several important compounds. In certain cases, the PDFs for samples were satisfactorily fitted using structure models derived from known bulk counterparts. This was true in the case of FeS where the PDF was fitted using the single-phase structure for well-crystallized mackinawite. This finding resolved a long-standing debate on the structure of this phase and for the first time a complete and quantitative structure model is now available. This model will be an essential component of future studies regarding the association of this phase with impurities through adsorption and co-precipitation, as well as evaluating its transformation to relatively stable phases (e.g., pyrite).

In the case of MnS, a combination of the structures of two metastable polymorphs (γ and β) where required to adequately describe the PDF of the initial nanosized precipitate. This poorly crystalline compound is an important precursor to its relatively stable, well-crystallized polymorphs which have a variety of potential technological applications. While the spatial relationship of the two phases is still uncertain, this finding opens up a new direction for understanding the properties of this compound. Additionally, detailed protocols for synthesizing well-crystallized γ- and α-MnS polymorphs using hydrothermal routes were described.

The most important finding of this dissertation is undoubtedly the development of a new structure model for ferrihydrite. The robustness of this model was not only shown for the inorganically-derived ferrihydrite samples with three distinct particle sizes (Chapters 5 and 6), but was also shown for ferrihydrite formed through biomineralization in the ferritin protein. Furthermore, the establishment of a crystal structure provides additional constraints on composition of this phase which is now understood in ideal form as $Fe_{10}O_{14}(OH_2)$. This study also identified the presence and particle size dependence of surface-adsorbed water using a combination of PDF and TGA. While this model provides a new understanding of the iron and oxygen framework in ferrihydrite, the role of water in the structure is still only partially understood. Future experiments using neutron total scattering and PDF analysis on carefully deuterated synthetic ferrihydrite are necessary in order to complete this model. Additionally, the surfaces of ferrihydrite particles are likely to be substantially different from the interior due to strain and relaxation effects and it is anticipated that simulations based on theoretical modeling will add to the story.

In regards to the biomineralization of ferrihydrite in ferritin, determining the structure of the nanocrystalline iron core (Chapter 7) resolved another long-standing question. By additionally comparing the natural sample to a ferritin sample reconstituted with iron, it was also shown that the routine heat treatment done on commercially-available samples does not result in a structural transformation of the core. This is the first example where the structure of the nanosized core in ferritin with the protein shell intact was evaluated using total scattering and PDF analysis. As these nanosized protein cages are increasingly being used as platforms for the nanoscale engineering of dispersed materials with biocompatible and bioactive properties, this result opens up a number of exciting possibilities in terms of future experiments.

Experiments aimed at evaluating the atomic arrangements of natural samples of ferrihydrite collected from acid mine drainage sites are interesting future possibilities. These samples are inherently more complex due to the conditions of formation and substitution of impurities. It is anticipated that the model presented here for synthetic ferrihydrite will allow the structures of natural samples, typically forming with coherent domain sizes ~1 nm, to be studied quantitatively. This will be an important development for future studies focused on evaluating the association and incorporation of impurities and contaminants. This will ultimately lead to a more comprehensive understanding of this phase and will be essential to evaluating and tracking changes over time.

The utility of high-energy X-ray total scattering and PDF analysis is shown as the best method currently available for evaluating the structures of the nanosized compounds included in this dissertation. While the studies included here were all done under ambient conditions, PDF is versatile in that it can be used for evaluating structural changes in situ and as a function of time, temperature, solution chemistry, relative humidity, etc. The widespread and increasing scientific interest in nanoparticles makes this a promising technique in a stimulating area of research. Technical advances may someday allow full particle simulations which describe the positions of all atoms in a single particle. One promising technique is X-ray photon correlation spectroscopy using the Linac Coherent Light Source (LCLS), a free-electron laser which is in the process of being built at the Stanford Linear Accelerator Center at Stanford University. The LCLS will provide photons of unprecedented brilliance in short pulses and is anticipated to one day allow the evaluation of both structure and dynamics of nanosized materials. Until that time, it is the current state-of-the-art to use periodic models, as shown in this dissertation, to describe the structures of most nanocrystalline and well-crystallized compounds.